

Electrical Engineering

**Biljana Milivojevic**

**Study of Optical Differential Phase Shift Keying  
Transmission Techniques at 40 Gbit/s and  
beyond**

PH.D. Dissertation

Paderborn, April 2005

# DISSERTATION

ON

## **Study of Optical Differential Phase Shift Keying Transmission Techniques at 40 Gbit/s and beyond**

SUBMITTED IN PARTIAL FULFILLMENT OF THE  
REQUIREMENTS FOR THE DEGREE OF  
DOKTOR-INGENIEUR  
IN ELECTRICAL ENGINEERING  
**(Dr.-Ing.)**

TO

DEPARTMENT OF ELECTRICAL ENGINEERING  
UNIVERSITY OF PADERBORN  
WARBURGER STR. 100, 33098 PADERBORN  
GERMANY

BY

**Dipl.-Ing. Biljana Milivojevic**  
from Serbia and Montenegro

Reviewers:

1. Prof. Dr.-Ing. Reinhold Noé
2. Prof. Dr.-Ing. Andreas Thiede

Date of Thesis Submission: April 7, 2005

Date of Defense Examination: June 22, 2005

Paderborn, April 2005  
Diss.



*Dedicated to  
my parents, my husband and my dearest kid Nikola*



# Contents

<b>Contents</b>	<b>V</b>
<b>List of Figures</b>	<b>VIII</b>
<b>List of Tables</b>	<b>XIII</b>
<b>List of Publications</b>	<b>XV</b>
<b>ABSTRACT</b>	<b>XIX</b>
<b>1 Introduction</b>	<b>1</b>
1.1 Background . . . . .	1
1.2 Motivation . . . . .	3
1.2.1 oDPSK and oDQPSK Transmission . . . . .	3
1.2.2 High-Speed Integrated Circuits for xPSK Transmission . . . . .	4
1.3 Organization of Thesis . . . . .	5
<b>2 oDPSK Transmission System</b>	<b>7</b>
2.1 oDPSK signal generation . . . . .	8
2.1.1 Differential Encoding and Decoding . . . . .	8
2.1.2 Optical Phase Modulation . . . . .	11
2.1.3 40 Gbit/s (CS)RZ-DPSK transmitter . . . . .	16
2.1.4 Experimental Results . . . . .	21
2.2 oDPSK signal detection . . . . .	21
2.2.1 Mach-Zehnder Interferometer Modelling . . . . .	22
2.2.2 40 Gbit/s RZ-DPSK receiver . . . . .	23
2.2.3 Measurement results . . . . .	25
2.3 Signed On Line Chromatic Dispersion Detection . . . . .	27
2.3.1 Chromatic Dispersion in Single Mode Fibers . . . . .	27
2.3.2 Measurement Setup for Chromatic Dispersion Detection . . . . .	28
2.3.3 Experimental results . . . . .	29
2.4 Chromatic Dispersion Compensation . . . . .	31
2.4.1 Adaptive Tunable CD Compensation . . . . .	33

2.5	Conclusion	38
<b>3</b>	<b>oDQPSK Transmission System</b>	<b>39</b>
3.1	Introduction to oDQPSK	39
3.2	oDQPSK signal generation	41
3.2.1	DQPSK Precoding	41
3.2.2	Optical Encoder	42
3.2.3	40 Gbaud DQPSK Transmitter	47
3.3	oDQPSK signal detection	48
3.3.1	DQPSK Decoding	48
3.3.2	40 Gbaud DQPSK Receiver	49
3.4	2×40 Gbit/s DQPSK Transmission Experiment	49
3.4.1	Transmission setup	49
3.4.2	Measurement Results and Discussion	50
3.5	RZ-DQPSK Polarization Multiplex Transmission	53
3.5.1	Transmission Setup	53
3.5.2	Transmission Results	55
3.6	Conclusion	58
<b>4</b>	<b>High-Speed Integrated Circuits for oDPSK Transmission</b>	<b>59</b>
4.1	Differential Amplifier for 10 and 40 Gbit/s CS(RZ)-DPSK system	59
4.2	Differential Distributed Amplifier	60
4.2.1	Distributed Amplification	61
4.2.2	Circuit Design	63
4.2.3	Result Discussion	68
4.3	10 Gbit/s CMOS Differential Amplifier	68
4.3.1	Design of Transmission Line Structures	69
4.3.2	Circuit Design	74
4.3.3	Result Discussion	77
4.4	Conclusion	77
<b>5</b>	<b>Result Discussion and Future Scope</b>	<b>79</b>
5.1	DPSK Transmission	79
5.2	DQPSK Transmission	80
5.3	High-Speed Integrated Circuit for oDPSK Transmission	81
5.4	Conclusion	82
<b>A</b>	<b>Definitions</b>	<b>83</b>
A.1	Bit Error Rate	83
A.2	Receiver sensitivity	84
A.3	Optical signal-to-noise ratio	84
<b>B</b>	<b>Theory of the Traveling Wave Amplifier</b>	<b>87</b>

<b>C Extraction of Transmission Line Parameters</b>	<b>93</b>
<b>References</b>	<b>96</b>
<b>Acknowledgements</b>	<b>107</b>



# List of Figures

1.1	Traffic Growth Trends . . . . .	2
2.1	Schematic diagram of a differentially encoded (left) and decoded (right) bit	9
2.2	Proposal for regular differential encoding/decoding scheme with realizable feedback delays . . . . .	9
2.3	Simplified differential encoding/decoding scheme . . . . .	10
2.4	Realized scheme . . . . .	10
2.5	Principle of optical PSK signal modulation a) data signal b) carrier c) PSK signal . . . . .	11
2.6	Lithium Niobate-based Phase Modulator . . . . .	12
2.7	Waveguide based travelling-wave phase modulator using x- or z-cut LiNbO <sub>3</sub> materials . . . . .	13
2.8	X-cut Lithium Niobate-based Mach-Zehnder modulator . . . . .	14
2.9	Three different structures for Mach-Zehnder modulator using x- or z-cut LiNbO <sub>3</sub> . . . . .	15
2.10	Chromatic dispersion tolerance of DPSK using either a Mach-Zehnder modulator or a phase modulator at the data rate of 40 Gbit/s and chromatic dispersion of 0, 34, and 68 ps/nm . . . . .	16
2.11	40 Gbit/s CSRZ-DPSK transmitter . . . . .	17
2.12	Photograph of the data buffer board . . . . .	17
2.13	DPSK Transmitter using the MZMs . . . . .	19
2.14	DPSK signal generation . . . . .	20
2.15	a)Transmission characteristic of MZM b)Optical intensity generated signals	20
2.16	DSPK optical receiver . . . . .	21
2.17	Simplified Interferometer model with delay T and retardation R in the lower branch . . . . .	22
2.18	Block diagram of the lock-in amplifier's scheme . . . . .	25
2.19	Optical spectrum at the constructive port (left) and destructive port(right)	25
2.20	BER vs. power at optical preamplifier input for different CS-RZ DPSK modulation format . . . . .	26
2.21	40 Gbit/s eye diagrams back-to-back for NRZ-DPSK (left) and (CS)RZ-DPSK (right) . . . . .	26

2.22	Total dispersion $D$ and relative contributions of material dispersion $D_m$ and waveguide dispersion $D_w$ for a conventional single mode fiber . . . . .	28
2.23	Experimental 40 Gbit/s CSRZ-DPSK setup for chromatic dispersion detection . . . . .	29
2.24	Chromatic dispersion detection readout vs. actual dispersion. Inset: eye diagram resulting from interferometer output signal difference . . . . .	30
2.25	Standard deviation versus measurement interval, at zero actual dispersion .	30
2.26	CSRZ-DPSK eye diagrams at interferometer outputs (top), and difference signal (bottom) back to back (left) after transmission over the 91km (right) .	31
2.27	Illustration of a uniform grating with constant amplitude of refractive index modulation and grating period . . . . .	32
2.28	Principle of FBG CD compensator with circulator . . . . .	33
2.29	CDC Setup for 40 Gbit/s DPSK transmission . . . . .	34
2.30	Photograph of the TeraXion thermally tunable dispersion compensator . . .	35
2.31	Group delay versus wavelength in tunable CD compensator for dispersion settings . . . . .	35
2.32	OSNR needed for BER = $10^{-9}$ versus compensator CD . . . . .	36
2.33	BER versus OSNR. The OSNR is varied by an attenuator. . . . .	37
2.34	40 Gbit/s eye diagrams back-to-back (top) and after 263 km transmission (bottom), for NRZ-DPSK and CSRZ-DPSK (from left to right) . . . . .	37
3.1	DQPSK Constellations . . . . .	40
3.2	Schematic representation of Optical DQPSK signalling . . . . .	41
3.3	DQPSK signal generation using two Mach-Zehnder modulators . . . . .	43
3.4	DQPSK signal generation using Mach-Zehnder and phase modulator . . . .	43
3.5	Single dual-drive MZM for DQPSK signal generation . . . . .	44
3.6	Procedure to find $\varphi_{i1}$ and $\varphi_{i2}$ for $s_i = r_i e^{j\theta_i}$ . . . . .	46
3.7	DQPSK signal generation using a dual-drive Mach-Zehnder modulator and interferometer . . . . .	46
3.8	$2 \times 40$ Gbit/s DQPSK Transmitter . . . . .	47
3.9	40 Gbaud intensity eye diagrams of NRZ-DQPSK (left) and CS(RZ)DQPSK signals (right) . . . . .	48
3.10	DQPSK Decoder . . . . .	48
3.11	$2 \times 40$ Gbit/s RZ-DQPSK transmission setup . . . . .	50
3.12	Measured BERs vs. optical preamplifier input power for RZ-DPSK, RZ-DQPSK, RZ-ASK . . . . .	51
3.13	$2 \times 40$ Gbit/s RZ-DQPSK I and Q eye diagrams back-to-back (top) and after 263 km of fiber (middle). Bottom diagram is back-to-back with wrong interferometer phase . . . . .	52
3.14	$4 \times 40$ Gbit/s per channel RZ-DQPSK PolDM transmission . . . . .	53
3.15	Electrical interference spectra measured in the 12 GHz photoreceiver after the polarizer . . . . .	55

3.16	Back-to-back receiver sensitivity for both in-phase and quadrature data channels for one polarization. Optical power is given for aggregate 160 Gbit/s signal . . . . .	55
3.17	Back-to-back performance of $4 \times 40$ Gbit/s system . . . . .	56
3.18	Eye diagrams in one polarization, (top) back-to-back in I channel, Q channel and (bottom )after 230 km in I and Q channel . . . . .	56
3.19	Optical spectrum after 229 km of fiber . . . . .	57
3.20	Measured Q factors for I and Q data channels in both polarizations back-to-back for 8 WDM channels, and after transmission over 230 km fiber for the CD-compensated 192.5 THz channel . . . . .	57
4.1	Typical 40 Gbit/s CS(RZ)-DPSK balanced optical front end . . . . .	60
4.2	Simulated DC characteristics of the HEMT fabricated in OMMIC D01PH process . . . . .	61
4.3	Basic configuration of the travelling wave amplifier . . . . .	62
4.4	Typical schematic of the cascode amplifier . . . . .	64
4.5	Schematic of the differential pre-amplifier (left) and simulated magnitude of $S_{21}$ and CMRR (right) . . . . .	64
4.6	Schematic of a traveling wave amplifier using cascode as the main amplifying stage . . . . .	65
4.7	Stability factors $k$ and $\mu$ (left) and output reflection coefficient $S_{22}$ (right) . . . . .	65
4.8	Phases on the gate and drain line . . . . .	66
4.9	Layout details of the cascode cell . . . . .	66
4.10	Optimization of forward transmission as a function of number of stages $N$ (left) and group delay (right) . . . . .	67
4.11	Simulated eye diagram for 50 mV <sub>pp</sub> input voltage . . . . .	67
4.12	Layout of the differential distributed amplifier at 40 Gbit/s . . . . .	67
4.13	Cross-section of the 0.18 $\mu\text{m}$ CMOS process (left) and n-MOS transconductance as a function of the gate-source voltage (right) . . . . .	69
4.14	Geometry of the microstripline in CMOS (left) and its characteristic impedance as function of the conductor width (right) . . . . .	70
4.15	Geometry of coplanar waveguide . . . . .	70
4.16	Characteristic impedance of the coplanar waveguide in function of the ratio $W/(W + 2G)$ (left) and conductor width (right) . . . . .	71
4.17	Measured attenuation for 50 $\Omega$ CPW versus width of signal line . . . . .	71
4.18	SL configuration (left) and characteristic impedance of the SL in function of the conductor width (right) . . . . .	72
4.19	Microphotograph of the fabricated MS, CPW and SL (from left to right) . . . . .	72
4.20	Comparison of measured MS, CPW and SL data for the magnitude $S_{21}$ and $S_{11}$ . . . . .	73
4.21	Comparison of measured, simulated and modelled MS data for the magnitude $S_{21}$ (top-left), phase $S_{21}$ (top-right) and magnitude $S_{11}$ (bottom) . . . . .	73

4.22	Comparison of measured, simulated and modelled CPW data for the magnitude $S_{21}$ (top-left), phase $S_{21}$ (top-right) and magnitude $S_{11}$ (bottom) . . .	74
4.23	Comparison of measured, simulated and modelled SL data for the magnitude $S_{21}$ (top-left), phase $S_{21}$ (top-right) and magnitude $S_{11}$ (bottom) . . . .	74
4.24	Schematic of the differential amplifier using striplines in CMOS . . . . .	75
4.25	Microphotograph of the realized chip . . . . .	75
4.26	Comparison of measured, simulated single phase and simulated differential magnitude of $S_{21}$ . . . . .	76
4.27	Comparison of measured, simulated single phase and simulated differential magnitude of $S_{11}$ . . . . .	76
4.28	Measured eye diagram at 10 Gbit/s for $2^7 - 1$ PRBS input signal . . . . .	77
B.1	Lumped transmission line with shunt loss . . . . .	87
B.2	One section of the drain line . . . . .	89
B.3	One section of the gate line . . . . .	89
B.4	Signal path from the input to the output via the 'k'-th transistor . . . . .	91
C.1	Single transmission line represented by a two-port network and described with distributed transmission line parameters R, L, C and $G \rightarrow 0$ . . . . .	93

# List of Tables

1.1	The frequencies of the optical carriers and the propagation losses in single mode optical fiber in the three most popular optical bands . . . . .	1
1.2	Optical carrier rates . . . . .	2
2.1	Selected long-haul 40 Gb/s DPSK transmission experiments . . . . .	7
2.2	The bit stream to be transmitted and bit stream generated for DPSK transmission . . . . .	8
3.1	Phase states for DQPSK signal . . . . .	40
3.2	Selected DQPSK transmission experiments with higher spectral efficiencies	41
4.1	Distributed circuit parameters for interconnect test structures . . . . .	73



## List of Publications

- (1) B. Milivojevic, A. Fauzi Abas, A. Hidayat, S. Bhandare, D. Sandel, R. Noé, M. Guy, M. Lapointe, “1.6 bit/s/Hz, 160 Gbit/s, 230 km RZ-DQPSK Polarization Multiplex Transmission with Tunable Dispersion Compensation”, *IEEE Photonics Technology Letters*, vol. 17 (2005), 495–497.
- (2) B. Milivojevic, Z. Gu, A. Thiede, “10 Gbit/s Differential Amplifier Demonstrating Striplines in 0.18 $\mu$ m CMOS Technology”, *Proc. European Microwave Week, The European Gallium Arsenide and other Compound Semiconductors Application Symposium*, Paris, France (October 2005), accepted.
- (3) B. Milivojevic, S. Hoffmann, A. Thiede, R. Noé, R. Leblanc, B. Wroblewski, “Distributed Amplifiers for Transmitter and Receiver of a 40 Gbit/s DPSK Optical Transmission System”, *Proc. European Microwave Week, The European Gallium Arsenide and other Compound Semiconductors Application Symposium*, Amsterdam, The Netherlands, (October, 2004), 9–12.
- (4) B. Milivojevic, A. Fauzi Abas, A. Hidayat, S. Bhandare, D. Sandel, R. Noé, M. Guy, M. Lapointe, “160 Gbit/s, 1.6 bit/s/Hz RZ-DQPSK Polarization-Multiplexed Transmission over 230 km Fiber with TDC”, *Proc. European Conference on Optical Communication ECOC*, Stockholm, Sweden, (2004), We1.5.5.
- (5) B. Milivojevic, D. Sandel, S. Bhandare, R. Noé, F. Wüst, “Chromatic Dispersion Detection in a 40 Gbit/s CSRZ-DPSK Transmission”, *Proc. YUINFO*, Kopaonik, Serbia and Montenegro, (2004), CD-58, 91.
- (6) B. Milivojevic, D. Sandel, S. Bhandare, R. Noé, F. Wüst, “40 Gbit/s CSRZ-DPSK Transmission System with Signed Online Chromatic Dispersion Detection”, *IEE Electronics Letters*, vol. 39 (2003), 1455–1456.
- (7) B. Milivojevic, D. Sandel, S. Bhandare, R. Noé, F. Wüst, “Practical 40 Gbit/s CSRZ-DPSK Transmission System with Signed Online Chromatic Dispersion Detection”, *Proc. European Conference on Optical Communication ECOC*, Rimini, Italy, (2003), Tu3.6.4.
- (8) A. Fauzi, B. Milivojevic, A. Hidayat, S. Bhandare, D. Sandel, H. Zhang, R. Noé, “2.38 Tbit/s, 1.49 bit/s/Hz, 40 Gbit/s RZ-DQPSK Polarization Division Multiplex Transmission over 273 km of Fiber”, *Electrical Engineering archive for Electrotechnics*, Springer-Verlag GmbH, (July, 2005), ISSN: 0948-7921, 1432-0487 (Online), DOI: 10.1007/s00202-004-0274-y.
- (9) S. Bhandare, D. Sandel, B. Milivojevic, A. Hidayat, A. Fauzi, H. Zhang, S. K. Ibrahim, F. Wüst, R. Noé, “5.94 Tbit/s (40 $\times$ 2 $\times$ 2 $\times$ 40 Gbit/s) C-Band Transmission over 324 km

using RZ-DQPSK Combined with Polarization Division Multiplex”, 6. *ITG-Fachtagung Photonische Netze*, Leipzig, Germany, (May, 2005), 87–90.

(10) S. Bhandare, D. Sandel, B. Milivojevic, A. Hidayat, A. Fauzi, H. Zhang, S. K. Ibrahim, F. Wüst, and R. Noé, “5.94 Tbit/s, 1.49 bit/s/Hz ( $40 \times 2 \times 2 \times 40$  Gbit/s) RZ-DQPSK Polarization Division Multiplex C-Band Transmission over 324 km”, *IEEE Photonics Technology Letters*, vol. 17 (April, 2005), 914–916.

(11) D. Sandel, S. Bhandare, B. Milivojevic, R. Noé, M. Guy, M. Lapointe, “Automated tunable chromatic dispersion compensation at 40 Gbit/s”, *Proc. 5. ITG-Fachtagung Photonische Netze*, Leipzig, Germany, (May, 2004), 199–201.

(12) S. Bhandare, D. Sandel, B. Milivojevic, A. Fauzi Abas Ismail, A. Hidayat, R. Noé, “ $2 \times 40$  Gbit/s RZ-DQPSK transmission”, *Proc. 5. ITG-Fachtagung Photonische Netze*, Leipzig, Germany, (May, 2004), 195–197

(13) D. Sandel, S. Bhandare, A. Fauzi, B. Milivojevic, R. Noé, M. Guy, and M. Lapointe, “Automatic Tunable Chromatic Dispersion Compensation at 40 Gbit/s in ASK and DPSK NRZ and CSRZ, 263 km Transmission Experiment”, *IEEE Photonics Technology Letters*, vol. 16 (2004), 2568–2569.

(14) S. Bhandare, D. Sandel, A. F. Abas, B. Milivojevic, A. Hidayat, R. Noé, M. Guy, M. Lapointe, “ $2 \times 40$  Gbit/s RZ-DQPSK transmission with tunable chromatic dispersion compensation in a 263 km fiber link”, *IEE Electronics Letters*, vol. 40 (2004), 821–822.

(15) R. Noé, D. Sandel, S. Bhandare, F. Wüst, B. Milivojevic, V. Mirvoda, “Signed on-line chromatic dispersion monitoring by synchronous detection of FM-induced arrival time modulations in the clock recovery PLL”, *Journal of Optical Networking, Optical Society of America*, vol. 3 (2004), 589–600.

(16) A. Fauzi, D. Sandel, A. Hidayat, B. Milivojevic, S. Bhandare, H. Zhang, R. Noé, “2.56 Tbit/s, 1.6 bit/s/Hz, 40 Gbaud RZ-DQPSK polarization division multiplex transmission over 273 km of fiber”, *Proc. OECC/COIN2004*, Yokohama, Japan, (2004), PD1-4.

(17) S. Bhandare, D. Sandel, A. Fauzi, B. Milivojevic, R. Noé, M. Guy, M. Lapointe, “Fully automatic, tunable chromatic dispersion compensation at 40 Gbit/s in ASK and DPSK, NRZ and CSRZ, 263 km transmission experiments”, *Proc. OECC/COIN2004*, Yokohama, Japan, (2004), 15C1-4.

(18) D. Sandel, S. Bhandare, A. Fauzi, F. Wüst, B. Milivojevic, A. Hidayat, R. Noé, M. Guy, M. Lapointe, “ $2 \times 40$  Gbit/s RZ-DQPSK transmission over 263 km of fiber with tunable

chromatic dispersion compensator”, *Proc. OECC/COIN2004*, Yokohama, Japan, (2004), 16C2-3.

(19) S. Bhandare, A. Hidayat, D. Sandel, A. F. Abas, H. Zhang, B. Milivojevic, R. Noé, M. Guy, M. Lapointe, “Adaptive 700...1350 ps/nm Chromatic Dispersion Compensation in 1.6 Tbit/s (40×40 Gbit/s) DPSK and ASK Transmission Experiments over 44...81 km of SSMF”, 6. *ITG-Fachtagung Photonische Netze*, Leipzig, Germany, (May, 2005), 91–94.



## ABSTRACT

The return-to-zero Differential Phase Shift Keying (RZ-DPSK) transmission format has attracted the interest of transmission experimentalist as an enabler for 40 Gbit/s systems because it provides 3 dB more system margin. Combined with Return-to-Zero (RZ) coding, it is also more resilient to non-linear distortions imposed by the transmission fiber. Here, a 40 Gbit/s Carrier-Suppressed RZ-DPSK transmission system with receiver sensitivity of  $-33.5$  dBm is presented. Various new features such as demodulation of RZ-DPSK signals using a delay interferometer having delay of 4 symbol durations and lock-in stabilization of the delay interferometer phase are demonstrated. It is particularly shown that a signed online chromatic dispersion measurement scheme which synchronously detects arrival time variations in the clock recovery phase locked loop also works for this type of modulation formats.

Further more, the residual chromatic dispersion of a various fiber link lengths up to 263 km length is automatically compensated for NRZ-DPSK and CSRZ-DPSK modulation formats at 40 Gbit/s, using synchronous arrival time detection scheme and a fiber Bragg grating-based thermally tunable dispersion compensator in the range of  $-300$  to  $-700$  ps/nm. The total measured penalty of transmission and CD compensation is  $-1.2$  dB ...  $+1.2$  dB, for various link lengths and compensator CDs.

A simple alternative to double the existing transmission capacity without optical bandwidth increase is to use Differential Quadrature Phase Shift Keying (DQPSK). Combined with RZ coding its robustness against cross-phase modulation is also large because the intensity is not modulated by the data. In this work,  $2 \times 40$  Gbit/s (40 Gbaud) RZ-DQPSK transmission over 263 km of fiber with manually thermally tunable chromatic dispersion compensator with a back-to-back Q factor  $> 20$  dB (extrapolated BER  $< 10^{-23}$ ) is reported. The receiver sensitivity is  $-27.5$  dBm. Even after transmission the Q factor is 17.5 dB.

DQPSK and polarization division multiplex (PoIDM) transmission each double fiber capacity by their increased spectral efficiency. Both techniques have been combined to transmit  $4 \times 40$  Gbit/s per WDM channel. The fiber capacity is 1.6 bit/s/Hz, the value which has been previously reported or surpassed only at 10 Gbaud. A 1.6 bit/s/Hz transmission over 230 km of fiber is demonstrated with  $Q > 15.6$  dB for one of the 8 WDM channels for which the thermally tunable dispersion compensator was operational.

A differential amplifier combined with travelling wave amplifier at 40 Gbit/s is designed and simulated in a pseudomorphic AlGaAs/InGaAs HEMT technology. The gain and 3 dB bandwidth are 17 dB and 46 GHz, respectively.

A version of the amplifier that will work at 10 Gbit/s is simulated, designed, and fabricated in low-cost  $0.18\mu\text{m}$  CMOS technology. Amplifier makes use of striplines. The experiment demonstrates the 10 Gbit/s signal propagation over narrow CMOS striplines. For a single phase input, amplifier has a gain of 6 dB at 10 Gbit/s. The measured bandwidth is 6.2 GHz and common mode rejection ratio (CMRR) is 8 dB. This CMOS circuit using striplines exhibits a performance comparable performances with that of the state-of-the-art amplifiers designed in conventional technologies. This opens the possibility for using

striplines with its over all good shielding in complex analog systems. Such differential in differential out amplifiers can be used in balanced optical front ends to achieve the record sensitivity values.

# Chapter 1

## Introduction

### 1.1 Background

Concept of optical fiber communication was introduced 20 years ago, when it became possible to reduce the attenuation in glass fibers to a few dB per kilometer. At that time, most fiber optic communication system were using multimode graded-index fibers and laser source radiated around 850 nm. These systems were mainly dispersion limited. Today's optical transmission systems are using the single mode optical fibers. They are operating in the transmission window where the material dispersion (1310 nm) or the attenuation (1550 nm) is minimum in single mode optical fibers. In single mode optical fiber, the light is confined to an area of high refractive index, which acts as *core*, with respect to its surroundings, called as *clad*. The Table 1.1 lists the frequencies of optical carriers and the propagation losses of the single mode optical fibers in the three most popularly used optical transmission windows.

**Table 1.1:** The frequencies of the optical carriers and the propagation losses in single mode optical fiber in the three most popular optical bands

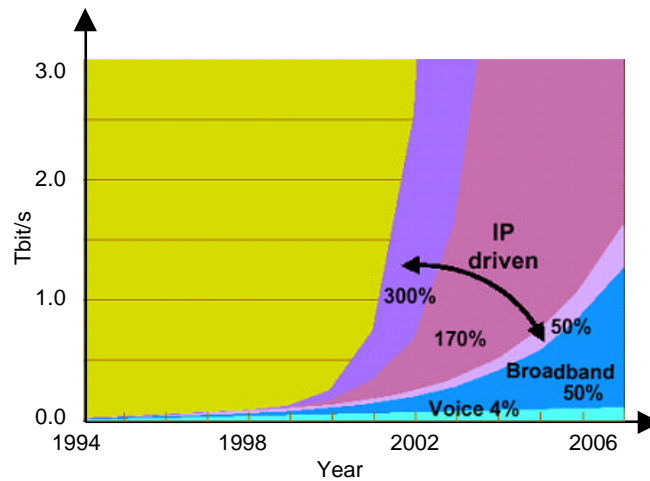
Wavelength ( $\mu\text{m}$ )	Frequency (THz)	Loss (dB/km)
0.85	353	2.0
1.31	229	0.5
1.55	194	0.2

The optical fiber communication industry also experienced the several generations like the integrated circuit technology. The digital optical transmission systems characterized by the available data rates rapidly took over the analog communication systems. The data rate levels commonly used in the digital fiber optical networks are given in Table 1.2. SONET refers to Synchronous Optical Networks, a North American standard while SDH refers to Synchronous Digital Hierarchy, a EU standard. The first generation systems were specified as OC-1 having the basic data of 51.84 Mb/s. OC stands for the optical carrier and each succeeding generation has a data rate which is integer multiple of OC-1.

**Table 1.2:** Optical carrier rates

SONET	SDH	Data Rate (MB/s)
OC-1	STM-0	51.84
OC-3	STM-1	155.52
OC-12	STM-4	622.08
OC-48	STM-16	2488.32
OC-192	STM-64	9953.28
OC-768	STM-256	39813.12
OC-13072	STM-1024	159252.48

The main driving force behind the development of high bit rate transmission systems and the future capacity upgrades are expected due to the exponential growth of the internet traffic. According to the prediction of [1], the expected capacity increase caused by voice based services is almost negligible (4%) compared to other possible broadband services (Figure 1.1). A doubling in internet traffic each year appears a more likely outcome, according to the Moore's law. Transmission systems using high spectral efficiencies are, therefore needed to accommodate the expected capacities in a bandwidth limited case.

**Figure 1.1:** Traffic Growth Trends

However, due to the global economic slow down the predictions from early 90s are no more valid. Recent analysis of US market [2] predict the annual grow of 10.3% for the fiber-optic related products and subsystems through out the year 2006.

Commercially available digital optical transmission systems which are fully operational today mainly suffer from the smaller spectral efficiencies (typically  $< 0.4$  bit/s/Hz) as they use the so called *Intensity Modulation with Direct Detection* (IM/DD) technique. Spectral efficiency is specified in terms of the specified data rate in Gb/s in 100 GHz band limitation.

Intensity modulated systems at higher data rates are also mainly limited by the so called polarization mode dispersion (PMD) [3] once the linear fiber dispersion (chromatic dispersion) is compensated. Therefore, the researchers are looking for the alternative modulation formats that could be implemented in the future generations of the digital optical transmission systems. The newer alternative modulation formats should directly influence the spectral efficiencies and increase the fiber capacity thereby satisfying the growing data traffic demands.

## 1.2 Motivation

The motivation behind this work is to explore the area of modulation formats which are primarily based on phase shift keying (PSK), as an alternative to the conventional intensity modulated formats such as nonreturn-to-zero (NRZ), return-to-zero (RZ) or carrier suppressed return-to-zero (CSRZ). Multi-level PSK-based modulation format offers the possibility to transmit more than one bit of information for the per transmitted optical symbol. This directly increases the spectral efficiency without the optical bandwidth increase. During this work, the digital optical transmission system at 40 Gbit/s is developed based on differential phase shift keying (DPSK) and this concept is later extended to differential quadrature phase shift keying (DQPSK) modulation format which provides 2:1 multiplexing and 1:2 demultiplexing at the optical level (1.2.1). Such systems indeed need the high-speed differential amplifiers for balanced detection (1.2.2).

### 1.2.1 oDPSK and oDQPSK Transmission

Even though PSK sensitivity performance is better than DPSK [4], DPSK is more preferred because demodulation of PSK requires coherent detection where the synchronous optical carrier is regenerated in the receiver so that the phase information can be correctly extracted at the receiver side without any ambiguity. This puts the stringent requirements on the laser linewidths of the transmitter laser and also on the local oscillator laser. These phase fluctuation can also be mitigated, for example, by using a variant of PSK with differential encoding at the transmitter side and a differential decoding at the receiver side. Generally, RZ or CSRZ-DPSK is used instead of NRZ-DPSK. In RZ- or CSRZ-DPSK, the intensity is not modulated by the data but is rather modulated by pulse carving. Thus, the information is carried by the optical phase itself. That's the reason why this modulation format is particularly more robust to cross phase modulation [5–7] and to PMD. A detailed review of such systems using DPSK as an alternative modulation format is given in [8]. The very first optical systems based on PSK were extensively studied with respect to coherent detection [9, 10]. However DPSK is generally demodulated using incoherent detection, for example, by a delay line demodulator followed by balanced detection and therefore, yields 3 dB more system margin as compared to conventional NRZ [11, 12]. Recently, number of experiments are reported using DPSK as an alternative and promising modulation format for long-haul and ultra long-haul optical transmission systems [13–20].

A practical 40 Gb/s CSRZ-DPSK system with signed online chromatic dispersion detection is developed as a part of this work at the University of Paderborn, and is reported in [21, 22]. Adaptive chromatic dispersion compensation is demonstrated in 263 km transmission experiments, for the first time, for NRZ- and CSRZ-DPSK modulation formats, using a thermally tunable dispersion compensator based on fiber Bragg grating technology [23].

A simple alternative to increase the fiber capacity is to use Differential Quadrature Phase Shift Keying (DQPSK) [24–28], which doubles the existing transmission capacity by carrying the two-bits of information for the each transmitted optical symbol [25] without optical bandwidth increase. Combined with RZ coding its robustness against cross phase modulation (XPM) is also large because the intensity is not modulated by the data. DQPSK signal also tolerates strong optical filtering [29]. The theoretically possible receiver sensitivity of DQPSK receiver is better than for intensity modulation.  $2 \times 40$  Gbit/s (40 Gbaud) RZ-DQPSK transmission over 263 km fiber is reported in [30]. This work has demonstrated the sufficient resilience against non-linear phase noise and a band limitation in a 40 Gbit/s WDM DEMUX with  $Q$  factors  $> 17.5$  dB.

The highly spectrally efficient transmission is the key to cost-effective capacity expansion in optical communication systems with a finite limited bandwidth. DQPSK [31, 32] and polarization division multiplex (PoDM) [33], transmission each double fiber capacity by their increased spectral efficiency [6, 27, 33]. 160 Gbit/s ( $4 \times 40$  Gbit/s) Polarization Division Multiplex RZ-DQPSK transmission over 230 km of fiber with  $Q > 15.6$  dB is demonstrated in one of 8 100 GHz-spaced WDM channels for which a thermally tunable dispersion compensator was operational [34].

## 1.2.2 High-Speed Integrated Circuits for xPSK Transmission

The future digital optical transmission systems will either use DPSK or DQPSK modulation formats, as has been mentioned in section 1.2.1. D(Q)PSK receivers are generally based on balanced detection technique and hence need the balanced optical front ends together with differential amplifiers. A differential amplifier concept using pseudomorphic AlGaAs/InGaAs HEMT technology is presented in [35]. The circuit basically consists of a differential preamplifier followed by Travelling Wave Amplifier's (TWA's) as the main amplifying stages. Traditionally, high-speed circuits were realized either in GaAs [36–39], InP [40–42] or in SiGe technology. However, all the above mentioned technologies have relatively high cost of integration. Another alternative is to use the standard CMOS technology to drastically reduce the cost, especially when the 40 Gbit/s circuits are scaled down to 10 Gbit/s. In this work, a single-stage differential pre-amplifier followed by three pairs of common source stages using striplines is implemented in standard  $0.18 \mu\text{m}$  CMOS technology. Simulated and measured results are summarized in [43]. CMOS differential amplifier presented in this work exhibits a performance which is comparable to the state-of-the-art amplifiers designed in other conventional technologies [44–46].

## 1.3 Organization of Thesis

The thesis is mainly organized into five chapters. First chapter is nothing more than a brief introduction to the thesis.

Second chapter deals with the development of a 40 Gbit/s CSRZ-DPSK transmission system with signed online chromatic dispersion detection. Fully automatic tunable chromatic dispersion compensation is demonstrated using signed online chromatic dispersion detection for DPSK signals. Third chapter describes the generation and transmission of  $2 \times 40$  Gbit/s CSRZ-DQPSK signals with and without polarization multiplexing with the thermally tunable manual chromatic dispersion compensation.

Fourth chapter is devoted to design and simulation of high-speed integrated circuits in GaAs and CMOS technologies. Measurement results on the differential amplifier fabricated in  $0.18 \mu\text{m}$  CMOS technology are also summarized in this chapter. Fifth chapter presents summary of all successfully conducted transmission experiments along with the future scope of this work.



# Chapter 2

## oDPSK Transmission System

Return-to-zero differential phase shift keying (RZ-DPSK) has received considerable attention over the last few years as it provides 3 dB improvement in receiver sensitivity using the balanced detection technique compared to standard NRZ modulation format [11]. This improvement directly translates into a reduced optical signal-to-noise ratio (OSNR) requirement to achieve a given bit-error-rate (BER), thereby increasing the system margin. This additional margin can be used to extend the transmission distance, reduce optical power requirement, or relax component specification. RZ-DPSK is also more robust to penalties caused by cross-phase modulation (XPM) in multichannel optical transmission systems [18, 47]. A number of 10 Gb/s transmission experiments using RZ-DPSK are reported in [8, 17, 18, 47, 48]. Table 2.1 summarizes a few selected 40 Gb/s long-haul transmission experiments recently carried out using DPSK as modulation format. During this work, a practical carrier-suppressed RZ-DPSK transmission is demonstrated with signed online chromatic dispersion detection and compensation.

**Table 2.1:** Selected long-haul 40 Gb/s DPSK transmission experiments

Number of Channels	Channels Data Rate (Gb/s)	Distance (km)	Fiber Type (km)	Efficiency (b/s/Hz)	Reference no.
64	42.7	4.000	NZDSF	0.4	[14]
40	42.7	10.000	DM	0.4	[15]
40	42.7	8.740	DM	0.57	[19]
100	43	6.240	DM	0.4, 0.64	[20]
64	42.7	8.200	DM	0.8	[7]
149	42.7	6.120	DM	0.8	[49]
160	42.7	3.200	DM	0.8	[16]

NZDSF: Nonzero dispersion shifted fiber

DM: Dispersion managed fibers

## 2.1 oDPSK signal generation

Phase shift keying formats carry the information in the optical phase itself. Due to the lack of absolute phase reference in direct-detection receivers, the phase of the preceding bit is used as a relative phase reference for demodulation. This results in differential phase shift keying modulation formats which carry the information in optical phase changes between bits. The next subsection illustrates how to generate differentially encoded sequence in the lab environment.

### 2.1.1 Differential Encoding and Decoding

Generally, differentially encoded bit sequence is obtained from the input binary message sequence by using

$$g_i = g_{i-1} \oplus d_i, \quad (2.1)$$

where the index  $i$  identifies the consecutive bits at 40 Gbit/s,  $d_i$  is the binary input information bit sequence to the encoder,  $g_i$  is the output bit sequence of the encoder and  $g_{i-1}$  is the 1-bit delayed version of the  $g_i$ . This symbol  $\oplus$  denotes modulo-2 addition. The encoded symbol  $g$  is transmitted in a bipolar fashion as the optical field polarity as shown in Table 2.2. The differential encoding requires the use of a reference bit before initiating the encoding process. This reference bit could be either arbitrarily set to logic “1” or to logic “0”.

**Table 2.2:** The bit stream to be transmitted and bit stream generated for DPSK transmission

$d_i$		0	1	1	1	0	0	1	1	0
$g_i$	1	0	0	0	0	1	0	0	0	1
phase	0	$\pi$	$\pi$	$\pi$	$\pi$	0	$\pi$	$\pi$	$\pi$	0

Thus, differentially encoding is schematically represented by a two-input XOR gate whose one of the two inputs is driven by the encoding bit sequence, while the other input is driven by its 1-bit delayed version of the encoded bit sequence. Since 40 Gbit/s bit rate corresponds to 25 ps bit duration, the differential encoding at 40 Gbit/s can be implemented as in Figure 2.1 (left). The received symbol is differentially decoded in an interferometer having a 1-bit delay. When written with binary variables the result is

$$d_i = g_{i-1} \oplus g_i, \quad (2.2)$$

just as desired. Schematically differential decoding is represented as shown in Figure 2.1 (right).

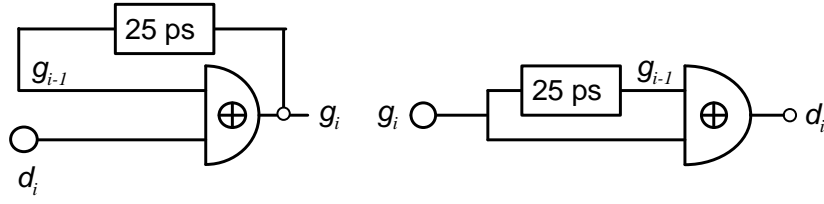


Figure 2.1: Schematic diagram of a differentially encoded (left) and decoded (right) bit

**New Proposal: Regular Differential Encoding/Decoding Scheme**

A practical problem that occurs in DPSK signal generation at 40 Gbit/s is the necessity of recursive differential encoding at 40 Gbit/s, since physically realizable feedback delays exceed 25 ps. Here, this problem is taken into consideration and a new, fully regular encoding scheme (Figure 2.2) is presented. Differential encoding,

$$e_i = e_{i-4} \oplus d_i \tag{2.3}$$

takes place only at 10 Gbit/s in 4 separate, parallel circuits. Then, the signals are then 4:2 multiplexed to 20 Gbit/s and modulo-2-added in 2 parallel circuits according to

$$f_i = e_i \oplus e_{i-2}. \tag{2.4}$$

After the additional 2:1 multiplexing to 40 Gbit/s, a very similar, serial non-recursive operation occurs

$$g_i = f_i \oplus f_{i-1}. \tag{2.5}$$

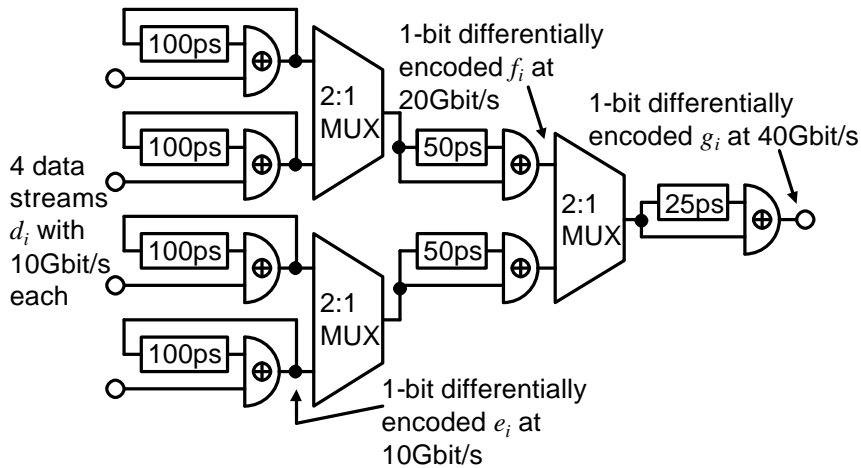
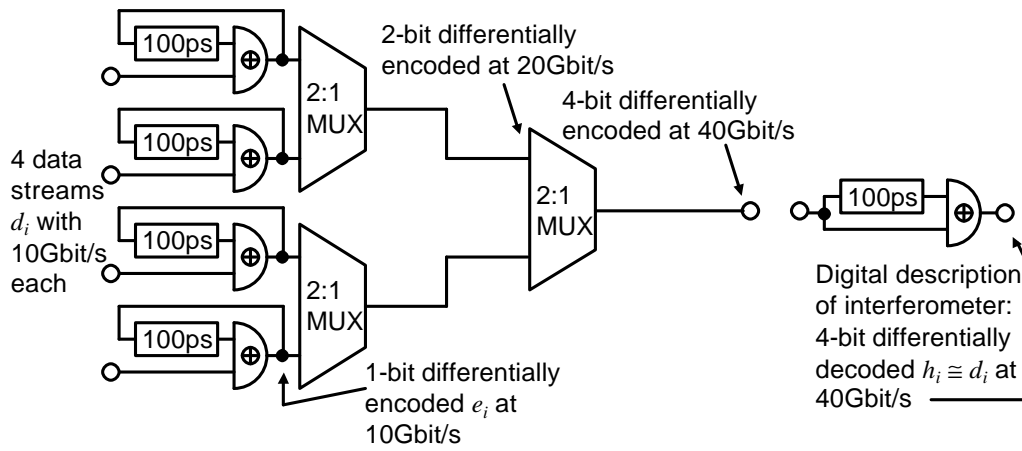
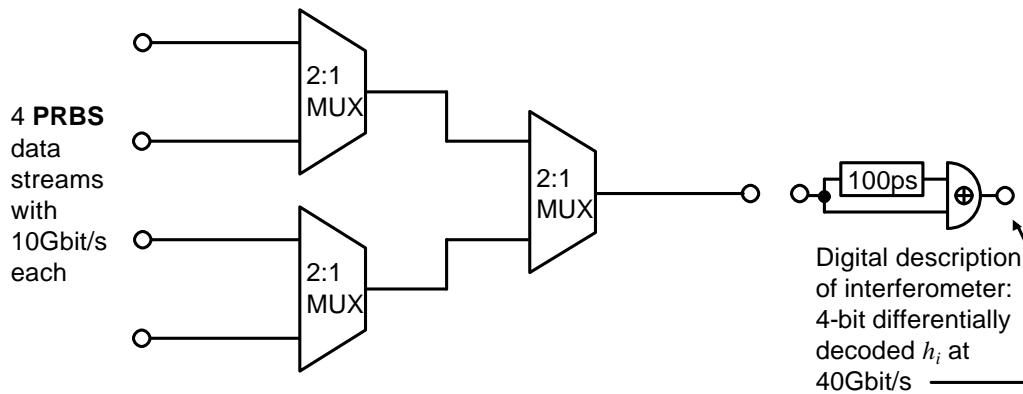


Figure 2.2: Proposal for regular differential encoding/decoding scheme with realizable feedback delays



**Figure 2.3:** Simplified differential encoding/decoding scheme



**Figure 2.4:** Realized scheme

It can be shown that the 1-bit differential decoding

$$h_i = g_{i-1} \oplus g_i, \quad (2.6)$$

results again in

$$h_i = d_i. \quad (2.7)$$

Simplifications are once again possible if recursive differential encoding is possible at 20 Gbit/s.

Even at 10 Gbit/s, DPSK laser linewidth requirements are easily fulfilled, which allows to simplify the matter further. If the interferometer delay is chosen equal to 4-bit durations a more simplified scheme is possible as shown in Figure 2.3. Thus, the 4-bit differential decoding results in

$$h_i = e_i \oplus e_{i-4} = d_i. \quad (2.8)$$

In hereafter presented 40 Gb/s DPSK transmission experiments, differential encoding was neither implemented nor needed because a  $2^7 - 1$  pseudo random binary sequence (PRBS) was transmitted. Therefore, the simplified scheme as shown in Figure 2.4 is realized in the our laboratory.

### 2.1.2 Optical Phase Modulation

The complex electric field of a typical laser source used in the optical communication is represented by:

$$\vec{E} = A(t) \vec{e}(t) \cos \{ \omega t + \varphi(t) \} \quad (2.9)$$

where  $A(t)$  is the amplitude of the optical field,  $\omega$  is the optical angular frequency,  $\varphi$  is the optical phase and  $\vec{e}$  represents the polarization vector of the laser source, also known as Jones-vector. These four parameter represent the four degrees of freedom that can be exploited in the generation of modulated optical signals. Each of these parameters can be modulated by an electrical binary baseband signal  $q(t)$ :

$$q(t) = \sum_{i=-\infty}^{\infty} I_i \cdot q(t - iT_b) \quad (2.10)$$

with the  $i$ -th information coefficient  $I \in [0, 1]$  and the baseband pulse shape  $q(t)$  delayed by multiples of the bit period  $T_b$ .

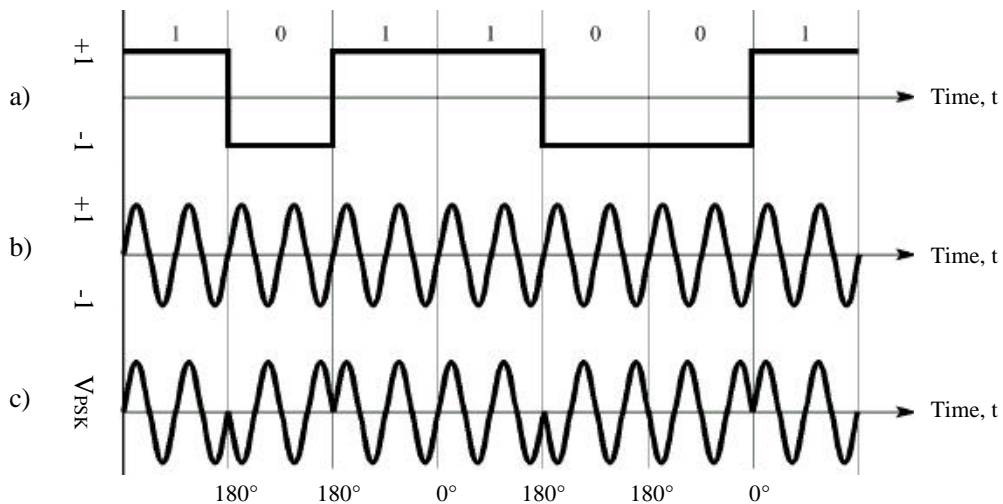


**Figure 2.5:** Principle of optical PSK signal modulation a) data signal b) carrier c) PSK signal

Depending on which parameter of the laser source is modulated, the modulation is mainly differentiated as: amplitude shift keying (ASK), frequency shift keying (FSK), phase shift keying (PSK) or polarization shift keying (PolSK).

Phase modulation is a form of data modulation scheme, where phase of the transmitted signal is varied to convey information (Figure 2.5) but the frequency of the carrier remains constant. The simple method, binary (D)PSK, uses only two signal phases: 0 and  $\pi$  rad. The digital signal is broken up time wise into individual bits (binary digits). The state of each bit is determined according to the state of the preceding bit. It encodes 0 phase shift for a logic input and a  $\pi$  phase shift for a logic 0 input. Thus, signal in D(PSK) representation is given by

$$\varphi_{signal}(iT_b) - \varphi_{signal}[(i-1)T_b] = \begin{cases} 0, & \text{if } q(t - iT_b) = 0 \\ \pi, & \text{if } q(t - iT_b) = 1 \end{cases} \quad (2.11)$$

The phase modulated optical signal could either be generated using commercially available external Lithium Niobate-based phase modulator or by a Mach-Zehnder modulator.

### Simple Phase Modulator

A phase modulator is the simplest waveguide electrooptic device where electro-optically induced refractive index change causes a phase shift of the guided light. Figure 2.6 illustrates the LiNbO<sub>3</sub>-based waveguide electrooptic phase modulator.

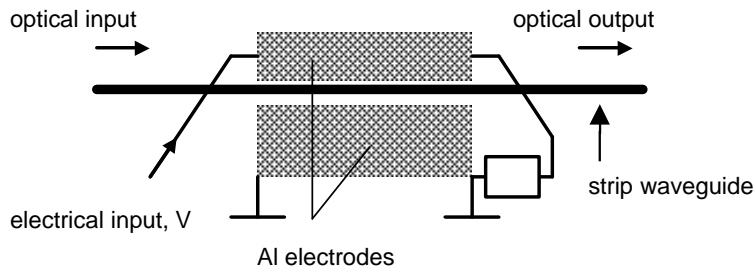


**Figure 2.6:** Lithium Niobate-based Phase Modulator

Basically, phase modulator simply consist of a Ti in-diffused optical channel waveguide placed in between the set of uniform electrodes of length,  $L$ , separated by a gap,  $G$ . The modulating voltage waveform  $V$ , applied to the both electrodes causes electro-optically induced refractive index change and hence the phase length variation of the channel. Actually, the refractive index of the material causes light to travel at a speed inversely proportional to the refractive index of the material. Thus, if the refractive index of a material suddenly increase, the light beam slows down and vice versa. The effective electrooptically induced refractive index change is given by

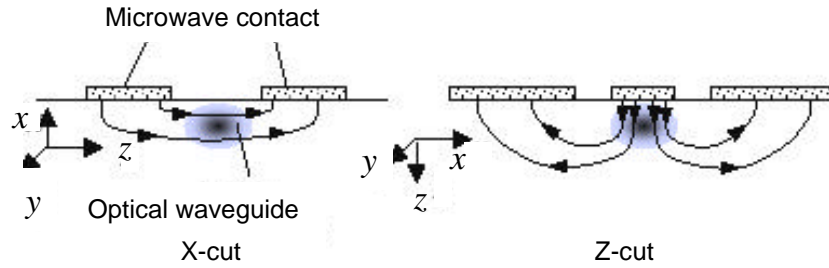
$$\Delta n(V) = -\frac{n_o^3 r_{ij}}{2} \frac{V}{G} \Gamma, \quad (2.12)$$

where  $n_o$  is the ordinary refractive index of  $\text{LiNbO}_3$ ,  $r_{ij}$  is the relevant electrooptic coefficient, an inter electrode gap  $G$ , and  $\Gamma$  is the overlap integral between the applied electrostatic field and the optical mode [50].

Phase modulators are generally characterized by the voltage  $V_\pi$  which is defined as the voltage required to obtain a phase shift of  $\pi$  rad. However, voltage-length product is more useful to compare the performance of different phase modulators and is defined as

$$V_\pi L = \frac{\lambda G}{n_o^3 r_{ij} \Gamma}. \quad (2.13)$$

The output electrical field of the phase modulator is proportional to  $\exp(j\pi V/V_\pi)$ .



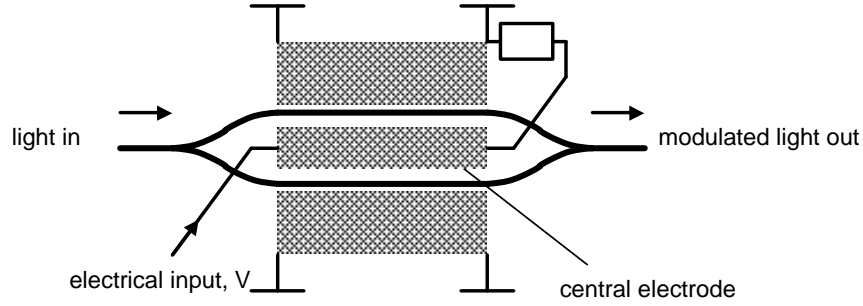
**Figure 2.7:** Waveguide based travelling-wave phase modulator using x- or z-cut  $\text{LiNbO}_3$  materials

Figure 2.7 shows two waveguide based travelling-wave phase modulator structures using x-cut and z-cut  $\text{LiNbO}_3$  crystal, respectively. The electric field lines are along the z-axis in both cases. In x-cut crystal, the electrodes for the radio frequency (RF) transmission line are located on either side of the optical waveguide where as in z-cut crystal, the electrode for the RF transmission line are located directly on the top of the optical waveguide.

### Mach-Zehnder Modulator

The operational principle of MZM are also based on the electro-optic effect. The Mach-Zehnder waveguide structure is typically realized in  $\text{LiNbO}_3$  using titanium-diffused technology. Figure 2.8 is a schematic drawing of such a modulator. At its optical input port, there is an optical power splitter that divides the input optical power into two equal portions. The divided power propagates in two separate waveguides that are often called “two arms”.

In a MZM, at least one of the these two arms is designed as an EO waveguide, along which the optical phase can be modulated by an applied voltage. If the optical waves are in phase after propagating through two arms, they combine as a single mode in the output optical combiner at the output; whereas if the optical waves are out of phase after propagating both arms, they combine as a higher order spatial mode near the optical combiner, therefore, most of the optical power is radiated into the substrate and the output intensity is at its minimum.



**Figure 2.8:** X-cut Lithium Niobate-based Mach-Zehnder modulator

The optical field amplitudes at the output port of the MZM can be generally represented by

$$\vec{E}_{out} = \frac{1}{\sqrt{2}}(\vec{E}_1 e^{j\Phi_1} + \vec{E}_2 e^{j\Phi_2}), \quad (2.14)$$

where  $\vec{E}_1$  and  $\vec{E}_2$  represent the optical field amplitudes in the both arms and  $\Phi_1$  and  $\Phi_2$  represent the optical phase delays. The output optical power is

$$P_{OUT} = |E_{out}|^2 = \frac{1}{2}[|E_1|^2 + |E_2|^2 + 2|E_1||E_2| \cos(\Phi_1 - \Phi_2)]. \quad (2.15)$$

Dividing the  $P_{OUT}$  by the input optical power  $P_{IN} = (|E_1|^2 + |E_2|^2)$  of the MZM and after some parameter transformations, the optical intensity transfer function for the MZM can be written in the form of

$$T_{MZM} = \frac{1}{2}[1 + b \cos(\Phi_1 - \Phi_2)], \quad (2.16)$$

where  $b = 2|E_1||E_2|/(|E_1|^2 + |E_2|^2)$  is an optical imbalance factor between the two arms.  $b = 1$  for ideally balanced design. The phase difference  $(\Phi_1 - \Phi_2)$  consist of two parts; one is the path difference  $\Phi_0$  at zero applied voltage and the other is the phase difference  $\Delta\Phi$  due to applied voltage.

When only one arm is modulated the phase difference becomes

$$\Delta\Phi = \frac{2\pi}{\lambda} \Delta n L \Gamma, \quad (2.17)$$

where  $\Delta n$  is the electrooptically induced index change,  $\Gamma$  is the overlap integral factor,  $\lambda$  is the wavelength,  $L$  is length of the modulator electrode. If both arms are modulated in push-pull mode, which means that the phase changes in the two arms are opposite, the overall phase change  $\Delta\Phi$  is simply doubled.

If the modulation is based on the electrooptic effect, then

$$\Delta n = \frac{1}{2} n_o^3 r_{ij} \frac{V}{G}, \quad (2.18)$$

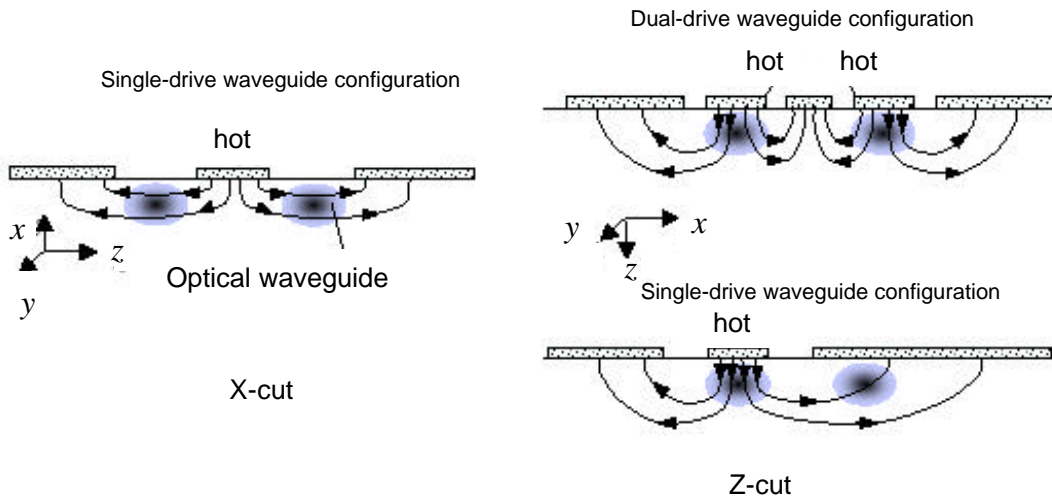
where  $n_o$  is the optical index at the zero applied voltage,  $r_{ij}$  is the relevant electrooptic coefficient,  $V$  is the applied voltage and  $G$  is the inter electrode gap. Combining (2.17) and (2.18), one gets

$$\Delta\Phi = \frac{\pi}{\lambda} n_o^3 r_{ij} \frac{V}{G} L \Gamma = \pi \frac{V}{V_\pi} \quad (2.19)$$

and

$$V_\pi = \frac{\lambda G}{n_o^3 r_{ij} \Gamma L}. \quad (2.20)$$

$V_\pi$  is a very important parameter for MZM. It is voltage required to induce a phase difference of  $\pi$  rad.



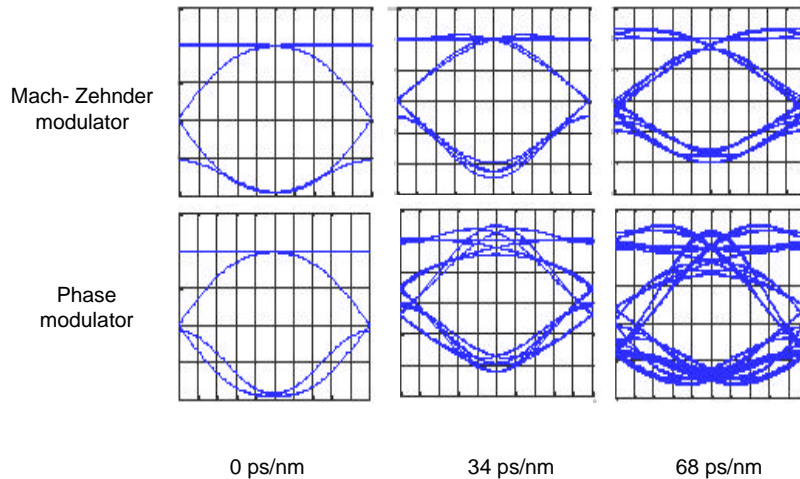
**Figure 2.9:** Three different structures for Mach-Zehnder modulator using x- or z-cut LiNbO<sub>3</sub>

Figure 2.9 shows the different electrode structures used in LiNbO<sub>3</sub>-based MZM's depending on the crystal cut and the propagation direction. In order to exploit the highest electrooptic coefficient, the strongest component of the applied electrical field must be aligned with the z-axis of the crystal. For x-cut LiNbO<sub>3</sub> crystal, an electrical field along the z-directions means a horizontal electrical field whereas for z-cut LiNbO<sub>3</sub> crystal, an electrical field along the z-directions means a vertical electrical field [51–53].

### MZM Versus Phase Modulator

For DPSK signal generation, the MZM is biased at its transmission minimum and needs a voltage swing of  $2V_{\pi}$ . MZM has highly accurate phase modulation at the expense of residual intensity modulation. This results in the intensity dips [8] with the widths depending on the drive signal. Since DPSK encodes the information in the optical phase rather than in the intensity, these dips are absolutely of no importance.

Chromatic dispersion (CD) tolerance (Section 2.3.1) of DPSK signals generated either using a Mach-Zehnder modulator or a phase modulator at the data rate of 40 Gbit/s is evaluated by simulation studies at the chromatic dispersion of 0, 34, and 68 ps/nm. Figure 2.10 shows the simulation results [54]. The DPSK signal generated with Mach-Zehnder modulator exhibits better CD tolerance with respect to the DPSK signal generated using the phase modulator. Therefore, our DPSK transmission setup uses a dual drive MZM at 40 Gbit/s [55].



**Figure 2.10:** Chromatic dispersion tolerance of DPSK using either a Mach-Zehnder modulator or a phase modulator at the data rate of 40 Gbit/s and chromatic dispersion of 0, 34, and 68 ps/nm

### 2.1.3 40 Gbit/s (CS)RZ-DPSK transmitter

Figure 2.11 shows the in-house developed 40 Gbit/s RZ-DPSK transmitter. The electrical part of the transmitter basically employs 16:1 Infineon multiplexer that processes 16 2.5 Gbit/s signals to generate the 40 Gbit/s signal. Tx also uses SHF modulator drivers for the Agere's dual drive data modulator and another dual drive modulator as a pulse carver, driven at half of the clock rate to generate either CSRZ (66% duty cycle) or RZ (33% duty cycle) signals. The details of the Tx are given in the next subsections.

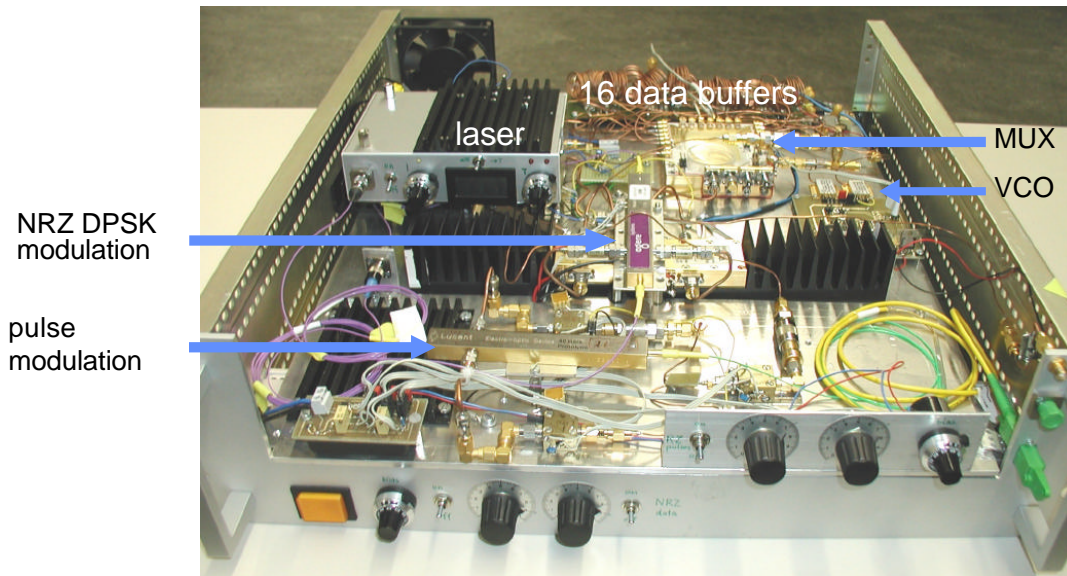


**Figure 2.11:** 40 Gbit/s CSRZ-DPSK transmitter

### Data buffer board

16:1 multiplexer multiplexes 16 data streams at 2.5 Gbit/s to generate 40 Gbit/s  $2^7 - 1$  PRBS data. Therefore, this multiplexer requires a data buffer board that will generate 16 outputs from the Pulse Pattern Generator's (PPG) data output. Data buffer board (Figure 2.12) is designed and developed in-house to provide 16 data output streams which are mutually delayed by multiples of 8 bits.

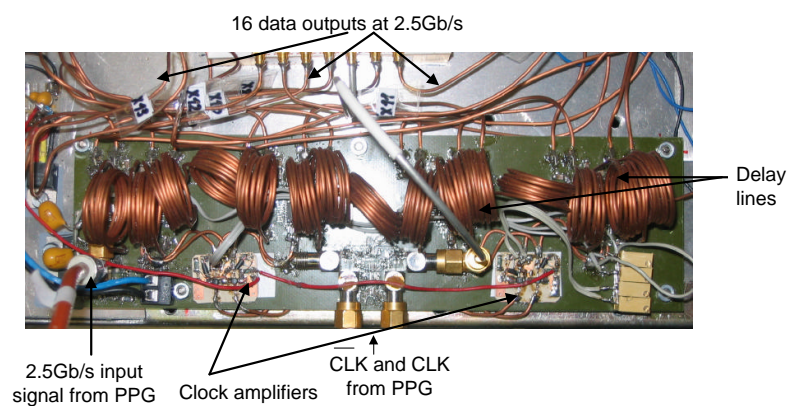


**Figure 2.12:** Photograph of the data buffer board

It is realized on PCB board having 6 layers using the four OnSemi MC100EP131 Quad Master-slaved D flip-flops with common set and separate resets.  $2^7 - 1$  PRBS data is differentially clocked into the flip flops at 2.5 Gbit/s using the PPG clock outputs (CLK and  $\overline{\text{CLK}}$ ). Differential clock signals are amplified before going to the flip-flop inputs using the monolithic amplifiers ERA-1 having a typical gain of 10 dB at 3 GHz.

### **Multiplexer**

The multiplexing is done in a SiGe-based Infineon Multiplexer (MUX) which multiplexes 16 2.5 Gbit/s inputs to a single 40 Gbit/s output. This 16:1 MUX has the conventional tree-type architecture which has built in 16:8, 8:4, 4:2, and 2:1 internal multiplexing units. The input 2.5 Gbits/s data streams are mutually delayed by multiples of 8 bits so that the resulting 40 Gbit/s pattern is also a PRBS pattern.

### **Delay Flip-Flop**

Waveform reshaping and retiming function is done at 40 Gbit/s using the NEL (CI0085B) delay flip-flop (D-FF). It is based on  $0.1 \mu\text{m}$  InP-based HEMT process. It operates up to the data rates of 43 Gbit/s and beyond. For a single ended clock and data input, it provides  $0.9 V_{\text{pp}}$  differential output signals which are directly connected to the two inputs of the SHF modulator drivers that drives the dual drive data modulator.

### **Modulator Driver**

SHF 806E is a modulator driver amplifier having three stage design. Driver is a monolithic microwave integrated circuit hermetically packaged to achieve ultra wide bandwidth and low noise performance. It has gain of  $\sim 26$  dB and bandwidth  $> 38$  GHz. Total power consumption of the driver amplifier is about  $\sim 6$  W and it delivers an output signal having  $8 V_{\text{pp}}$  amplitude into  $50 \Omega$  load.

### **40 Gbit/s LiNbO<sub>3</sub> Electro-Optic Modulator**

Tx uses the distributed feedback (DFB) laser at 192.5 THz. The laser output is connected to the input of the dual drive data modulator. The use of dual drive technology inherently offers the capability to adjust the modulator chirp for ASK mode of operation and chip-free operation for DPSK mode of operation. Dual drive modulators are able to operate in the wavelength range of 1525-1620 nm. They have a maximum optical insertion loss of 6 dB, minimum DC and RF extinction ratios in the order of 20 dB and 14 dB, respectively and minimum bandwidth of 30 GHz. Maximum drive voltage at 1 GHz is about 3 V per side.

### Generation of optical NRZ-DPSK signal

In house developed 40 Gbit/s DPSK transmitter is shown in Figure 2.13. When using a MZM for phase modulation, the modulator is biased at its point of minimum transmission and is driven at *twice* the voltage swing required for ASK mode of operation. If z-cut MZM is used then it is driven in push-pull mode of operation to minimize the chirp, whereas an x-cut modulator requires only a single electrical drive.

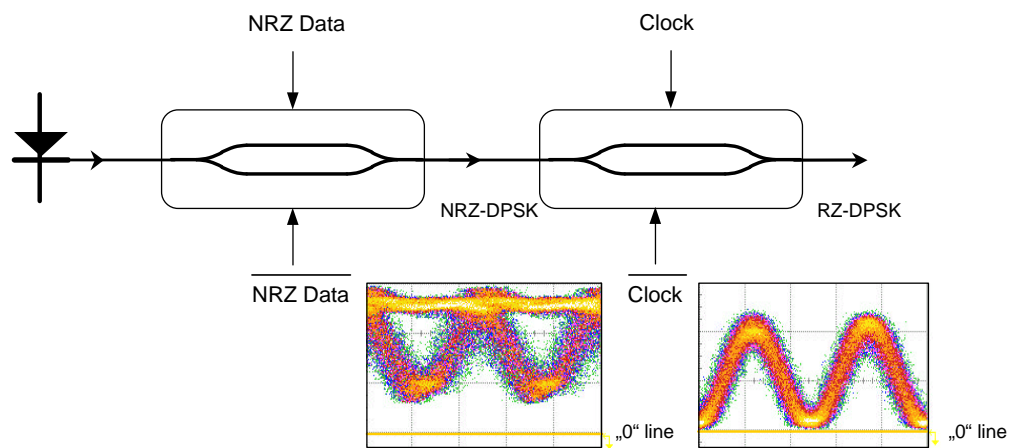


Figure 2.13: DPSK Transmitter using the MZMs

The method of generating the optical binary phase modulation by using a dual-drive MZM is shown in Figure 2.14. Since the phase of the optical field changes its sign upon transitioning through a minimum in the MZMs power transmission curve, two neighboring intensity maxima have opposite optical phases, and a near-perfect  $180^\circ$  phase shift is obtained, *independent* of the drive voltage swing. The benefit of highly accurate phase modulation comes at the expense of some residual intensity modulation at the transition of two bits, with the width of the resulting intensity dips depending on the drive signal's bandwidth and voltage. However, DPSK encodes information in the optical phases rather than in the intensity, these dips are of no importance, especially for RZ-DPSK.

A digital "1" is represented by a  $\pi$  phase change between the consecutive data bits in the optical carrier, while there is no phase change between the consecutive data bits in the optical carrier for a digital "0". For NRZ-DPSK signal optical power is constant, however the optical field shifts between "1" and "-1", that what it differs from ASK, where the optical field shifts between "1" and "0".

To improve system tolerance to nonlinear distortion and to achieve a longer transmission distance (higher sensitivity), instead of NRZ-DPSK, return-to-zero DPSK (RZ-DPSK) is often used. But, to generate the RZ-DPSK optical signal, one more intensity modulator needs to be used as pulse carver.

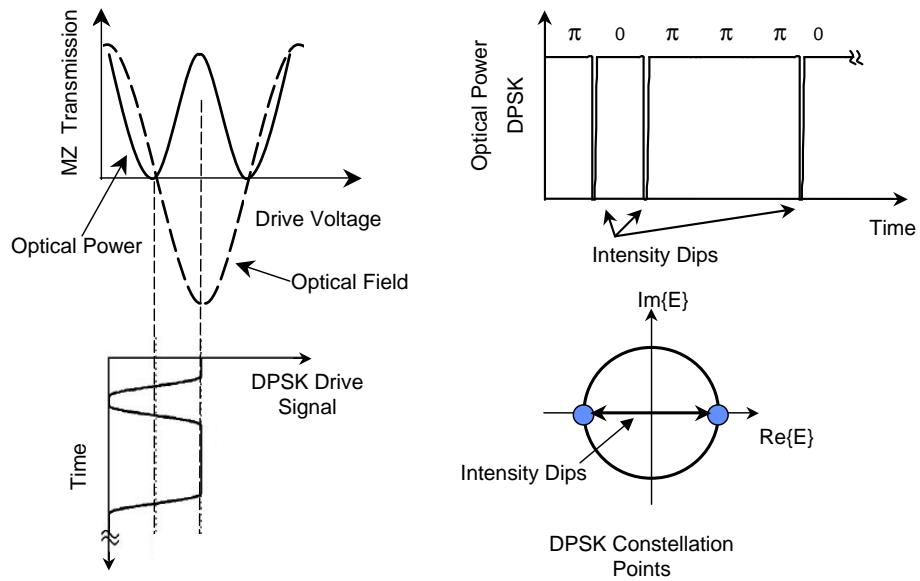


Figure 2.14: DPSK signal generation

### Generation of optical (CS)RZ-DPSK Signal

(CS)RZ-DPSK signal is generated in our transmitter using another dual drive modulator driven with a sinusoidal signal at half of the clock rate. Figure 2.15.a shows the method of generating the 66% and 33% RZ signals by biasing the modulator at transmission minimum and maximum respectively, and driving the modulator with a sinusoidal signal with a maximum drive voltage swing of  $2V_{\pi}$  for both cases. Figure 2.15.b shows the resulting intensity pulses for both the 33% and 66% (CS)RZ pulses.

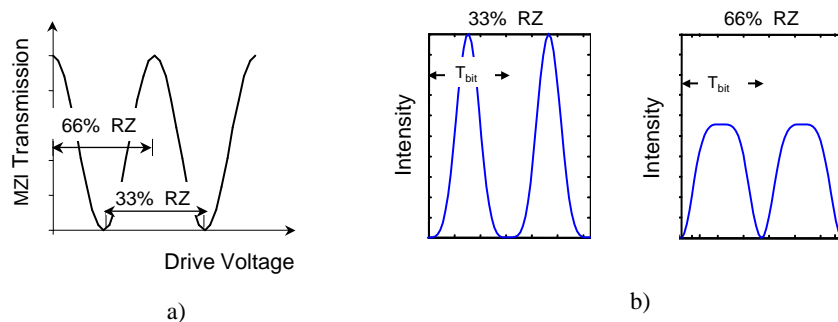


Figure 2.15: a)Transmission characteristic of MZM b)Optical intensity generated signals

### 2.1.4 Experimental Results

To judge the quality of the modulation, NRZ- and RZ-DPSK optical signals are first generated using the developed hardware and then received using two high-speed photodiodes. Output of the two photodiodes are directly connected to a 50 GHz oscilloscope. The oscilloscope was triggered with the transmitter clock at 2.5 GHz to view the eye diagrams at 40 Gb/s. The exemplary NRZ- and RZ-DPSK eye diagrams at the transmitter side are shown in Figure 2.13.

Since the pulse width of the (CS)RZ-DPSK signal is narrower than that of the NRZ-DPSK signal, the (CS)RZ-DPSK pulse has higher peak power than the NRZ-DPSK for a given average power. Thus, the eye opening of the (CS)RZ-DPSK signal format is wider than that of the NRZ-DPSK (inset Figure 2.13), resulting in better receiver sensitivity than the NRZ-DPSK for a given average power [23]. This implies that for a required receiver sensitivity, the transmitted power can be lowered by employing the (CS)RZ-DPSK signal format rather than the NRZ-DPSK. The better receiver sensitivity in the case of the (CS)RZ signal also suggests that the transmission distance can be increased compared with the NRZ-DPSK signal for the same transmitted power.

## 2.2 oDPSK signal detection

A typical optically pre-amplified balanced DPSK receiver is shown in Figure 2.16. The optical signal is first amplified using a pre-amplifier. Then it passed through an optical band pass filter in order to improve the optical signal-to-noise ratio before it enters the Mach-Zehnder delay-interferometer (MZDI), whose differential delay is set equal to the bit period. This optical signal preprocessing is necessary in direct-detection receivers to accomplish demodulation, since the photodetection process is insensitive to the optical phase; a detector only converts optical intensity modulation into an electrical signal.

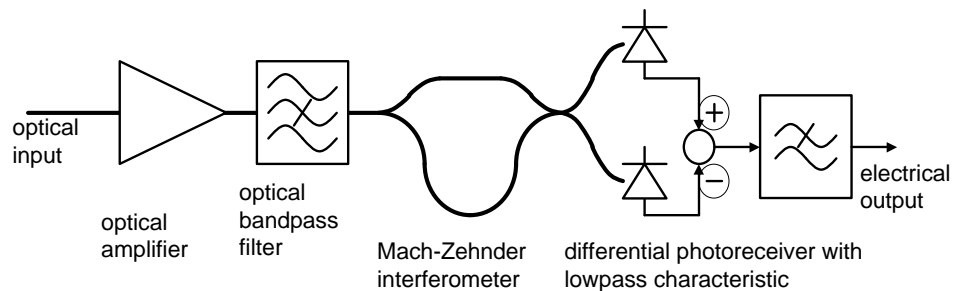


**Figure 2.16:** DPSK optical receiver

In direct-detection DPSK receiver, the MZDI lets two adjacent bits interfere with each other at its output port. This interference leads to the presence (absence) of power at a MZDI output port if two adjacent bit interfere constructively (destructively) with each other. Thus, the preceding bit in a DPSK encoded bit stream acts as the phase reference for demodulating the current bit. Two MZDI output ports generally carry identical, but logically inverted data streams under DPSK modulation. MZDI's can be fiber based or else could be implemented as a planer lightwave circuit (PLC) technology.

The DPSK using balanced detection, has the most obvious benefit. It exhibits 3 dB lower OSNR required to reach a given BER compared to conventional ASK. At a BER of  $10^{-9}$ , the quantum limit for an optically preamplified ASK receiver is 38 photons/bit [56], however only 20 photons/bit are needed for the optically preamplified balance DPSK receiver [13]. A receiver sensitivity of 36.2 dBm (45 photons/bit) was reported for a 42.7 Gb/s optically preamplified return-to-zero DPSK signals [11]. However, the reported record sensitivity is 38 photons/bit at 42.7 Gb/s once again using RZ-DPSK signals [12].

### 2.2.1 Mach-Zehnder Interferometer Modelling

A Mach-Zehnder delay interferometer (MZDI) consists of a input 2x2 coupler, an output 2x2 coupler and two waveguide branches in between them with unequal optical path length difference corresponding to the integer multiples of bit duration (Figure 2.17). Thus, the MZDI's power transfer matrix is given by

$$S_{MZDI} = [S_{coupler}][S_{branches}][S_{coupler}]. \quad (2.21)$$

The upper arm of the Mach-Zehnder interferometer is a direct connection and the lower arm contains the delay including the phase adjustment.

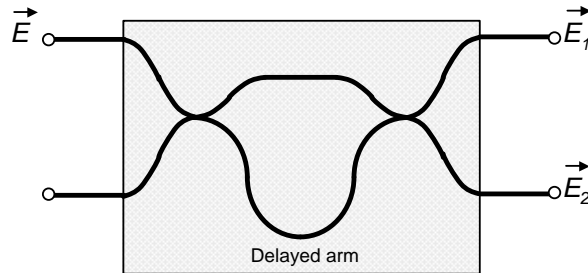


**Figure 2.17:** Simplified Interferometer model with delay T and retardation R in the lower branch

As the both branches are summarized by

$$[S_{branches}] = \begin{bmatrix} 1 & 0 \\ 0 & e^{-(j\omega T + \varphi)} \end{bmatrix} \quad (2.22)$$

the equation (2.21) becomes

$$S_{MZDI} = \frac{1}{\sqrt{2}} \begin{bmatrix} 1 & -j \\ -j & 1 \end{bmatrix} \begin{bmatrix} 1 & 0 \\ 0 & e^{-(j\omega T + \varphi)} \end{bmatrix} \frac{1}{\sqrt{2}} \begin{bmatrix} 1 & -j \\ -j & 1 \end{bmatrix} \quad (2.23)$$

If the electrical field at the MZI input is  $\vec{E}(t)$ , both output arms of the splitter in the MZI carry electric fields  $\vec{E}(t)/\sqrt{2}$ . Therefore the output fields at the the two photodiodes are

$$\vec{E}_1(t) = \frac{1}{2} \left( \vec{E}(t) + \vec{E}(t - T) \right) \quad (2.24)$$

and

$$\vec{E}_2(t) = \frac{1}{2} \left( -j\vec{E}(t) + j\vec{E}(t - T) \right) \quad (2.25)$$

As the two adjacent bits interfere with each other at the MZDI output ports, the optical output of the Mach-Zehnder delay interferometer is either a constructive or a destructive interference depending on the relative phase difference between  $\vec{E}(t)$  and  $\vec{E}(t - T)$ . The signals measured by the two photodiodes are

$$|\vec{E}_1(t)|^2 = \left[ \frac{\vec{E}(t) + \vec{E}(t - T)}{2} \right]^2 \quad (2.26)$$

and

$$|\vec{E}_2(t)|^2 = \left[ \frac{\vec{E}(t) - \vec{E}(t - T)}{2} \right]^2 \quad (2.27)$$

For the difference of intensities at the two photodiode outputs, one can write

$$|\vec{E}_1(t)|^2 - |\vec{E}_2(t)|^2 = \text{Re}(\vec{E}^+(t) \cdot \vec{E}(t - T)). \quad (2.28)$$

Polarization matching is achieved by a polarization-independent design of the MZDI.

## 2.2.2 40 Gbit/s RZ-DPSK receiver

In the receiver, after passing an optical preamplifier (EDFA) and an optical BPF filter (Figure 2.16), the optical signal enters a commercial Mach-Zehnder interferometer having four bit delay (NEL). This allows us to differentially encode the data at 10 Gbit/s in the transmitter (Section 2.1.1). The two outputs from the Mach-Zehnder interferometer are connected to two high-speed photodiodes from u2t.

A variable electrical delay line was used to adjust the path length difference between the two photodiode outputs. The two photodiode outputs are directly connected to the differential inputs of a Infineon demultiplexer having standard clock and data recovery circuits (CDR). From the received NRZ data stream, either at 40 or at 43 Gbit/s, CDR recovers the clock and data. Demultiplexer demultiplexes the 40 Gbit/s data to  $16 \times 2.5$  Gbit/s data streams. Additional details about the components used in the DPSK receiver are given in the following subsections.

### **Mach-Zehnder Interferometer**

NEL Mach-Zehnder delay interferometer (MZDI) is planar lightwave circuit (PLC) based on silica on silicon waveguide technology. It is stable against mechanical vibration. The MZDI is temperature stabilized at  $45^\circ\text{C}$  using a proportional integral (PI) temperature controller. The free spectral range of the interferometer is 10 GHz. Its phase tuning speed is in the range of 2-3 ms and the tuning range is between  $0 - 2\pi$  rad. Its insertion loss is  $\leq 3.5$  dB and extinction ratio is  $> 17$  dB. The phase tuning is accomplished by using the differential micro-heaters with total constant power.

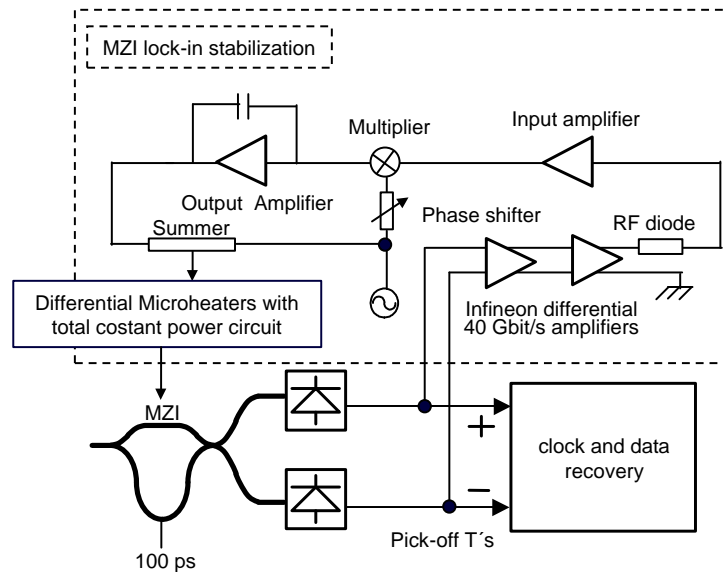
### **Photo Receiver**

The u2t (XPDV202R) photodiodes have bandwidths  $> 50$  GHz and the responsivities of 0.68 A/W. The maximum dark current is 500 nA. Photodiodes are equipped with an internal  $50 \Omega$  resistor between RF-signal and ground, so they can be biased via the bias-pin and ground-pin regardless of a measurement unit being connected. Typically, a bias voltage in the order of 2 V is needed. The maximum allowed optical input power is 20 mW. The average photocurrent on each detector was about 2.5 mA which corresponds to average optical power of  $\approx 5$  dBm.

### **Lock-In Stabilization Scheme**

To make the delay interferometer more stable and more robust against the existing small polarization dependent phase shift, the lock-in stabilization scheme was first proposed and later implemented by R. Noè, using the existing lock-in amplifier board. Parts of the photodiode output signals are tapped off using pick-off T's and sent through the 40 Gbit/s Infineon differential amplifiers for subsequent AC power detection. Detected RF power is at its maximum when the interferometer phase difference is set to  $0^\circ$ . The DC voltage that controls the differential micro-heaters with total constant power was therefore added with a small signal 400 Hz tone to thermally modulate the interferometer phase difference for subsequent lock-in stabilization. The detected RF power was synchronously detected using a lock-in amplifier which utilizes an AD734 as an analog multiplier. The reference signal was fed into the second input of the multiplier. An additional phase shifting network was used in the reference path for obtaining the best sensitivity from the lock-in amplifier.

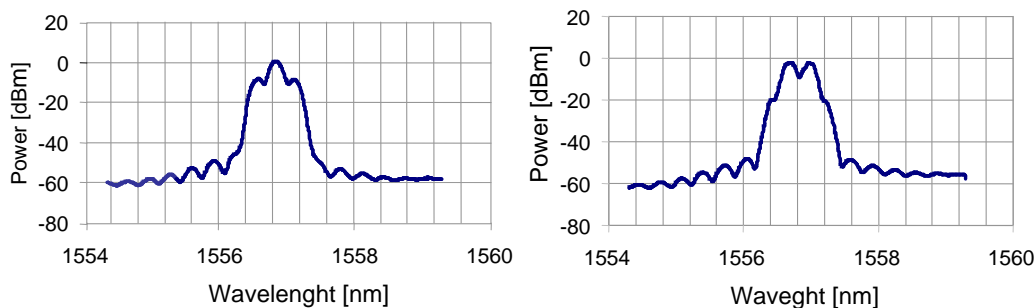
The multiplier's output signal was low pass filtered using a proportional integrator whose output finally controls the interferometer phase difference. Due to lock-in stabilization scheme (Figure 2.18), when the interferometer phase difference is set optimally by the controller, the eye diagram is open and the 400 Hz tone is absent. An opposite thing happens, when the phase difference is set incorrectly, so that the eye diagram is closed and the 400 Hz tone is present.



**Figure 2.18:** Block diagram of the lock-in amplifier's scheme

### 2.2.3 Measurement results

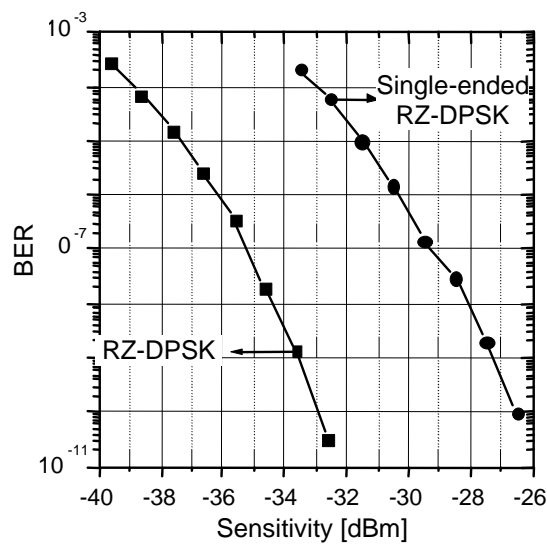
The measured results show that difficulties in implementing stable delay interferometers [57] have been overcome using the proposed lock-in stabilization scheme. This 400 Hz lock-in stabilization scheme for the interferometer phase essentially eliminates the impact of a small polarization-dependence of the interferometer phase shift.



**Figure 2.19:** Optical spectrum at the constructive port (left) and destructive port (right)

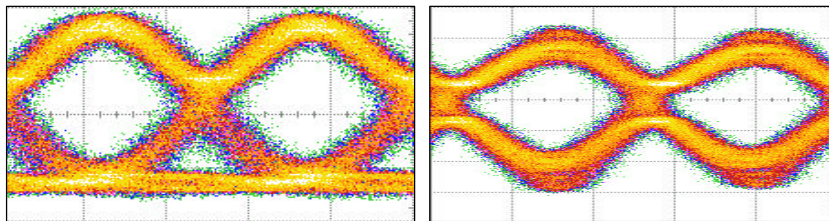
The interferometer phase difference could be continuously fine-tuned in order to match the laser center frequency. As mentioned above, the two MZDI's output ports carry inverted data streams. Figure 2.19 shows the optical spectrum recorded at constructive and destructive port of the MZDI in a direct-detection DPSK receiver. Since both ports carry the full (only inverted) information, they can be detected either using a so called "single-ended detection" or using "balanced detection".

Figure 2.20 shows the experimentally measured BER curves for balanced detection as well as single-ended detection of (CS)RZ-DPSK signals using in-house developed optically pre-amplified receiver. The corresponding back-to-back receiver sensitivities are  $-33.5$  dBm and  $-27.5$  dBm.



**Figure 2.20:** BER vs. power at optical preamplifier input for different CS-RZ DPSK modulation format

Figure 2.21 shows the measured back-to-back eye diagrams for NRZ-DPSK as well as for CSRZ-DPSK signals.



**Figure 2.21:** 40 Gbit/s eye diagrams back-to-back for NRZ-DPSK (left) and (CS)RZ-DPSK (right)

## 2.3 Signed On Line Chromatic Dispersion Detection

Tunable chromatic dispersion (CD) compensation is often needed in long-haul and dynamically routed transmission links, especially at 40 Gbit/s and beyond. Among many CD detection schemes, a synchronous arrival time detection was implemented for intensity-modulated systems [58]. In this scheme arrival time modulations caused by a small frequency modulation in the presence of CD are synchronously detected in the clock recovery phase locked loop (PLL). In this work, it is demonstrated that this signed online CD detection scheme also works for the DPSK modulation format, even with an interferometer having 100 ps delay [59].

### 2.3.1 Chromatic Dispersion in Single Mode Fibers

The main advantage of single-mode fibers is that intermodal dispersion is absent simply because the energy of the injected pulse is transported by the single optical mode. However, the pulse broadening does not disappear altogether. The group velocity associated with the fundamental mode is frequency dependent because of chromatic dispersion. As a result different spectral component of the pulse travels slightly different group velocities, a phenomenon referred to as the *Group Velocity Dispersion* or simply the linear fiber dispersion.

The concept of chromatic dispersion (CD) or group velocity dispersion can be understood as follows: the complex field transfer function of an optical fiber of length  $L$  is

$$\underline{H}(\omega) = e^{-j\beta(\omega)L} \quad (2.29)$$

where  $\beta (= \bar{n}k_0 = \bar{n}\omega/c)$  is the propagation constant,  $\bar{n}$  is the modal index and  $\omega$  is the optical angular frequency.

It's phase can be approximated, by neglecting the fiber attenuation, by the truncated Taylor series expansion as

$$\varphi = -\beta(\omega) \cdot L = (\beta + (\omega - \omega_0)\beta' + \frac{1}{2}(\omega - \omega_0)^2\beta'') \cdot L. \quad (2.30)$$

At  $\omega_0$  the propagation constant  $\beta(\omega)$  assumes the value  $\beta$ , its first and second derivative with respect to  $\omega$  are  $\beta'$  and  $\beta''$ , respectively. The group delay

$$\tau_g = -\varphi' = (\beta' + (\omega - \omega_0)\beta'') \cdot L \quad (2.31)$$

is a linear function of  $\omega$ . It's derivative with respect to wavelength  $\lambda$  and length  $L$  is the chromatic dispersion coefficient

$$D = \frac{d^2\tau_g}{d\lambda \cdot dL} = -\frac{2\pi c}{\lambda^2}\beta'' \quad (2.32)$$

The  $\beta''$  in (2.32) is nothing but the derivative of  $V_g^{-1}(= d\beta/d\omega)$  with respect to  $\omega$ , where the group velocity  $V_g$  is given by  $V_g = c/\bar{n}_g$ . The group index  $\bar{n}_g = \bar{n} + \omega(d\bar{n}/d\omega)$ .

Therefore, the wavelength dependence of  $D$  as shown in (2.32) is in fact governed by the frequency dependence of the modal index  $\bar{n}$  and can be written as [60]

$$D = -\frac{2\pi c}{\lambda^2} \frac{d}{d\omega} \left( \frac{1}{V_g} \right) = -\frac{2\pi}{\lambda^2} \left( 2 \frac{d\bar{n}}{d\omega} + \omega \frac{d^2\bar{n}}{d\omega^2} \right). \quad (2.33)$$

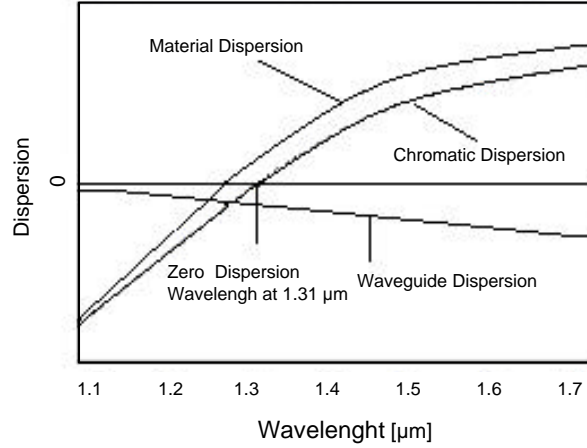


**Figure 2.22:** Total dispersion  $D$  and relative contributions of material dispersion  $D_m$  and waveguide dispersion  $D_w$  for a conventional single mode fiber

Generally,  $D$  can be written as the sum of the two terms  $D = D_m + D_w$ , where  $D_m$  and  $D_w$  are material and the waveguide dispersions, respectively. Material dispersion occurs because the refractive index of silica, the material used for fiber fabrication changes with the optical frequency  $\omega$ , while the waveguide dispersion arises because the way in which the waves match the boundary conditions at the core-cladding interface depends on their frequency. As a result, their propagation phase velocity is a function of frequency, independent of any material effects. Another way of understanding this is to recognize that, in monomode fibers, a significant fraction of the optical power propagates in the cladding. As the frequency varies, so the propagation of the power travelling in the cladding changes, and so the average refractive index experienced by the waves also changes. Figure 2.22 shows  $D_m$ ,  $D_w$  and their sum,  $D = D_m + D_w$  for standard single mode fiber.

### 2.3.2 Measurement Setup for Chromatic Dispersion Detection

Adjustable drop-in CD compensator requires a signed online CD detection. For this purpose the DFB transmitter laser is frequency-modulated at 5 MHz with a 224 MHz (rms) frequency deviation, and a parasitic 1.2% (rms) amplitude modulation. Figure 2.23 shows the 40 Gbit/s in-house developed CSRZ-DPSK transmission setup with signed online chromatic dispersion detection.

In the presence of chromatic dispersion (CD), the frequency modulation (FM) causes a small arrival time modulation which is indicated by the clock phase error signal. This arrival time signal is synchronously detected using a multiplier and averaging circuit. A low-frequency monitor photodiode with bandpass filter at 5 MHz detects the amplitude modulated (AM) reference signal for a 5 MHz lock-in detection of the clock phase error signal coming from the clock recovery phase locked loop (PLL).

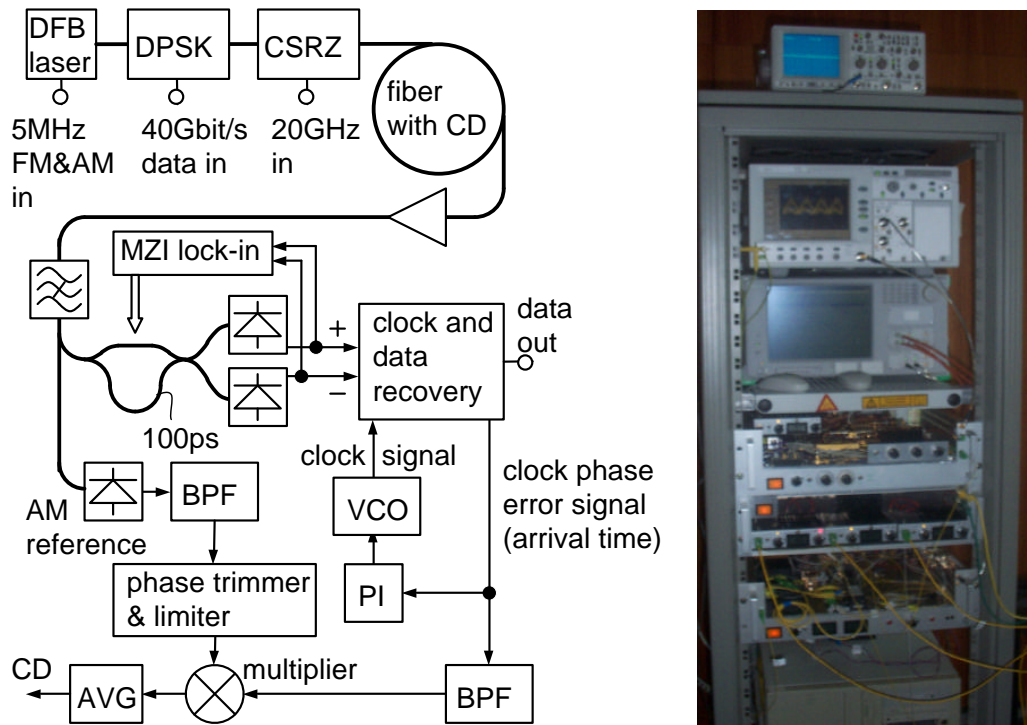
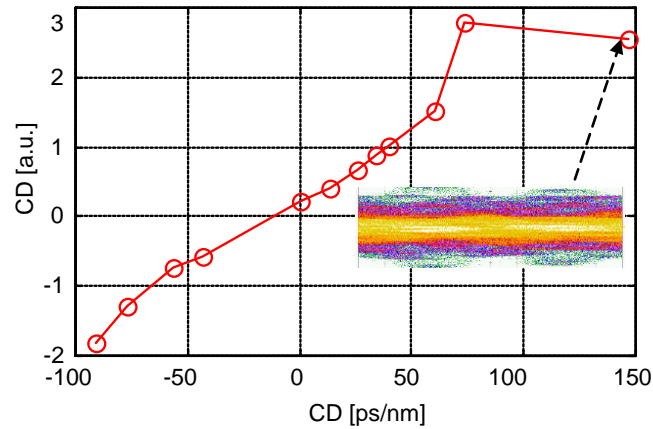


Figure 2.23: Experimental 40 Gbit/s CSRZ-DPSK setup for chromatic dispersion detection

### 2.3.3 Experimental results

The function of the chromatic dispersion detection is verified by inserting various fiber pieces. Figure 2.24 shows the CD readout as a function of true CD in the range  $-91$  ps/nm  $\dots$   $+147$  ps/nm. The readout is fairly linear in the range where the eye diagram is fairly open. The sign of the CD is faithfully returned even when the eye diagram is closed (inset Figure 2.24) as long as the clock phase detector works, the PLL locks, and there is a high-enough percentage of correct data decisions. Since the sign of the CD is preserved, the CD error signal could be directly used to control an adaptive CD compensator via an integral controller.



**Figure 2.24:** Chromatic dispersion detection readout vs. actual dispersion. Inset: eye diagram resulting from interferometer output signal difference

The readout noise (rms) at zero CD (Figure 2.25), ranges from 4 ps/nm to <100 fs/nm for measurement intervals between 38  $\mu$ s and 157 ms. The  $2^7 - 1$  PRBS yielding slightly better results than a  $2^{23} - 1$  PRBS.

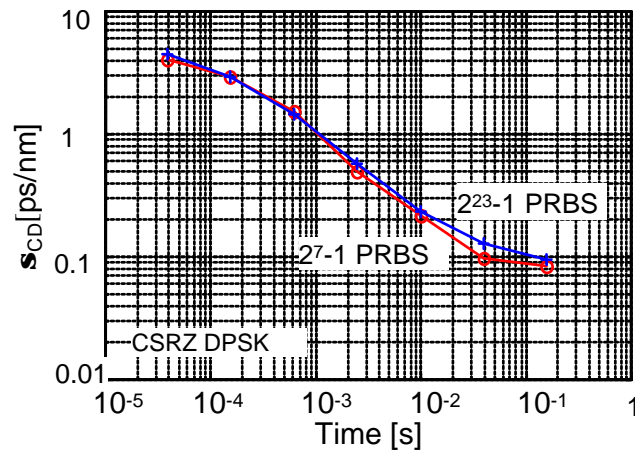


**Figure 2.25:** Standard deviation versus measurement interval, at zero actual dispersion

The eye diagrams back to back at each photodiode and their difference are shown in Figure 2.26 (left). The eye diagrams after 91 km of transmission are also shown in Figure 2.26 (right).

The Q factor is 24 dB for 17 ps CSRZ pulses. For 8 ps RZ pulses were also tried out and yielded a  $Q > 28$  dB. The CSRZ-DPSK signal was also transmitted over 58 km of SSMF, 33 km of DSF, and some DCF. The Q factor after transmission was always  $> 22$  dB.

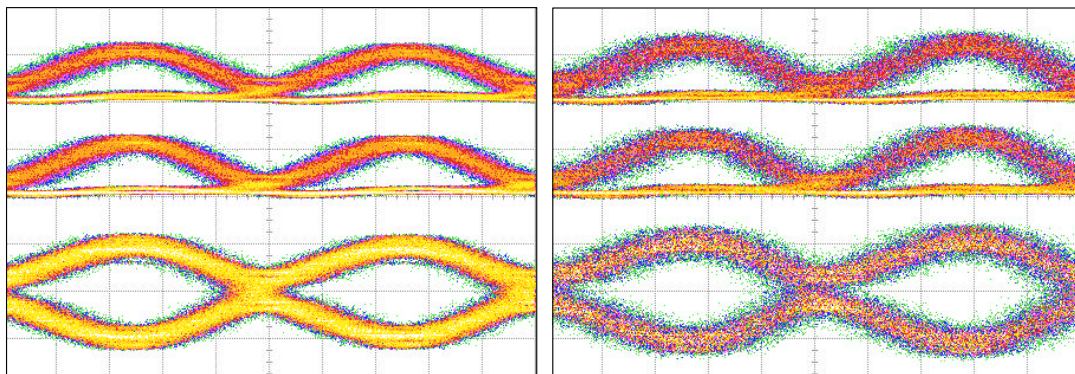


**Figure 2.26:** CSRZ-DPSK eye diagrams at interferometer outputs (top), and difference signal (bottom) back to back (left) after transmission over the 91km (right)

Compared to the recently reported method [61], the employed CD detection scheme [58] needs a much smaller frequency modulation. This means reduced parasitic amplitude modulation and is of course advantageous in densely packed WDM environments. Thus, a small FM was applied to the transmitter DFB laser allows us to measure chromatic dispersion online in sub-ms intervals, including its sign. Therefore, the required frequency deviation is so small that this scheme can be applied to DPSK modulation format even with an interferometer having 100 ps delay.

## 2.4 Chromatic Dispersion Compensation

At 40 Gbit/s, chromatic dispersion is the main limiting factor, as the system tolerance is reduced to 1/16 of that at 10 Gbit/s [62]. Temperature changes can lead to variations in dispersion that may be significant enough to degrade system performance. Therefore an accurate, tunable CD compensation is often required. Various types of integrated optical dispersion compensators [63–67] have been demonstrated but, the fiber Bragg grating-based dispersion compensators exhibit the largest dispersion range and lowest insertion loss with an associated tunability.

### Fiber Bragg Grating

The significant discovery of photosensitivity in optical fibres led to the development of a new class of in-fibre components, called the fibre Bragg gratings (FBGs). In its simplest form a fiber Bragg grating consists of a periodic modulation of the index of refraction in the core of a single-mode optical fiber. These types of uniform fiber gratings, where the phase fronts are perpendicular to the fiber's longitudinal axis and with grating planes having constant period, are considered as the fundamental building blocks for most of the

fiber Bragg grating structures. Generally, if the light propagating in the fiber core having the above mentioned refractive index modulation satisfies the well known Bragg's condition then and only then it is strongly coherently reflected back.

The Bragg grating condition is simply the requirement that satisfies both energy and momentum conservation principles. Energy conservation ( $\hbar\omega_i = \hbar\omega_r$ ) requires that the frequency of the incident radiation and the reflected radiation is the same [68]. Momentum conservation requires that the incident vector  $\mathbf{k}_i$ , plus the grating vector,  $\mathbf{K}$  equal the wavevector of the scattered radiation  $\mathbf{k}_r$ . This is simply stated as

$$\mathbf{k}_i + \mathbf{K} = \mathbf{k}_r, \quad (2.34)$$

where the grating wavevector,  $\mathbf{K}$ , has a direction normal to the grating planes with a magnitude  $2\pi/\Lambda$  ( $\Lambda$  is grating spacing shown in Figure 2.27).

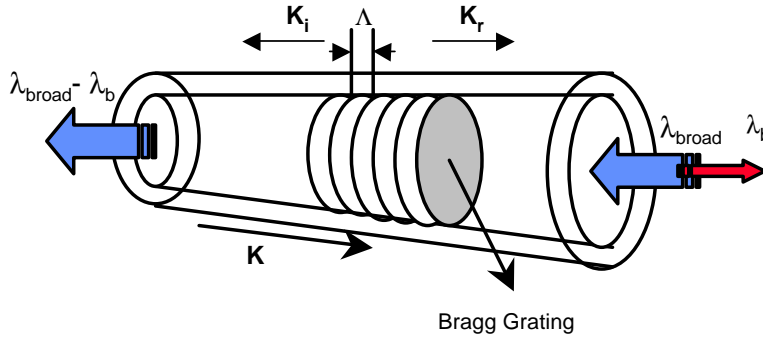


**Figure 2.27:** Illustration of a uniform grating with constant amplitude of refractive index modulation and grating period

The diffracted wavevector is equal in magnitude, but opposite in direction, to the incident wavevector. Thereby, for the momentum conservation condition stands

$$2 \left( \frac{2\pi n_{\text{eff}}}{\lambda_B} \right) = \frac{2\pi}{\Lambda} \quad (2.35)$$

which simplifies to the first-order Bragg condition

$$\lambda_B = 2n_{\text{eff}}\Lambda \quad (2.36)$$

where the Bragg grating wavelength,  $\lambda_B$ , is the free-space center wavelength of the input light that will be reflected from the Bragg grating, and  $n_{\text{eff}}$  is the effective refractive index of the fiber core at the free space center wavelength.

Consider a uniform Bragg grating formed within the core of an optical fiber with an average refractive index  $n_0$ , the index of refractive profile can be expressed as

$$n(z) = n_0 + \frac{1}{2}\Delta n_{pp}(z) \cos\left(\frac{2\pi}{\Lambda}z + \phi(z)\right), \quad (2.37)$$

where  $\Delta n_{pp}(z)$  is the gratings peak to peak refractive index modulation amplitude (typical values  $10^{-5}$  to  $10^{-3}$ ), and  $\phi(z)$  is the grating phase.  $L$  is the grating length, and  $z$  is the distance along the fiber longitudinal axis.

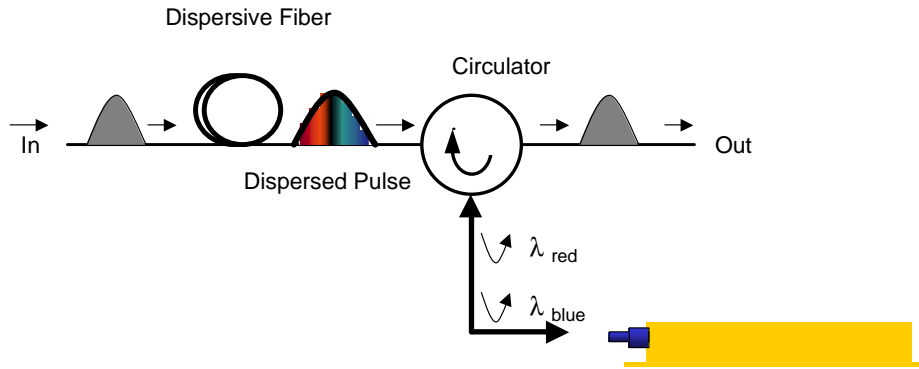


**Figure 2.28:** Principle of FBG CD compensator with circulator

Devices with the fiber Bragg grating are often used in conjunction with optical circulator. The light normally enters the circulator input port (1) and appears at the second port (2), which is connected to the FBG. Then, the light travels through the FBG and reflects back to port 2. The light that enters the port 2 is routed to output port (3) (Figure 2.28). The fiber Bragg grating introduces the negative dispersion to clean the spectrum of the dispersed signal. Dispersion compensators based on optical FBGs are now commercially becoming the promising candidates for tunable dispersion compensation [69, 70]. The advantages of FBGs are large nonlinear tolerance and lower device insertion loss. The main drawback associated with the FBG-based dispersion compensators is distortions arising from the residual amplitude and phase ripples of the Bragg grating as well as the increased system complexity due to the fact that such compensators need high resolution temperature controllers for their operation.

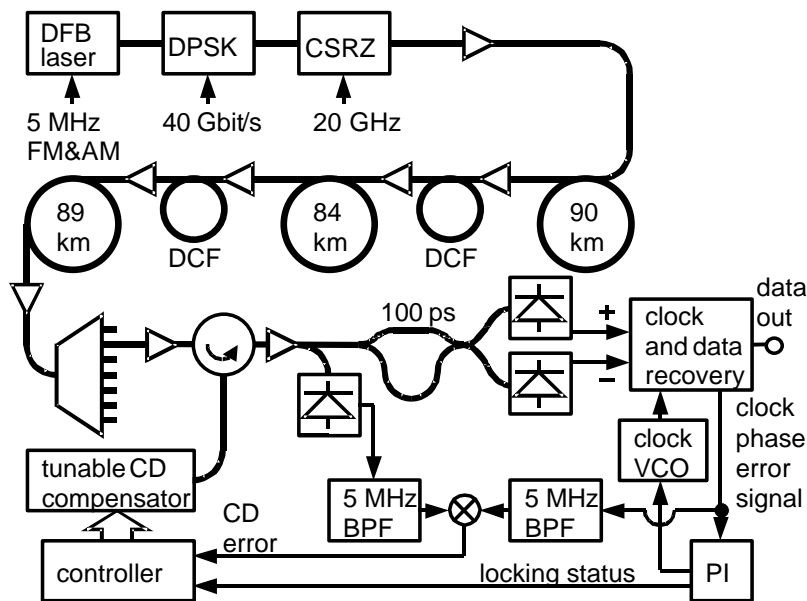
### 2.4.1 Adaptive Tunable CD Compensation

Tunable chromatic dispersion (CD) compensation is needed in long haul and dynamically routed transmission links, especially at 40 Gbit/s. Among many CD detection schemes, synchronous arrival time detection with a sensitivity of at least 200 attoseconds [58] is the most promising option because the scheme has an extremely low incremental cost, provides the sign of CD and is usable for various modulation formats [59].

The tolerance to residual CD with respect to in-line CD compensation ratio for various modulation formats including NRZ-ASK, CSRZ-ASK, NRZ-DPSK and CSRZ-DPSK was evaluated numerically in [71] at 43 Gbit/s. But in [23], it is for the first time reported on automatic chromatic dispersion compensation for all these modulation formats in a 40 Gbit/s transmission experiment, using a thermally tunable dispersion compensator. The fully automatic residual chromatic dispersion compensation is reported for a fiber link with fibers up to 263 km in length for NRZ-DPSK as well as CSRZ-DPSK modulation formats at 40 Gbit/s, using synchronous arrival time detection and a thermally tunable dispersion compensator.

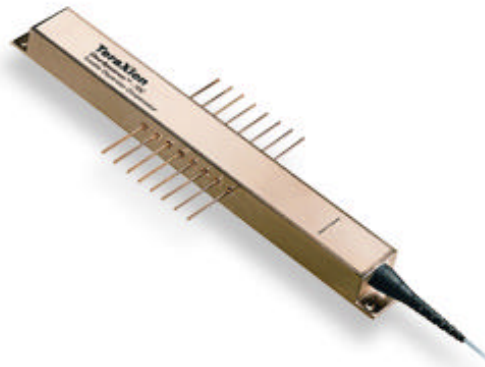
### Transmission setup

Figure 2.29 shows 40 Gbit/s DPSK transmission setup for adaptive tunable CD compensation. A DFB laser at 192.5 THz (1557.366 nm) is modulated with a 5 MHz sinusoidal source to provide 1.8% (rms) power modulation and 336 MHz (rms) frequency modulation. A 40 Gbit/s  $2^7 - 1$  PRBS is impressed on the optical carrier to generate NRZ-DPSK or CSRZ-DPSK signal for transmission (Section 2.1.3).



**Figure 2.29:** CDC Setup for 40 Gbit/s DPSK transmission

This signal is transmitted over three fiber spans with a total length of 263 km. The spans were mixed from 170 km of SSMF, 60 km of NZDSF, and 33 km of DSF. DCF with a total dispersion of  $-2713$  ps/nm was inserted between first and second stages of the two inline EDFA's.



**Figure 2.30:** Photograph of the TeraXion thermally tunable dispersion compensator

At the receiver end, there is an 980 nm optical preamplifier followed by a 40 channel, flat top wavelength division Optun de-multiplexer which is being used as a narrow band optical band pass filter. The TeraXion tunable dispersion compensator (TDC) (Figure 2.30) is inserted just before the receiver using a three-port optical circulator. This single-channel TDC [69] at 192.5 THz is based on thermally tunable chirped FBG. The dispersion tuning range of device is between -300 and -700 ps/nm. Insertion loss excluding circulator loss is less than 1.5 dB. Figure 2.31 shows the group delay versus wavelength in tunable chromatic dispersion compensator for various dispersion settings.

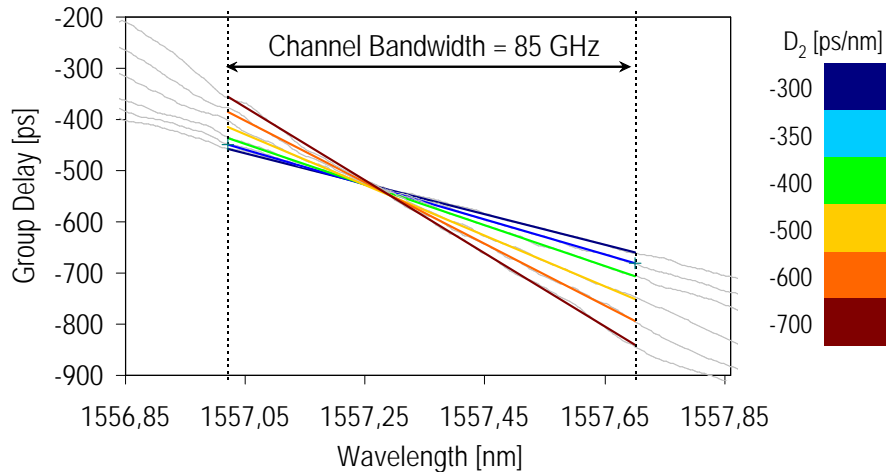


**Figure 2.31:** Group delay versus wavelength in tunable CD compensator for dispersion settings

An optical tap and a low frequency power monitor photodiode is used to recover the power modulation whose output is being used as a reference signal for arrival time detection followed the dispersion compensator. DPSK signals are decoded using a Mach-Zehnder interferometer having a 100 ps delay. Both interferometer outputs are connected to high-speed photodiodes, which in turn are connected to the differential inputs of an Infineon clock and data recovery circuit with 1:16 DEMUX.

BERs in even and odd DEMUX channels are about the same. For ASK operation, the interferometer and one photodiode is left out. In the presence of CD, the FM causes small arrival time modulation, which is indicated by the clock phase error signal. The CD error signal is directly proportional to the residual CD including its sign.

### Experimental Results

In order to keep the CD readout independent of optical input power fluctuations, the detected photocurrent is stabilized by feedback loop that controls the pump current of the last EDFA. Figure 2.32 shows OSNRs in dB/0.1nm, which all result in BER =  $10^{-9}$ . They are given as a function of a manually adjusted compensator CD with a fiber link of 258 km in place.

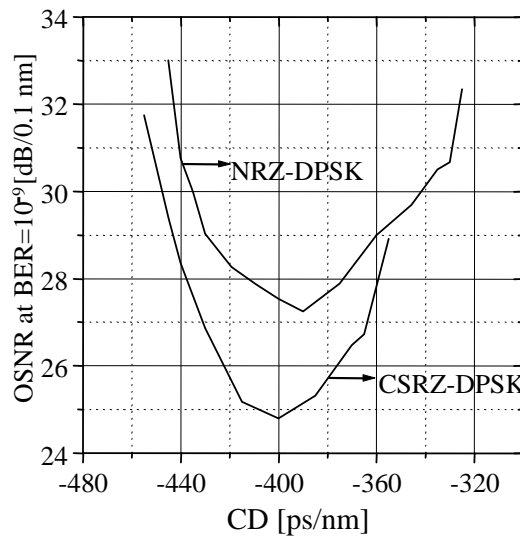


**Figure 2.32:** OSNR needed for BER =  $10^{-9}$  versus compensator CD

Automatic CD compensation is carried out by a Digital Signal Processor (DSP) in the following way: at first, the dispersion compensator is thermally scanned through its  $-300$  ps/nm to  $-700$  ps/nm CD tuning range. Then it is set into the middle of that region where the clock recovery PLL locks successfully. Finally, an integrator controls the value of the CD. The integrator input is driven by the CD error signal. Integration stalls when the CD error signal vanishes and indicates zero residual CD. Temporal variations of CD are automatically tracked. The electrical heating/cooling power required to control and tune the compensator is 10 W. A thermal scan takes 10 minutes, and the control time constant is about 45 s, but control speed was not optimized.

The back-to-back Q values for NRZ-DPSK and CSRZ-DPSK are 25.8 and 29.5 dB, respectively. The corresponding back-to-back receiver sensitivities of  $-26.8$ , and  $-32.1$  dBm are equivalent to OSNRs of 29.6, and 23.8 dB/0.1nm, respectively.

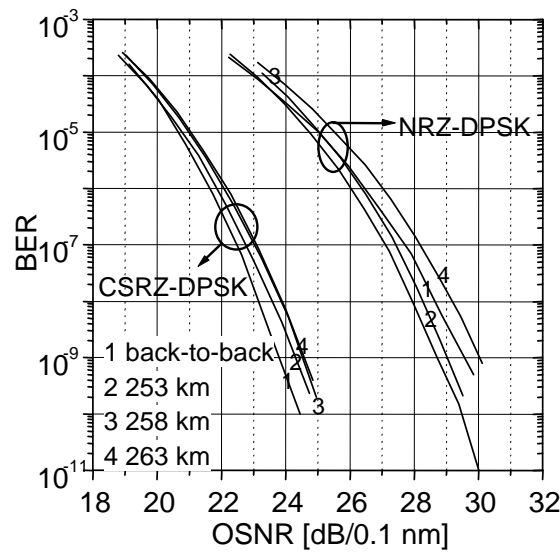


**Figure 2.33:** BER versus OSNR. The OSNR is varied by an attenuator.

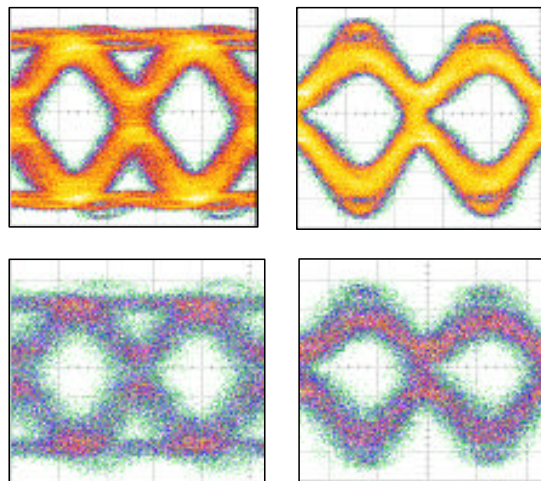


**Figure 2.34:** 40 Gbit/s eye diagrams back-to-back (top) and after 263 km transmission (bottom), for NRZ-DPSK and CSRZ-DPSK (from left to right)

Figure 2.33 shows BER vs. OSNR. With the 263 km fiber link, the Q factors are reduced to 19.1 and 20.4 dB, respectively, and they stay essentially unchanged when the tunable dispersion compensator is operational. One hour of error-free operation was verified in each case. In order to test other compensator CDs, either 5 km or 10 km of SSMF with a  $-342$  ps/nm piece of DCF was taken out from the link. Compensator control was always successful, and error-free transmission was always possible. Corresponding BER data (258 km, 253 km) is also plotted in Figure 2.33. The combined penalties of transmission and CD compensator were measured to be between  $-1.2$  dB (an improvement) and  $+1.2$  dB. Figure 2.34 shows received eye diagrams for for NRZ-DPSK and CSRZ-DPSK modulation formats.

## 2.5 Conclusion

The CD detection scheme is extremely cheap to implement, features superior sensitivity, is fast enough, introduces hardly any transmission penalty, tolerates NRZ and RZ ASK and DPSK modulation formats and may be many more modulation formats, provides also the sign of CD and is believed to have widest measurement range. The 40 Gbit/s CSRZ-DPSK system also features lock-in stabilized interferometer phase difference and a standard NRZ clock recovery.

In [72], CD has been compensated at 43 Gbit/s, but for CSRZ-ASK. When that CD compensator was operational, the Q factors were about 12.5 dB, which was very close to the FEC limit. Here, the residual chromatic dispersion has been compensated in a 263 km fiber link at 40 Gbit/s for the modulation formats NRZ-DPSK and CSRZ-DPSK. The synchronous arrival time detection scheme measured residual CD, which was in turn eliminated by automatic control of a  $-300$  ps/nm to  $-700$ ps/nm thermally tunable dispersion compensator. Q factors are  $> 19$  dB which corresponds to error free transmission. The total measured penalty of transmission and CD compensation was  $-1.2$  dB ...  $+1.2$  dB, for various link lengths and compensator CDs. CS(RZ)-DSPK outperforms the other modulation formats in receiver sensitivity, which recommends it for long and ultra-long haul optical transmission.

# Chapter 3

## oDQPSK Transmission System

With demands to increase capacity, increase reach and reduce cost, there has been growing interest in developing alternative modulation formats for high bit rate optical transmission systems [24–28]. A simple alternative to double the existing transmission capacity or spectral efficiency without optical bandwidth increase is to use *differential quadrature phase shift keying* (DQPSK) signals. Combined with RZ coding its robustness against XPM is also large because the intensity is not modulated by the data but is rather modulated by pulse carving. The theoretically possible receiver sensitivity for DQPSK signals is better than for intensity modulated signals. Practically, sensitivity of DQPSK receivers is almost the same as for the ASK receivers. For the given bit-rate, DQPSK has the symbol rate which is half of the bit-rate, resulting in increased tolerance to chromatic dispersion and polarization mode dispersion and reduced spectral and bandwidth requirements for the optical transmitter and receiver. It also known that DQPSK signal tolerates strong optical filtering [29]. In particular, DQPSK has recently received intense attention for several and obvious reasons. In this work, DQPSK is explored as an alternative optical modulation format that has multi-level phase modulation combined with direct detection. Later on, the DQPSK spectral efficiency was once more doubled using the polarization multiplexing technique.

### 3.1 Introduction to oDQPSK

Digital modulation formats are generally characterized by a so called constellation which is graphical representation of the real and imaginary part of the complex envelope of the modulated carrier. In optical communication, we have for the representation of the modulated carrier:

$$E(t) = \text{Re}[a(t)e^{j\phi(t)}e^{j\omega_c t}] \quad (3.1)$$

where  $a(t)e^{j\phi(t)}$  is the complex envelope which contains both, amplitude modulation  $a(t)$  and/or phase modulation  $e^{j\phi(t)}$ . Optical carrier frequency is determined by the laser center wavelength  $\omega_c$ . This complex envelope carries the information, allowing phase (or frequency) modulation as well as amplitude modulation.

In digital transmission, the  $b$  bit are transmitted with a bit rate of  $1/T_b$  bps, where  $T_b$  is the bit duration. In multilevel modulation schemes, the bits are collected and mapped to digital symbols which are chosen from an alphabet

$$d(i) \in \{d_0, d_1, \dots, d_{M-1}\}, M = 2^m \quad (3.2)$$

of  $M$  complex symbols at each symbol interval  $T_s = mT_b$  numbered by integer  $i$ . Thus, for 4-level PSK (DQPSK) transmission, we have  $m = 2$  and

$$d_0 = 1, d_1 = j, d_2 = -1, d_3 = -j. \quad (3.3)$$

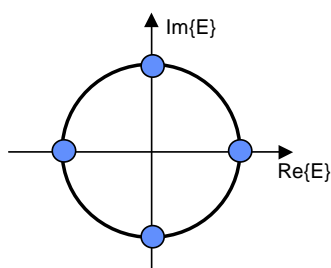


**Figure 3.1:** DQPSK Constellations

Figure 3.1 shows the DQPSK constellation. In DQPSK modulation format, the information is encoded in four different phase states  $0, \pi/2, \pi, 3\pi/2$  of the optical carrier. The carrier can assume one of four phases, each change of phase, or symbol, representing 2 bits. The bit combinations being 00, 01, 11 and 10. Consequently, the data stream can carry 2 bits at a time. Two bits are mapped onto one transmitted optical symbol, offering bandwidth reduction for increased spectral efficiency. The table 3.1 below illustrates the mapping from input symbol to output phase transition for DQPSK signal.

**Table 3.1:** Phase states for DQPSK signal

DataBits	PhaseChange
00	0
10	$\pi/2$
11	$\pi$
01	$3\pi/2$

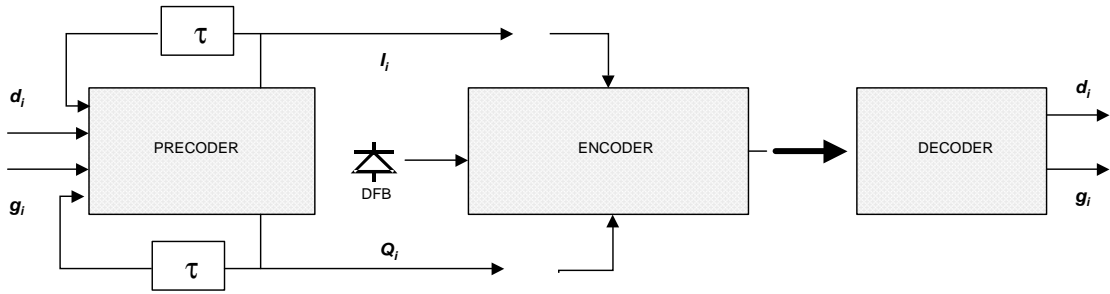
Recently number of experiments are reported using the DQPSK as the modulation format for high bit rate optical transmission systems having higher spectral efficiencies. Table 3.2 summarizes the selected DQPSK transmission experiments having higher spectral efficiencies and the corresponding transmission distances.

**Table 3.2:** Selected DQPSK transmission experiments with higher spectral efficiencies

Number of Channels	Channels Data Rate (Gb/s)	Distance (km)	Fiber Type	Efficiency (b/s/Hz)	Reference no.
40	160	124+200	SSMF+NZ-DSF	1.49	[73]
16	160	153+120	SSMF+NZ-DSF	1.49	[74]
8	160	170+60	SSMF+NZ-DSF	1.6	[75]
64	85.4	320	SSMF	1.6	[76]
50	85.4	300	NZ-DSF	1.14	[73]
8	40	200	SSMF	1.6	[27]
8	20	310	SSMF	0.8	[26]
9	25	1200	SMF-28	0.8	[25]

## 3.2 oDQPSK signal generation

To perform oDQPSK transmission, one requires a digital precoder, an optical encoder, and an optical decoder as shown in Figure 3.2.

**Figure 3.2:** Schematic representation of Optical DQPSK signalling

### 3.2.1 DQPSK Precoding

Because of the differential nature of decoding in oDQPSK transmission, a precoding function is required, as illustrated in Figure 3.2, to provide a direct mapping of the data from input to output. Mathematically, the operation of the precoder is described by the following set of equation [24]:

$$\begin{aligned}
 I_i &= (\overline{Q_{i-1} \oplus I_{i-1}})(\overline{d_i \oplus I_{i-1}}) + (Q_{i-1} \oplus I_{i-1})(\overline{g_i \oplus I_{i-1}}) \\
 Q_i &= (\overline{Q_{i-1} \oplus I_{i-1}})(\overline{g_i \oplus I_{i-1}}) + (Q_{i-1} \oplus I_{i-1})(\overline{d_i \oplus I_{i-1}})
 \end{aligned} \tag{3.4}$$

where  $\oplus$  denotes exclusive OR,  $d_i$  and  $g_i$  are the original information data bits, and  $I_i$  and  $Q_i$  are the precoded data bits.

With the precoding function given by (3.4), the output data streams from the decoder are identical to the data streams input to the precoder: oDQPSK provides optical 2:1 multiplexing and 1:2 demultiplexing at the optical level. In our lab oDQPSK transmission experiments as the  $2^7 - 1$  PRBS was transmitted, the precoding function was neither implemented not needed.

### 3.2.2 Optical Encoder

There are several possibilities to generate the optical DQPSK signals using the various types of devices. Most of them either uses two parallel Mach-Zehnder modulators (MZM) placed inside the another Mach-Zehnder interferometer forming a Mach-Zehnder superstructure having quadrature control electrodes to generate four phase states or uses a series combination of MZM and a phase modulator (PM) to generate four phase states of the oDQPSK signal. Another possibility is to use only PM driven in such a way that it again produces the four required phase states. Fourth possibility is to use single dual-drive modulator to produce nearly arbitrary phase and/or amplitude modulation onto the optical modulators. Next subsection gives the brief introduction to these methods and as well as the method that was used in the laboratory to generate the oDQPSK signal.

#### Parallel Structure using two Mach-Zehnder Modulators

The most widely used method to generate oDQPSK signal is shown in Figure 3.3 [24, 62]. The transmitter consists of two parallel Mach-Zehnder modulators (MZM). It requires two bias controls for each of the MZMs and an active phase control for the phase shifters. Each of the MZMs of Figure 3.3 is biased for minimum *DC* transmission and driven with NRZ data with peak-to-peak amplitude of  $2V_\pi$ . Quadrature phase control is required to recombine signals from the in-phase component (*I*) and the quadrature component (*Q*) with a relative phase difference of  $\pi/2$ . If the two normalized independent drive signals of such a transmitter are  $V_1$  and  $V_2$ , respectively, the baseband complex representation of the output of the transmitter is the complex number of the form

$$V_1 + V_2 e^{-j(\pi/2)}. \quad (3.5)$$

The output electric field is thus

$$\begin{aligned} E &= \text{Re}\{(V_1 - jV_2)e^{j\omega_c t}\} \\ &= V_1 \cos(\omega_c t) + V_2 \sin(\omega_c t) \end{aligned} \quad (3.6)$$

where *Re* denotes the real part of a complex number and  $\omega_c$  is the angular frequency of the optical carrier. Since the output signals of the two Mach-Zehnder modulators are combined with a  $\pi/2$  phase shift, no coherent superposition occurs in the output Y combiner. The half of the power is being radiated into the next higher order mode. The same splitting loss occurs also in the input Y fork [77]. Thus, a 3 dB intrinsic loss exists. The signal exiting the output of such transmitter is referred to as NRZ-DQPSK signal.

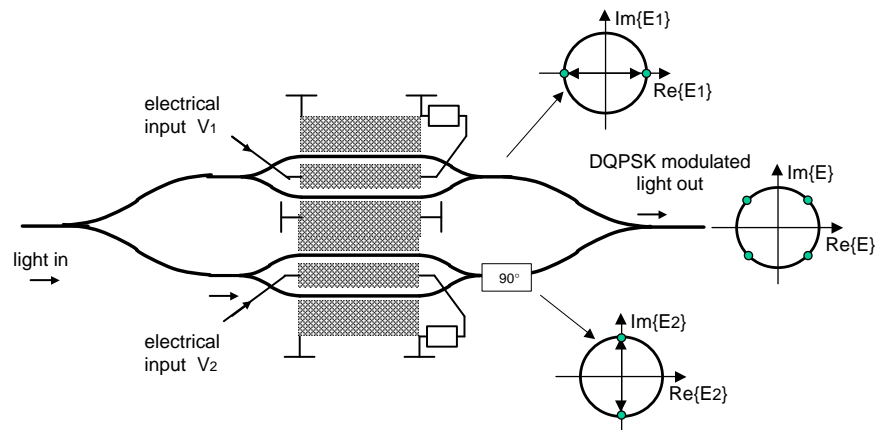


**Figure 3.3:** DQPSK signal generation using two Mach-Zehnder modulators

### Serial Structure Using Phase and Mach-Zehnder Modulator

A series arrangement of in-phase modulator and a MZM, as shown in Figure 3.4, is also possible, and has been used in experiments of [26, 28] to generate four phase states of DQPSK signal. Usually, the first in-phase modulator is driven by NRZ data stream and its modulation voltage is set to  $V_{\pi/2}$  to generate  $\pi/2$  phase shift. The second Mach Zehnder (MZM) modulator is driven by another NRZ data stream and also performs phase modulation. The modulation voltage of this second modulator is set to  $2V_\pi$  to generate  $\pi$  phase shift. There is no intrinsic loss. The relative amplitude error in the in-phase and quadrature parts of the normalized field in Mach Zehnder modulator can be neglected in comparison with the phase error in simple phase modulator. The signal that exits the second MZM is again equivalent to NRZ-DQPSK signal.

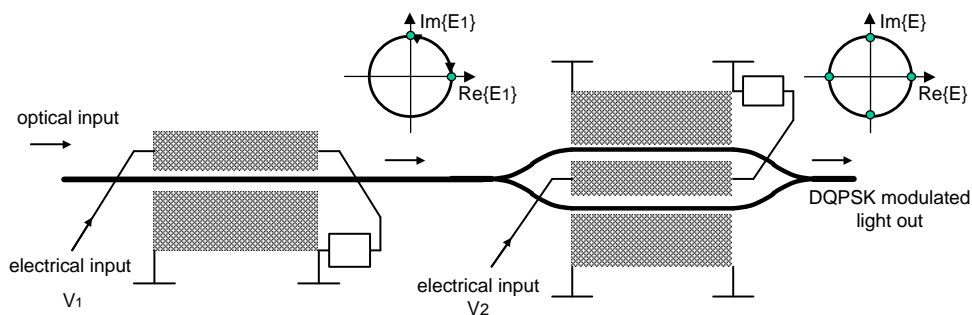


**Figure 3.4:** DQPSK signal generation using Mach-Zehnder and phase modulator

### Single Phase Modulator

A simple phase modulator shown in Figure 2.6 and explained in subsection of optical phase modulation in chapter 2 can also be used to generate the DQPSK signal. In this special case, peak-to-peak drive amplitude of one the NRZ data signal is set equal to twice the peak-to-peak drive amplitude of the another NRZ data signal. The sum of these two driving signals in fact drive the phase modulator. The phase modulator is biased such that it produces the optical output signal that takes one out of four phase states of DQPSK signal  $\phi_k \in \{0, \pi/2, \pi, 3\pi/2\}$  where input NRZ data streams ( $k = 1, 2$ ) are differentially precoded. There is no intrinsic loss.

### Single dual-drive modulator

A single dual-drive Mach-Zehnder modulator structure may also be used as device for producing nearly arbitrary phase and/or amplitude modulation onto an optical carrier.

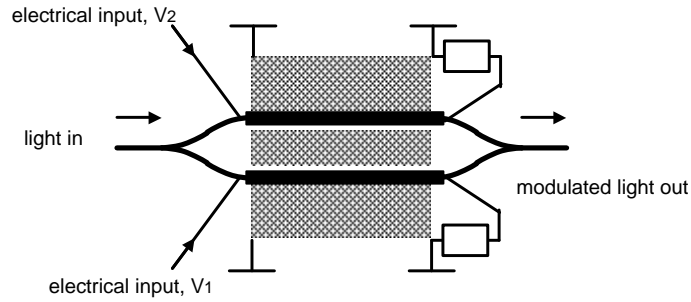


**Figure 3.5:** Single dual-drive MZM for DQPSK signal generation

This two arm structure usually results into the output complex envelope:

$$E_{\text{out}} = \frac{E_{\text{in}}}{2} \left[ \exp(j\pi \frac{V_1}{V_\pi}) + \exp(j\pi \frac{V_2}{V_\pi}) \right] \quad (3.7)$$

where  $V_\pi$  is the voltage to provide a  $\pi$  rad phase shift of each phase modulator. In the most trivial case, the MZM is operated as a phase modulator if  $V_1 = V_2$ . Thus, by a proper choice of the both driving voltages  $V_1$  and  $V_2$ , any quadrature signal can be generated and a variety of constellations can be achieved.

The equation (3.7) can be rewritten in the normalized form as

$$E_{\text{out}} = \frac{r_{\text{max}}}{2} (\exp(j\phi_1) - \exp(j\phi_2)) \quad (3.8)$$

where  $\phi_1 = \pi V_1/V_\pi$  and  $\phi_2 = \pi V_2/V_\pi + \pi$ . The output electric field,  $E_{\text{out}}$ , is the difference of the two vectors in the circle having a radius of  $r_{\text{max}}/2$ . The MZM shown in Figure 3.5 is biased at the point of minimum transmission and the maximum output electric field has

an amplitude  $r_{\max}$  when  $V_1 = V_2$  or  $\phi_1$  and  $\phi_2$  have antipodal phases. The equation (3.8) gives a geometric representation of the operation of a dual-drive MZM with two independent phase modulators. Assume an M-ary signal constellation that can be represented as complex numbers of the form

$$s_i = r_i e^{j\theta_i}, r_i > 0, 0 \leq \theta_i < 2\pi, i = 1, 2, \dots, M - 1 \quad (3.9)$$

with a maximum amplitude of

$$r_{\max} = \max\{r_0, r_1, \dots, r_{M-1}\}. \quad (3.10)$$

With two phases of [78]

$$\phi_{i1} = \theta_i + \cos^{-1}\left(\frac{r_i}{r_{\max}}\right) \quad (3.11)$$

$$\phi_{i2} = \theta_i - \cos^{-1}\left(\frac{r_i}{r_{\max}}\right) + \pi, \quad (3.12)$$

we obtained

$$s_i = \frac{r_{\max}}{2} (\exp(j\phi_{i1}) - \exp(j\phi_{i2})). \quad (3.13)$$

The procedure to find the two phases of  $\phi_{i1}$  and  $\phi_{i2}$  in the circle having radius of  $(1/2)r_{\max}$  for the constellation point of  $s_i$  is described in [78], where the real number of  $r_i$  is equal to the sum of two conjugated symmetrical complex numbers of  $(1/2)r_i \pm jy_i$  in the circle with a radius of  $(1/2)r_{\max}$ , i.e.  $(1/4)r_i^2 + y_i^2 = (1/4)r_{\max}^2$ . With  $\varphi_i = \cos^{-1}(r_i/r_{\max})$ , it is derived  $(1/2)r_i \pm jy_i = (1/2)r_{\max} \exp^{\pm j\varphi_i}$ . Figure 3.6 represents the two complex numbers of  $(1/2)r_{\max} \exp^{\pm j\varphi_i}$  as two vectors with phase angles of  $\pm\varphi_i$ . The real number of  $r_i$  given by

$$r_i = \frac{1}{2}r_{\max}e^{j\varphi_i} - \frac{1}{2}r_{\max}e^{j(\pi-\varphi_i)}. \quad (3.14)$$

All constellations points of (3.9) can be generated based on two phase modulators having the phases of (3.11) and (3.12), respectively. The dual-drive MZM in Figure 3.5 can be used to generate DQPSK signals with constellations of Figure 3.1 when operated as a phase modulator when  $\phi_{i1}$  and  $\phi_{i2}$  are antipodal phases. The four phases of Figure 3.1 are generated by a four-level drive signal. It is also possible to generate a DQPSK signal constellation with a smaller number of levels if the four constellation points are reached with two different two-level drive signals. The scheme that use two-level drive signals has intrinsic loss of 3 dB [77]. The peak-to-peak drive voltages of the two phase modulators in Figure 3.5 are proportional to the maximum phase difference of  $\phi_1$  or  $\phi_2$ , respectively. The maximum phase difference of the four level drive signals is  $3\pi/2$  and that of the two-level drive signals is  $\pi$  [78].

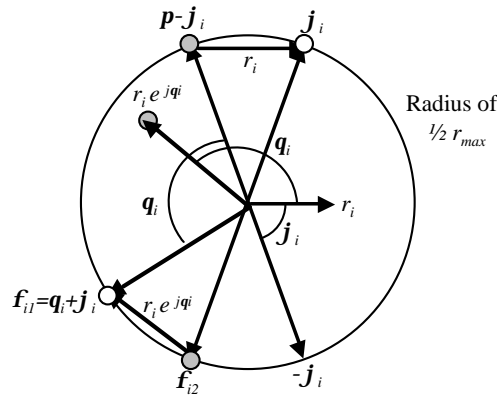


Figure 3.6: Procedure to find  $\varphi_{i1}$  and  $\varphi_{i2}$  for  $s_i = r_i e^{j\theta_i}$ .

### Serial Structure Using MZM and Interferometer

Figure 3.7 shows the laboratory implementation of the DQPSK transmitter using series combination of single dual-drive MZM followed by the low-cost all-fiber Mach-Zehnder interferometer (MZI) having differential delay of three symbol durations. This delay is high enough for decorrelating the data streams but avoids vibration and laser linewidth-induced differential phase fluctuations.

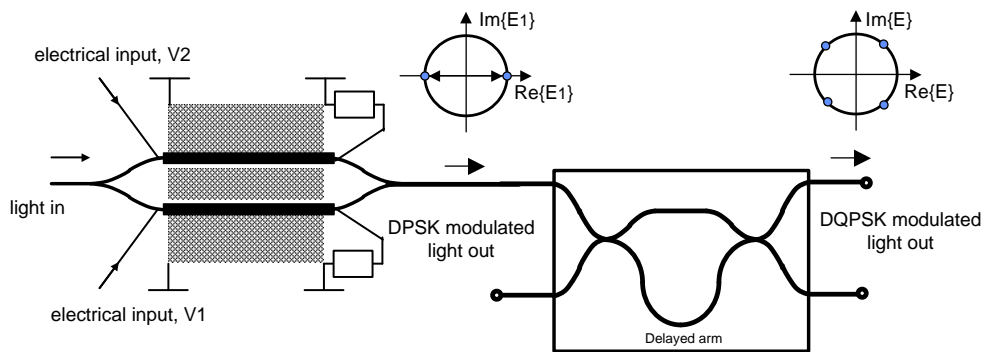


Figure 3.7: DQPSK signal generation using a dual-drive Mach-Zehnder modulator and interferometer

Mach-Zehnder interferometer with a  $\pi/2$  phase shift in one of the arms converts the NRZ-DPSK signal generated by the dual-drive modulator to NRZ-DQPSK signal. A piezo fiber stretcher is included in one of the arms for an active phase control. The measured polarization-dependent phase shift of MZI is  $< 500$  MHz and the extinction ratio is about 24 dB.

### 3.2.3 40 Gbaud DQPSK Transmitter

Figure 3.8 shows the RZ-DQPSK 40 Gbaud transmitter [30, 32].  $2 \times 40$  Gbit/s DQPSK signals are generated in a subsequent all-fiber temperature-stabilized Mach-Zehnder interferometer as described in the previous subsection. At one interferometer output, a 192.5 THz optical bandpass filter (BPF), a photoreceiver with a bandwidth of about  $\approx 12$  GHz, and a subsequent RF diode detector were used to measure the RF power carried by the optical signal. When the two optical signals are superimposed in phase quadrature, there is no interference and hence no RF power. A quadrature control loop based on a 10 kHz lock-in detection scheme stabilizes the interferometer phase by minimizing the RF power carried by the optical signal. The 10 kHz phase modulation has a depth of  $\sim 0.01$  rad (rms).

The laser frequencies are fine-tuned to points of a  $6.76 \text{ GHz} \approx 1/(2\tau)$  raster so that each WDM channel contains a proper DQPSK signal. The channel spacing is roughly an odd multiple of the raster point spacing. This means that each WDM channel has at least one neighbor whose in-phase and quadrature data streams are combined with opposite polarities and hence form a different optical pattern. After differential interferometric demodulation in the receiver, this means that the in-phase and quadrature data streams are exchanged.

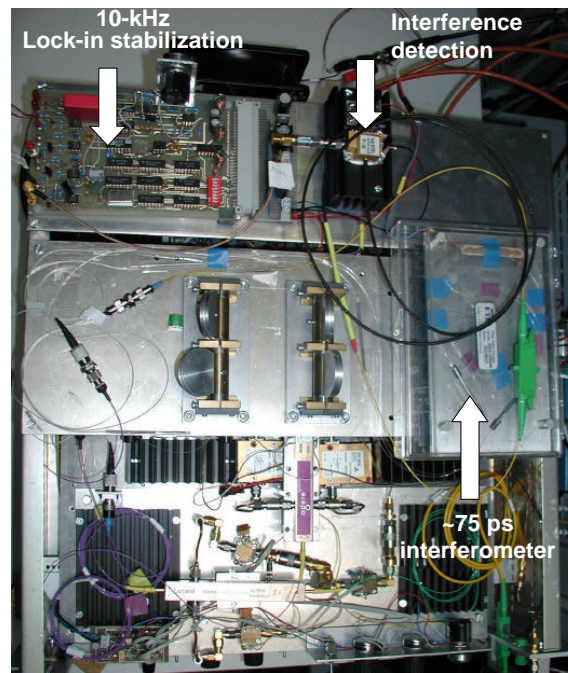


**Figure 3.8:**  $2 \times 40$  Gbit/s DQPSK Transmitter

In the transmitter, another dual-drive modulator driven at half the clock rate and biased at the transmission minimum carves 13 ps pulses and thereby generates the return-to-zero (RZ)-DQPSK signal for transmission. Figure 3.9 shows “eye diagrams” of the intensity of NRZ-DQPSK and RZ-DQPSK signals at the transmitter.

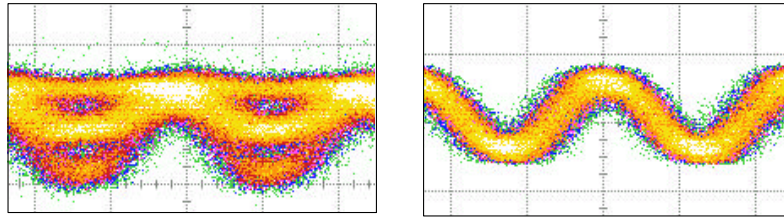


**Figure 3.9:** 40 Gbaud intensity eye diagrams of NRZ-DQPSK (left) and CS(RZ)DQPSK signals (right)

### 3.3 oDQPSK signal detection

Decoding function is normally performed in the optical domain using the Mach-Zehnder Delay Interferometer (MZDI). Delay interferometer used for DQPSK demodulation is very similar to the one that was used to demodulate DPSK signals.

#### 3.3.1 DQPSK Decoding

The decoder structure consist of a pair of Mach-Zehnder interferometers, each with an optical delay  $\tau$  equal to the symbol period  $T_s = 2T_b$ . The differential optical phase between the interferometer arms is set to  $\pi/4$  and  $-\pi/4$  for upper and lower branches, respectively (Figure 3.10).

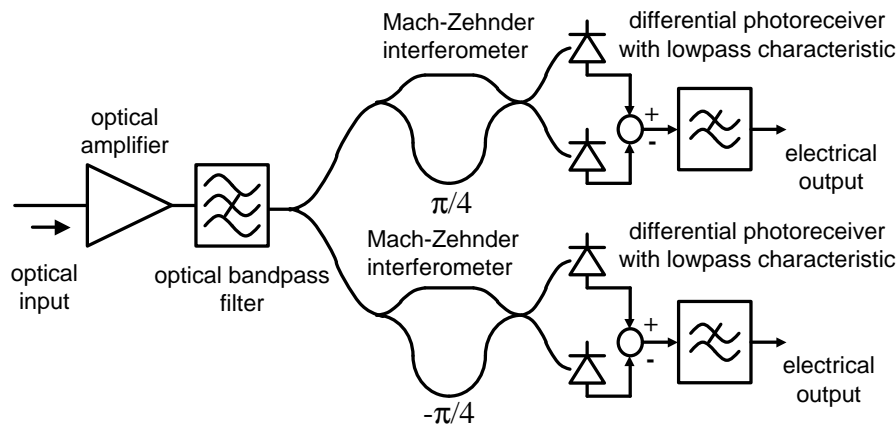


**Figure 3.10:** DQPSK Decoder

Balanced optical photoreceivers are employed in each of the interferometer; each of the photoreceiver pair used in the interferometer has a bandwidth  $> 50$  GHz. If the input signal has the form  $E_o e^{-j(\omega_0 t + \Delta\phi_i)}$ , then the output signals after balanced detection are proportional to:  $(\cos \Delta\phi_i + \sin \Delta\phi_i)$  and  $(\cos \Delta\phi_i - \sin \Delta\phi_i)$ , respectively. The output signals are, therefore, binary NRZ signals. Standard clock and data recovery circuits can therefore be used. Generally, an adaptive polarization control is not needed for demodulation of oDQPSK signals if the receiver interferometer is free from the polarization-dependent loss.

### 3.3.2 40 Gbaud DQPSK Receiver

The receiver employs optical preamplifiers, a flat-top C band DWDM DEMUX (Optun) and an integrated-optical Mach-Zehnder demodulator with a delay of 4 symbol durations (Figure 3.11). For proper reception of in-phase and quadrature data channels, the phase difference of delay demodulator is set to  $\pi/4$  or  $-\pi/4$  using differential micro-heaters with total constant power. The demodulator outputs are connected to two high-speed photodetectors (u2t), which are connected to differential inputs of a 1:16 Infineon demultiplexer that uses standard clock and data recovery circuits. Main advantage of this scheme is that here we do not need an extra high-speed photodiode to recover the clock from 40 GHz intensity modulation. A  $2^7 - 1$  PRBS data generated using the polynomial  $1 + X^6 + X^7$  was transmitted. Precoding function described by equation (3.4) was neither needed nor implemented as the PRBS pattern was transmitted. Therefore, there was a deterministic mapping of the data from the input to the output. As a result, the demodulated bit patterns in in-phase and quadrature data channels differ from the transmitted ones. To enable bit-error-rate (BER) measurements, the error detector was properly programmed to receive the expected data sequence using the DQPSK mapping.

## 3.4 $2 \times 40$ Gbit/s DQPSK Transmission Experiment

The aim of this transmission experiment is to demonstrate  $2 \times 40$  Gbit/s RZ-DQPSK transmission and compare its performance to that of the RZ-ASK and RZ-DPSK modulation formats in terms of receiver sensitivity and OSNR.

### 3.4.1 Transmission setup

Figure 3.10 shows the RZ-DQPSK 40 Gbaud transmission setup. For RZ-DPSK operation, the all-fiber Mach-Zehnder interferometer at the TX is left out. For RZ-ASK operation, both interferometers and one photodiode are left out.

The optical signal is transmitted over 3 fiber spans with a total length of 263 km. These three spans consist of 170 km of standard single mode fiber (SSMF), 60 km of nonzero dispersion shifted fiber (NZDSF), and 33 km of dispersion shifted fiber (DSF). Dispersion compensating fiber (DCF) with a total dispersion of  $-2713$  ps/nm was inserted between first and second stages of the two inline EDFAs. A thermally tunable dispersion compensator from TeraXion compensates for the residual dispersion of the 192.5 THz channel. Dispersion was set to  $-470$  ps/nm while the total tuning range of the dispersion compensator is from  $-300$  to  $-700$  ps/nm.

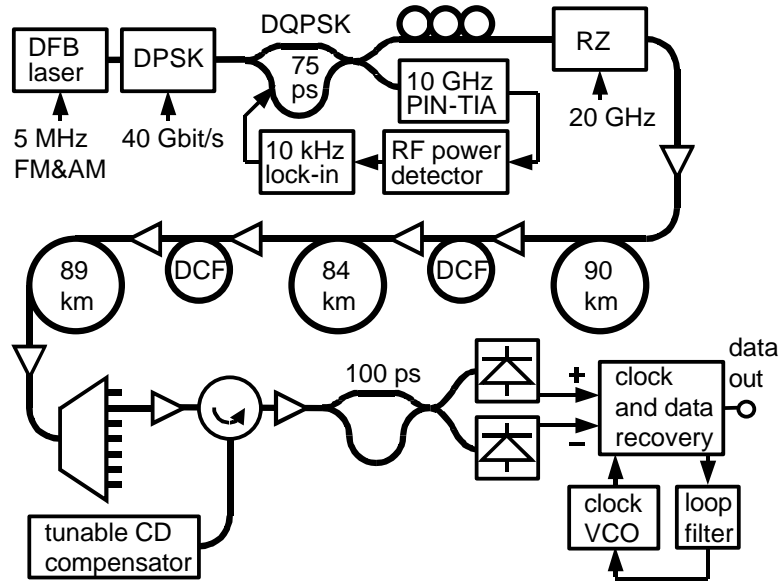


Figure 3.11:  $2 \times 40$  Gbit/s RZ-DQPSK transmission setup

### 3.4.2 Measurement Results and Discussion

Figure 3.12 shows measured bit-error-ratios (BERs) vs. optical preamplifier input power in dBm for RZ-DQPSK, RZ-ASK, and RZ-DPSK modulation formats. The back-to-back Q factors for these modulation formats are 20.9 dB (for both I and Q data channels), 26.6 dB, and 29.5 dB, respectively. The corresponding back-to-back receiver sensitivities are  $-27.5$  dBm (for both I and Q data channels),  $-27.3$  dBm, and  $-33.6$  dBm. They are equivalent to OSNRs of 29.7, 27.7, and 23.8 dB/0.1nm, respectively. With the 263 km fiber link in place, the Q factors are reduced to 17.5 dB (for I and Q data channels), 19.6, and 20.4 dB, respectively.

As can be seen from Figure 3.12, the DQPSK receiver sensitivity is almost the same as for ASK. However, DQPSK transports 80 Gbit/s whereas ASK transports only 40 Gbit/s. In principle, the similar bit rates can be also achieved, for example, by using the multilevel modulation formats based on amplitude shift keying (ASK) [79, 80]. This class of signals is known as M-ary ASK signals.

The transmission bandwidth of a multilevel ASK signal (M-ary signal), where  $M$  is the number of levels in the  $M$ -ary signal, is scaled by a factor  $1/\log_2(M)$  compared to a binary signal operating at the same bit rate. Similarly, the symbol period is increased by a factor  $\log_2(M)$  compared to a binary signal. The back-to-back sensitivity, however, is significantly degraded for these type of signals because of the increased number of levels in signals and the signal dependence of signal-spontaneous beat noise [81].

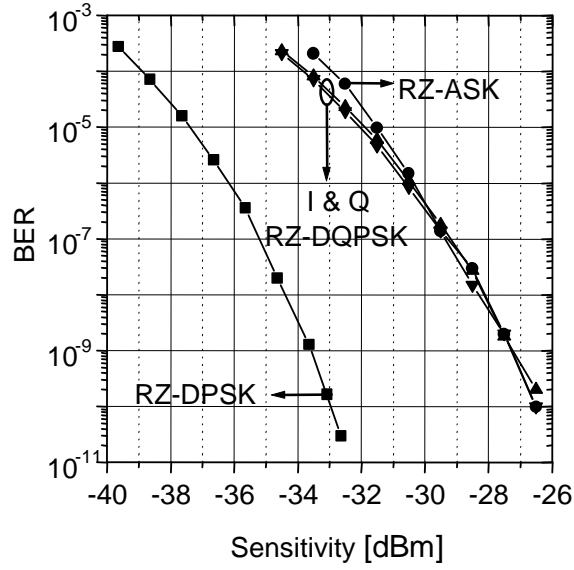


**Figure 3.12:** Measured BERs vs. optical preamplifier input power for RZ-DPSK, RZ-DQPSK, RZ-ASK

In a presence of stationary noise only, and assuming a white noise spectral density, the additional optical power required for detecting an  $M$ -ary signal over a binary signal signal is [81]

$$P_M = \frac{M - 1}{\sqrt{\log_2(M)}}. \quad (3.15)$$

According to equation (3.15), a 4-ary ASK requires about 3.3 dB more optical power than a conventional binary signal.

The measured receiver sensitivity (Figure 3.12) is still better for RZ-DPSK signals, but the main advantage is that RZ-DQPSK signal simply doubles the transmission capacity. When the sensitivities are compared on the basis of photons/bit (not photons/symbol) then DQPSK is 3.2 dB better than ASK, and 3.1 dB worse than DPSK. All 2.5 Gbit/s sub-channels are bit error free, with the almost identical sensitivities.

Figure 3.13 shows  $2 \times 40$  Gbit/s RZ-DQPSK eye diagrams back-to-back (top) and after 263 km transmission (middle) for in-phase and quadrature reception. The bottom eye diagram with 3 lines results when the interferometer phase difference was set to either  $0^\circ$  or  $90^\circ$  instead of  $45^\circ$  or  $135^\circ$  for DQPSK reception. The eye diagrams are well open, both back-to-back and after transmission over 263 km of fiber. The in-phase and quadrature data channels were tested (in 1 out of 16 2.5 Gbit/s sub-channel) to be error-free during 1 h each, but these measurements were interrupted (before errors occurred) for occasional phase adjustment in the receiver interferometer, and polarization adjustment. Shorter transmission spans were also tried, 258 km (5 km less SSMF) and 253 km (10 km less SSMF but increased link dispersion because a  $-342$  ps/nm DCF module was also taken out).

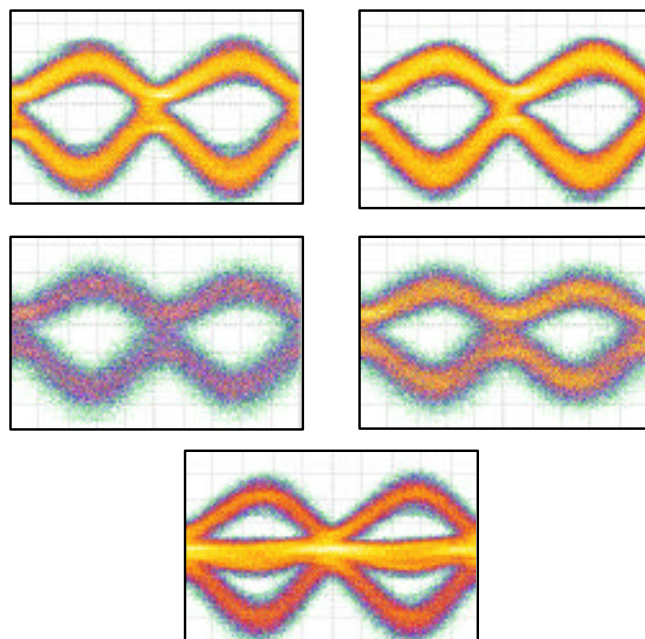


**Figure 3.13:**  $2 \times 40$  Gbit/s RZ-DQPSK I and Q eye diagrams back-to-back (top) and after 263 km of fiber (middle). Bottom diagram is back-to-back with wrong interferometer phase

Error-free transmission was possible, though not extensively tested. The chromatic dispersion compensator had to be set to  $-390$  ps/nm (for 258 km) and  $-635$  ps/nm (for 253 km), respectively. In those cases as well as for 263 km (see Figure 3.13) the eye diagrams before and after transmission had identical shapes, which suggests that the compensator did not introduce a significant penalty. This is remarkable because DQPSK is more sensitive to chromatic dispersion than DPSK or ASK. However, as the signal is transmitted, the in-phase part of optical amplifier noise modulates the pulse amplitudes. Self phase modulation converts this into a random phase modulation which limits permissible link lengths. This nonlinear phase noise is also discussed in [82, 83]. Although, this is not strictly necessary because linear phase noise is generally included as a part of any sensitivity calculation in which optical amplifier noise is taken into account. It scales with the square of the length and linearly with the symbol rate (taking into account that the linewidth tolerance scales also linearly with the symbol rate). Launch powers were 4...6 dBm for the 3 spans in the present experiment, and the laser linewidth is  $< 2$  MHz according to the Triquint data sheet.

The setup could be made less sensitive against phase noise if the interferometer delay in the receiver were shortened to 1 bit. In theory, this should at least double the permissible transmission distance but we don't know precise experimental limits yet. Definitely, the use of Forward Error Correction (FEC) technology, in practice, will relax the problem.

### 3.5 RZ-DQPSK Polarization Multiplex Transmission

DQPSK [24–26, 28, 31, 32] and polarization division multiplex (PolDM) [33] transmission each can double the fiber capacity by their increased spectral efficiency. Both techniques have been combined to transmit  $4 \times 10$  Gbit/s per WDM channel [27, 62].

In this work, a 160 Gbit/s ( $4 \times 40$  Gbit/s) transmission system is realized by combining DQPSK with polarization division multiplex, for the first time at a line rate of 40 Gbaud. The fiber capacity equals 1.6 bit/s/Hz, which value has previously been achieved or surpassed only at 10 Gbaud [27, 62].

#### 3.5.1 Transmission Setup

Figure 3.14 shows the RZ-DQPSK polarization division multiplex (PolDM)  $4 \times 40$  Gbit/s per WDM channel transmission setup [75]. Eight 100-GHz spaced WDM signals (192.3 ... 193.0 THz) are combined with equal polarizations and are modulated together.

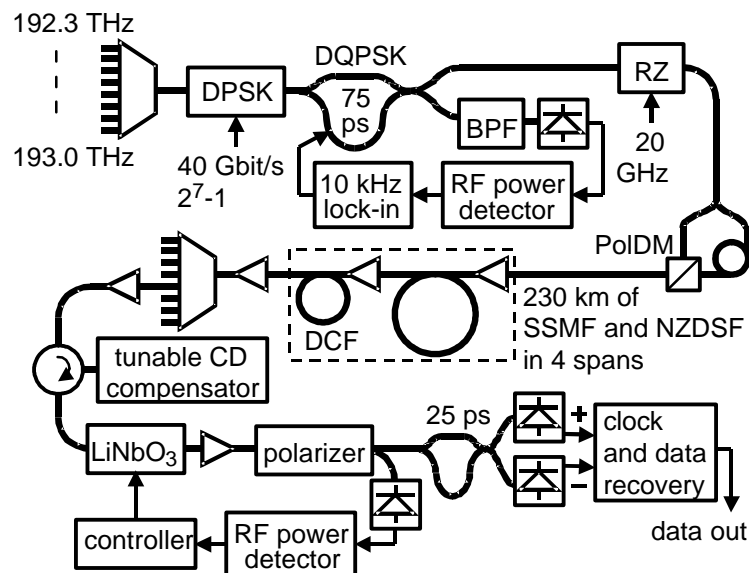


**Figure 3.14:**  $4 \times 40$  Gbit/s per channel RZ-DQPSK PolDM transmission

First,  $2 \times 40$  Gbit/s DQPSK signals are generated (Section 3.4). In order to increase the bit rate from 80 to 160 Gbit/s per WDM channel, an existing polarization division multiplexer (PolDM) was employed. PolDM is a quaternary modulation scheme where one bit modulates the horizontal and the other bit modulates the vertical electric field [33]. It doubles the data rate in existing trunk lines without need for an additional optical bandwidth. Thus, the DQPSK signal is split and recombined with orthogonal polarizations with a differential delay of 2.8 ns. Since this polarization multiplexer (PolDM) was available, interleaving of orthogonally polarized pulses in the time domain was not tested.

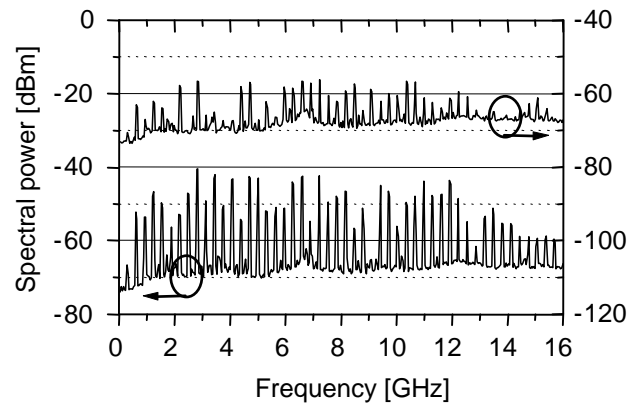
The optical signals are transmitted over  $\sim 230$  km of fiber in 4 fiber spans having  $\sim 170$  km of SSMF and  $\sim 60$  km of NZDSF. DCF with dispersions of  $-1345$ ,  $-685$ , and  $-683$  ps/nm is inserted in between two inline EDFAs, in pairs, respectively ( $-2713$  ps/nm in total). Fiber and DCF launch powers are  $-0.5 \dots + 4$  dBm and  $-4.8 \dots - 3$  dBm per WDM channel, respectively. EDFA input powers are  $-15 \dots - 10.5$  dBm per WDM channel.

The receiver contains optical preamplifiers and a flat top C band DWDM DEMUX. To receive the 192.5 THz (1557.366 nm) channel, the TeraXion thermally tunable dispersion compensator is set to  $-440$  ps/nm. Group delay vs. wavelength for various dispersion settings has been already shown in Section 2.4 (Figure 2.31). Other WDM channels are not compensated because only a single channel TDC [69] was available. Automatic polarization control is implemented in the receiver to recover both polarizations. A LiNbO<sub>3</sub>-based polarization controller is followed by a polarizer. The control strategy is again based on the minimization of the broadband RF interference noise. It occurs when both polarizations are present after the polarizer. A linear ideal polarizer is an optical device, birefringent or not, that only transmits one linear state of polarization and suppresses any transmission of the orthogonal state of polarization. Although a real component always lets through a fraction of the orthogonal state. These device is characterized by a Jones matrix  $\mathbf{J}_P$  which is expressed with respect to a reference coordinate system  $Oxy$ . If the phase factor, which simply renders the propagation of the light in the material medium making up the device, is not taken into account, the Jones matrices  $\mathbf{J}_{P_x}$  and  $\mathbf{J}_{P_y}$  of the polarizers whose principal axes are respectively the axes  $Ox$  and  $Oy$  are given by:

$$\mathbf{J}_{P_x} = \begin{pmatrix} 1 & 0 \\ 0 & 0 \end{pmatrix} \quad \mathbf{J}_{P_y} = \begin{pmatrix} 0 & 0 \\ 0 & 1 \end{pmatrix} \quad (3.16)$$

Polarizer is used to suppress the orthogonal polarization and to ensure that phase modulated light having a single polarization enters the Mach-Zehnder delay interferometer for demodulation. The interference noise is detected in another 12 GHz photoreceiver followed by an RF power detector (Figure 3.15). The measured RF power is  $-22$  dBm in the best case (when the two polarizations are well aligned) and  $-8.5$  dBm in the worst case (when both polarizations pass the polarizer with equal powers). The controller tries to minimize the interference noise by suppressing the unwanted polarization in the fiber polarizer. Signal acquisition takes around 1 s, and this is fast enough to track occurring fiber polarization changes.

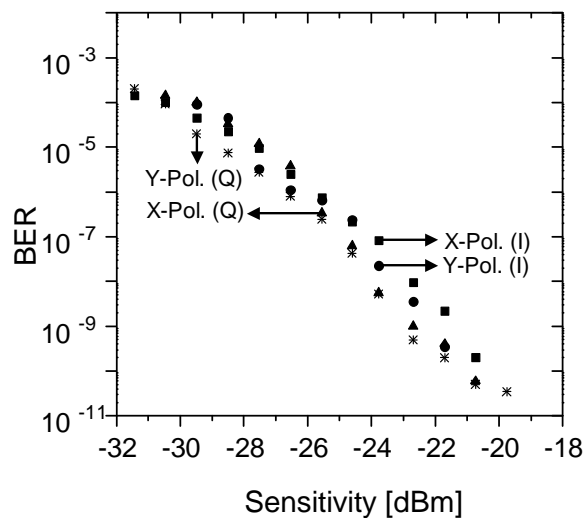
Another Mach-Zehnder interferometer, with a delay of one symbol duration, demodulates the signal. For proper reception of in-phase and quadrature data channels, the phase difference of the delay demodulator is set either to  $45^\circ$  or  $135^\circ$ , using a piezo fiber stretcher. The demodulator outputs are connected to two high-speed photodetectors, which in turn are connected to the differential inputs of a 1:16 demultiplexer with standard clock and data recovery. Note that the demodulated bit patterns in in-phase and quadrature data channels differ from the transmitted ones. The half rate clock signals in transmitter and receiver are generated by VCOs from WORK Microwave GmbH.



**Figure 3.15:** Electrical interference spectra measured in the 12 GHz photoreceiver after the polarizer

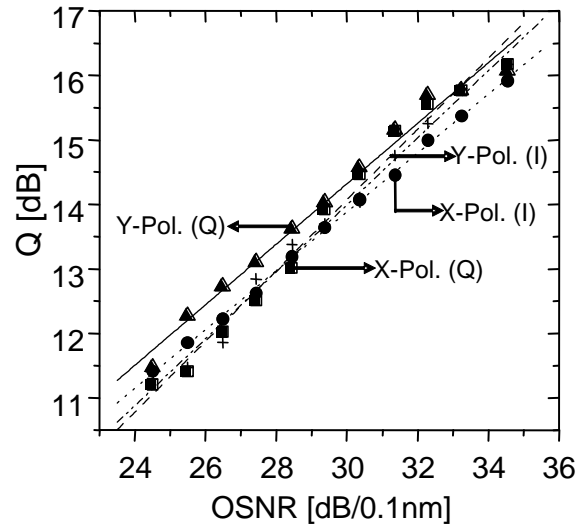
### 3.5.2 Transmission Results

Figure 3.16 shows the recorded back-to-back sensitivities of the  $4 \times 40$  Gbit/s, 192.5 THz signal, for which the TDC was operational. For a BER of  $10^{-9}$  the sensitivity is about  $-22$  dBm. At the forward error correction (FEC) threshold, say for a BER of  $10^{-3}$ , it is about  $-32$  dBm.



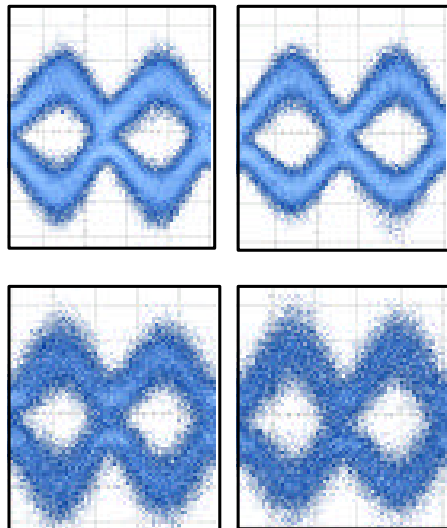
**Figure 3.16:** Back-to-back receiver sensitivity for both in-phase and quadrature data channels for one polarization. Optical power is given for aggregate 160 Gbit/s signal

Figure 3.17 shows measured back-to-back Q factors, calculated from BER measurements, for I and Q data streams for all 8 WDM channels. A  $Q \geq 15.6$  dB or  $BER \leq 10^{-9}$  is achieved for all channels, polarizations and quadratures. After transmission over 230 km of fiber, a  $BER \leq 10^{-9}$  is obtained for the 192.5 THz channel with CD compensation. Corresponding data, expressed as Q factors, is also given in Figure 3.17.



**Figure 3.17:** Back-to-back performance of  $4 \times 40$  Gbit/s system

The eye diagrams corresponding to back-to-back configuration and after transmission over 230 km of fiber are shown in Figure 3.18. The case of other polarization is very similar. The eye diagrams before and after transmission have identical shapes, which indicates a clean transmission with effective CD compensation. This is remarkable because an extrapolation of the results in [27], and our own experience, tells that DQPSK tolerates less chromatic dispersion than DPSK at the same symbol rate.



**Figure 3.18:** Eye diagrams in one polarization, (top) back-to-back in I channel, Q channel and (bottom) after 230 km in I and Q channel

In Figure 3.19 the optical spectrum after 229 km of fiber is shown. Figure 3.20 shows Q factors, directly calculated from the measured BER values, for the back-to-back case against the OSNR. The OSNR is determined in an 0.1 nm bandwidth by comparing the spectral peak against the surrounding noise. To reach  $Q = 15.6$  dB the required OSNR is about 33 dB. At the FEC threshold the required OSNR is about 22 dB.

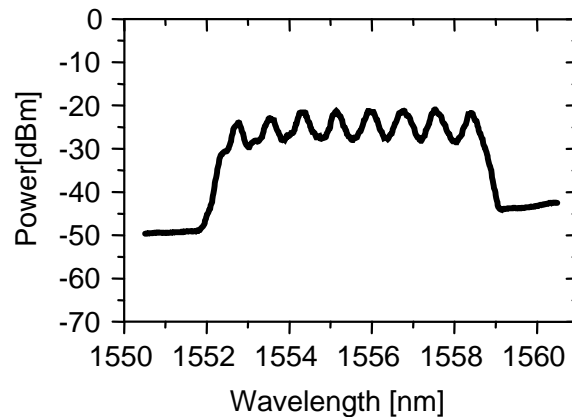


**Figure 3.19:** Optical spectrum after 229 km of fiber

The presence of the other WDM channels confirms that the capacity is 1.6 bit/s/Hz. Simultaneous BER measurement of all WDM channels would require a broadband dispersion compensator [25]. If FEC is available, amplifier spacing and/or WDM channel number are expected to be expandable.

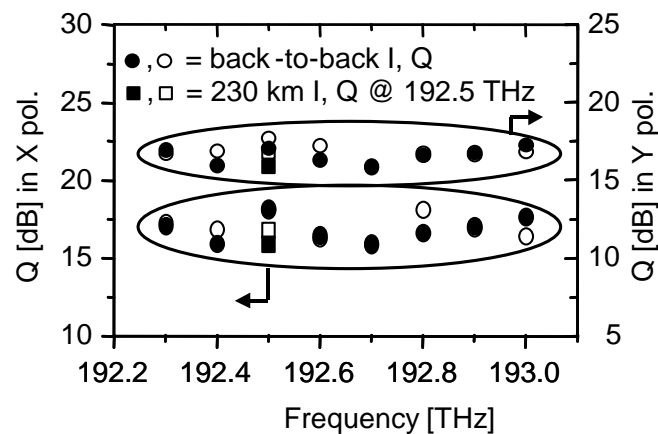


**Figure 3.20:** Measured Q factors for I and Q data channels in both polarizations back-to-back for 8 WDM channels, and after transmission over 230 km fiber for the CD-compensated 192.5 THz channel

System stability was limited to  $\sim 1$  min due to insufficient thermal isolation of the receiver interferometer. Recently, the receiver interferometer has been packaged with the

commercial styrofoam, which has drastically improved the system stability. However, long term stability has not yet been assessed.

By using only 100 GHz channel spacing, a 1.6 bit/s/Hz spectral efficiency is achieved. In [28], a 70 GHz spacing was used for  $2 \times 42.7$  Gbit/s DQPSK transmission. Combining such a channel spacing with polarization division multiplex should make spectral efficiencies beyond 2 bit/s/Hz possible.

## 3.6 Conclusion

The  $2 \times 40$  Gbit/s RZ-DQPSK error-free signals are transmitted over a 263 km fiber link. A 40 Gbit/s tunable chromatic dispersion compensator and a standard 40 Gbit/s DWDM DEMUX are used; fiber capacity is simply doubled. The receiver sensitivity is -27.5 dBm. The back-to-back Q factor is  $> 20$  dB. Even after transmission the Q factor is 17.5 dB.  $2 \times 40$  Gbit/s RZ-DQPSK transmission over a 263 km fiber link was reported. Sufficient resilience against nonlinear phase noise and band limitation in a 40Gbit/s WDM DEMUX is achieved by a Q factor of 17.5 dB. The receiver sensitivity of -27.5 dBm is 0.2 dB better than for RZ-ASK and 6.1 dB worse than for RZ-DPSK but the data rate is twice as high.

For the first time, a 160 Gbit/s ( $4 \times 40$  Gbit/s) DQPSK on each of 8 100 GHz-spaced WDM channels using a 40 Gbit/s tunable chromatic dispersion compensator and a standard 40 Gbit/s DWDM DEMUX has been demonstrated. Data is carried in two polarizations and differentially encoded in two quadratures. Fiber capacity per WDM channel is therefore quadrupled. A 1.6 bit/s/Hz transmission over 230 km of fiber is achieved with  $Q > 15.6$  dB for one of the 8 WDM channels for which the tunable dispersion compensator was operational.

## Chapter 4

# High-Speed Integrated Circuits for oDPSK Transmission

High-performance low-cost physical layer integrated circuits are needed for the successful implementation of next generation 40 Gbit/s optical networks. To expand the transmission capacity of the existing wavelength division multiplexed (WDM) networks, such high bit rates must have to be realized at the single channel level. This prerequisite imposes significant technological demands on the optical front ends. To date, the high-speed (i.e. 10 and 40 Gbit/s) demonstrations in the literature mainly focuses on the transmitter hardware [36–40, 84, 85] as opposed to receiver hardware. In this work, a differential amplifier combined with Travelling Wave Amplifier concept is simulated in GaAs technology while differential in and differential out linear amplifier is demonstrated in 0.18  $\mu\text{m}$  CMOS technology using striplines.

### 4.1 Differential Amplifier for 10 and 40 Gbit/s CS(RZ)-DPSK system

To build the commercial (CS)RZ-DPSK receiver, the architecture of the conventional NRZ optical receiver must be changed. It has been shown both theoretically and experimentally that roughly a 3 dB improvement in system margin can be achieved by using a balanced optical front end (OFE) instead of a single-ended OFE (see Figure 4.1). Therefore, for high-speed systems using CS(RZ)-DPSK or DQPSK, particularly at 10 and 40 Gbit/s, the design of an integrated balanced optical front end (OFE) can be extremely challenging due to packaging issues and integrated circuit performance which basically includes differential in and differential out linear amplifier with two matched photodiodes, and is thus quite worthy of significant attention. Such optical front ends are needed to reach record sensitivity limit of about  $-35.5$  dBm or less and optical signal-to-noise ratio (OSNR) performance of or around 18.5 dB in a 0.1 nm bandwidth at a BER of  $10^{-9}$ . Such a sensitivity or OSNR performance is very difficult to achieve without using the linear differential amplifier.

Differential processing of input RF signals removes some waveshape distortions resulting from RF group delay variations and amplitude distortions. Typically, the common mode rejection ratio (CMRR) should be better than 20 dB [86]. The methodology that is outlined here could provide a commercial path without the use of monolithic integrated circuits. Such an approach usually takes an advantage of the hybrid technologies that allows us to use better photodiodes and differential amplifier performance because of the individually optimized fabrication processes.

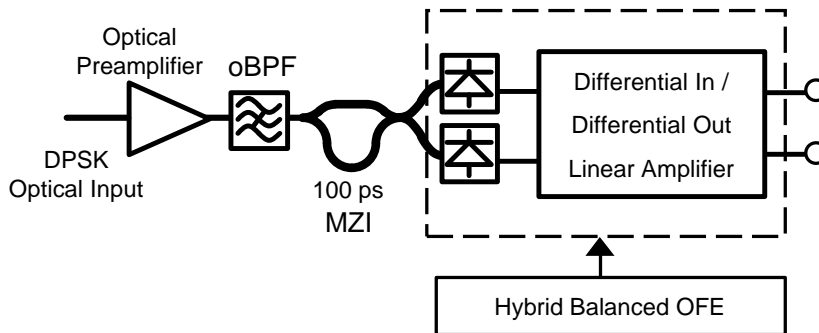


**Figure 4.1:** Typical 40 Gbit/s CS(RZ)-DPSK balanced optical front end

Figure 4.1 shows the typical schematic of the CS(RZ)-DPSK balanced optical front end. Received input optical signal (DPSK) is first passed through the optical preamplifier followed by the optical bandpass filter (oBPF) to improve the OSNR and then through the delay demodulator (Mach-Zehnder interferometer) to generate two complementary ASK signals for direct detection. It is desirable to differentially amplify these directly detected signals before they are passed on to the standard clock and data recovery circuits in order to achieve better signal-to-noise ratio performance. The linear differential amplifier could be used for this purpose.

Typically, such differential in and differential out linear amplifier should have a small signal gain of around 20 dB, a 3 dB bandwidth of at least 36 GHz, and a nominal maximum output swing of 400 mV per channel for 40 Gbit/s application [86]. The circuit should be DC coupled at the input and output and therefore, must have separate input offset voltage terminals to set the desired output DC offsets for the data and data complement outputs. Such circuits at 40 Gbit/s could be realized either in GaAs or InP or in SiGe technology [86]. CMOS technology could become an alternative for 10 Gbit/s applications and beyond [45, 87–89].

## 4.2 Differential Distributed Amplifier

The differential distributed amplifier presented here is based on the OMMIC D01PH pseudo-morphic AlGaAs/InGaAs HEMT technology which was specifically developed for power

applications and operational frequencies up to the millimeter wave region [90]. Typically, D01PH process exhibits the cut-off frequency in the range of  $\sim 100$  GHz.

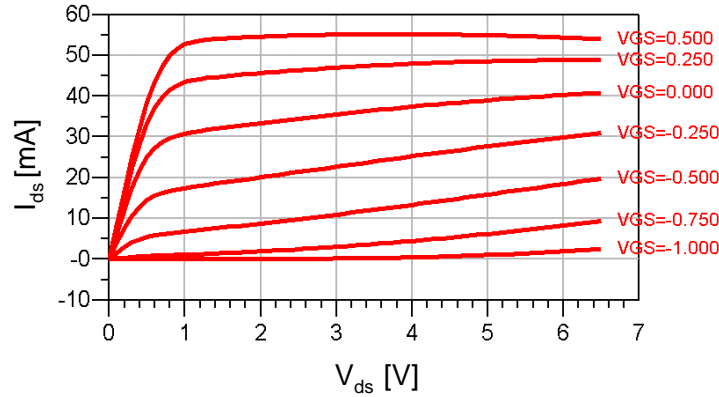


**Figure 4.2:** Simulated DC characteristics of the HEMT fabricated in OMMIC D01PH process

Figure 4.2 shows the simulated HEMT (size:  $2 \times 40 \mu\text{m}$ ) characteristics of drain-to-source current,  $I_{DS}$ , versus drain-to-source voltage,  $V_{DS}$ , for different values of gate-to-source voltage,  $V_{GS}$ . It is possible to operate the HEMT with zero gate-to-source voltage. The HEMT's in distributed amplifying stages are operated with zero gate-to-source voltage while in the differential amplifying stages they are biased.

### 4.2.1 Distributed Amplification

The concept of distributed amplifiers dates back to the 1940s when it was used for the first time in the design of broadband vacuum tube amplifiers. With recent advances in microwave integrated circuit and device processing technology, the distributed amplifiers found new applications in broadband microwave amplifiers [91]. Bandwidth in excess of decade are possible with good input and output impedance matching. But, they are generally larger in size than amplifiers having a comparable gain over a narrower bandwidth. Distributed amplifiers are also known as travelling wave amplifiers (TWA).

Most distributed amplifiers since the early 1980's have been realized as MMIC's on compound semiconductor technology (GaAs or InP) [38–42]. Recently, interest in MOS-FET distributed amplifiers [92–96], has been fueled by the fact that a standard submicron CMOS process can reach operating speeds well into the microwave range [97]. However, there is still a considerable obstacle in the realization of useful CMOS distributed amplifiers due to the difficulty in realizing high-quality factor inductors and transmission lines in a standard CMOS process [93].

The basic configuration of a distributed amplifier is shown in Figure 4.3. The amplifier consist of two transmission lines on the input and the output, and multiple transistors providing gain through multiple signal paths. The forward (from left to right in Figure 4.3) wave on the input line is amplified by each transistor. The incident wave on the output line travels forward in synchrony with the travelling wave on the input line.

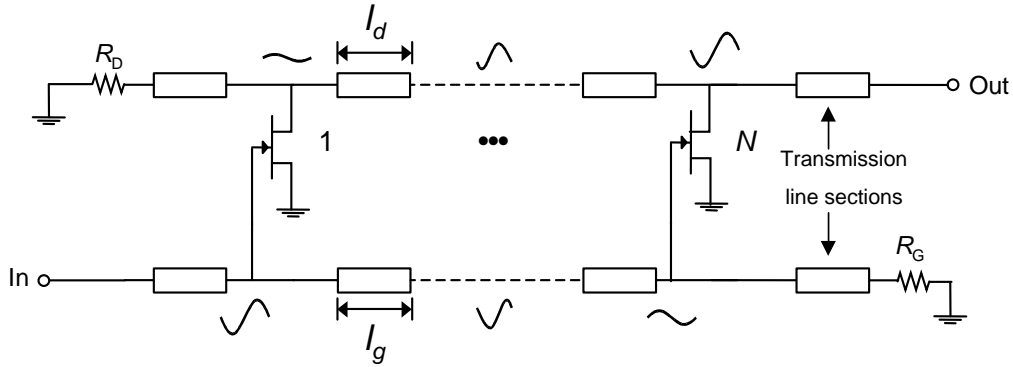


Figure 4.3: Basic configuration of the travelling wave amplifier

Each transistor adds power in phase to the signal at each tap point on the output line and therefore, the whole amplifier is capable of providing a higher gain-bandwidth product than a conventional amplifier. The forward travelling wave on the gate line and backward (travelling from right to the left) wave on the drain line are absorbed by terminations matched to the loaded characteristic impedance of the input line,  $R_G$ , and output line,  $R_D$ , respectively, to avoid reflections. The extended bandwidth of the distributed amplifier comes at the price of a larger time delay between its input and output, as there is a trade-off between the bandwidth and delay in an amplifier. Alternatively, one can think of this approach as a method of absorbing the parasitic capacitances of the transistors into transmission line structures and making them a part of the passive network [91, 98]. According to the inductive–capacitive (LC) model of the transmission line as derived in Appendix B, this added capacitance portions reduce the impedance of the gate and drain line to

$$\begin{aligned} Z_{0G} &\approx \sqrt{\frac{L'_g}{C'_g + C_{gs}/l_g}} \\ Z_{0D} &\approx \sqrt{\frac{L'_d}{C'_d + C_o/l_d}} \end{aligned} \quad (4.1)$$

As has been mentioned above, the resulting waves on the drain line travel in forward direction in synchrony with the travelling wave on the gate line. Matched terminations absorb the forward wave on the gate line and backward wave on the drain line. Thus, the phase velocities

$$v_{\text{ph}} = \frac{1}{\sqrt{L'C'}} \quad (4.2)$$

on the gate and drain line must coincide. As the input capacitance is normally larger than the output capacitance, a constructive superposition, for example, can be achieved by using the different transmission line lengths for the gate and drain line. Another possibility is to insert the appropriate capacitance either in parallel with the drain line or in series with the gate line.

The total TWA gain resulting from  $N$  transistors stages as has been derived in Appendix B is given by the following expression:

$$G_p = \frac{g_{ko}^2 Z_{0G} Z_{0D} [\exp(-\alpha_G N l_g) - \exp(-\alpha_D N l_d)]^2}{4(\alpha_D l_d - \alpha_G l_g)^2}. \quad (4.3)$$

Reducing the number of stages will obviously reduce the gain [99]. The simple solution is to increase the size of the individual transistor in order to effectively increase the transconductance,  $g_m$ , of the individual transistor. However, an increase in the size of transistor also increases the gate capacitance and hence decreases the cut-off frequency

$$f_c = \frac{1}{\pi Z_{0G} C_{gs}}. \quad (4.4)$$

The number of stages which maximizes the gain of a traveling wave amplifier at a given frequency can be approximated by [99]

$$N_{opt} = \frac{\ln(\alpha_G l_g / \alpha_D l_d)}{\alpha_G l_g - \alpha_D l_d}. \quad (4.5)$$

As a result, the gain of a distributed amplifier cannot become infinity. The overall gain of the travelling wave amplifier increases with corresponding increase in the distributed stages until the optimum number of stages has been reached at the given frequency. Any further increase in the distributed stages beyond the optimum number is not useful because the signal can not overcome the attenuation in the extra sections of the drain line. As a result, the gain of the travelling wave amplifier begins to decrease with further increase in the number of distributed stages.

### Cascode Stage

Traveling wave amplifiers normally use the cascode as the main amplifying stage. Figure 4.4 is an example of a *cascode amplifier*, a common-source transistor driving a common-gate transistor. A cascode amplifier has the same overall voltage gain as that of the common-source amplifier. The main advantage of a cascode amplifier is its lower input Miller capacitance, which is considerably less than the input capacitance of a common-source amplifier. Compound device also provides a higher output impedance and reduced “reverse internal feedback”. But the main drawback of the cascode stage is that it exacerbates the stability problems caused by resonance in the  $S_{22}$  parameter of the amplifier.

### 4.2.2 Circuit Design

The differential distributed Amplifier (DDA) basically consists of a differential preamplifier circuit with two differential outputs, each driving the gate line of a TWA with four stages [35].

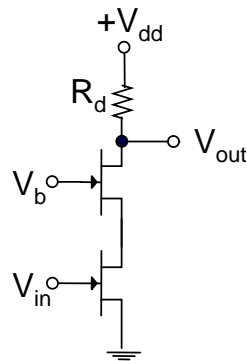


Figure 4.4: Typical schematic of the cascode amplifier

### Differential Pre-amplifier Circuit

Figure 4.5 (left) shows the schematic of the lumped differential preamplifier which acts as an input stage of the differential distributed amplifier. Differential pre-amplifiers features on-chip  $50\ \Omega$  resistors to provide good impedance matching. The differential input signals are coupled into the differential preamplifier using the  $50\ \Omega$  matched coplanar waveguides. The width of the central conductor and the gap between the central conductor and the ground planes of the coplanar waveguides are  $13\ \mu\text{m}$  and  $18.5\ \mu\text{m}$ , respectively. Differential preamplifier has simulated power gain of  $\approx 3\ \text{dB}$  at 40 GHz while the simulated Common Mode Rejection Ratio (CMRR) is better than 16.5 dB up to 40 GHz as shown in Figure 4.5 (right).

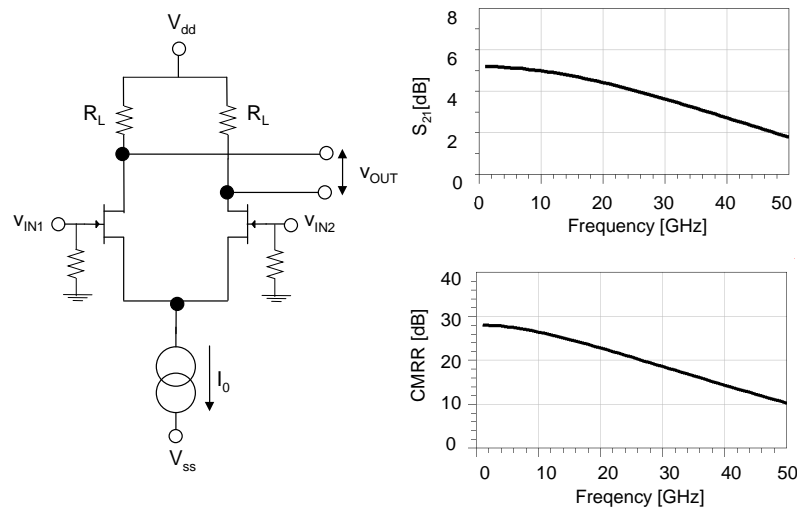
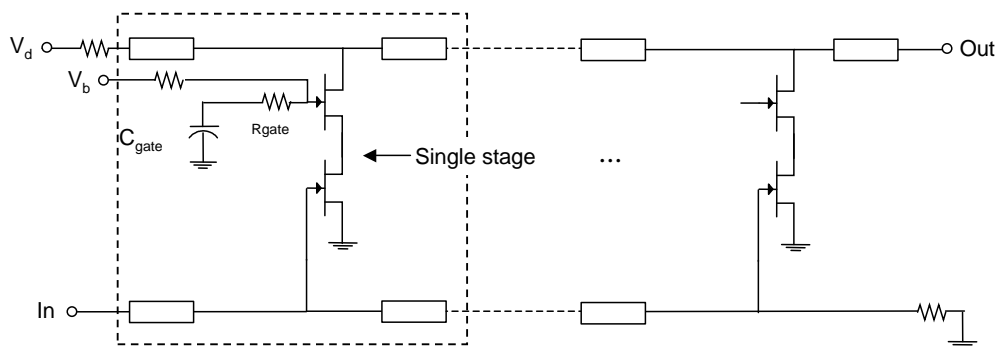


Figure 4.5: Schematic of the differential pre-amplifier (left) and simulated magnitude of  $S_{21}$  and CMRR (right)

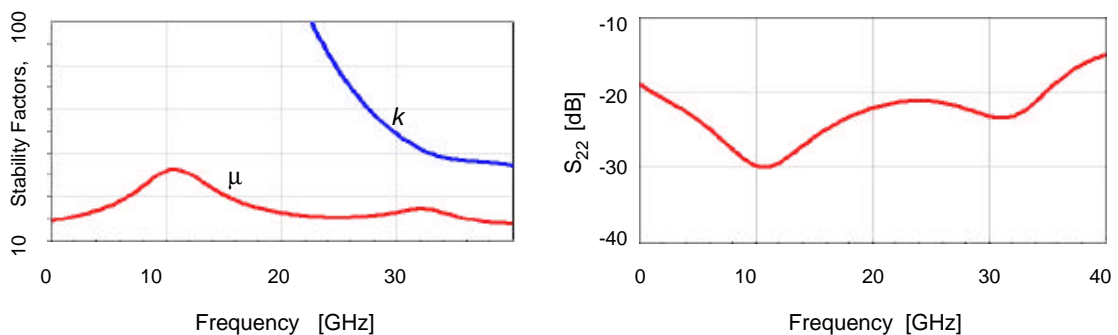
### Travelling Wave Amplifier

Figure 4.6 shows the schematic of the traveling wave amplifier. The circuit is designed to work with the drain bias voltage of 2.8 V which could be applied through an external bias tee. This voltage is also used on chip for the drain line termination resistor, avoiding the DC losses that would result from termination to ground. To obtain larger bandwidth, a common-source common-gate (cascode) amplifier is used as the main amplifying stage. Thus, a single cascode stage consists of a pair of two finger HEMTs in a common-source common-gate cascode configuration where every finger has a gate width of  $40 \mu\text{m}$ . Cascode is designed as a single cell in order to save space and reduce parasitics. The gate bias voltage of common-gate HEMT is set to 1.4 V.



**Figure 4.6:** Schematic of a traveling wave amplifier using cascode as the main amplifying stage

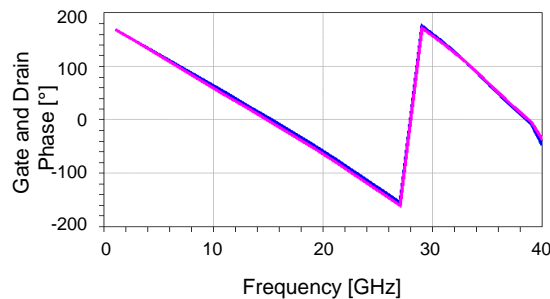
The main drawback of the cascode cell is that it causes the resonance in  $S_{22}$  of the amplifier, which may lead to stability problems. Therefore, in order to improve stability, a series-damping resistor at the gate of the common-gate transistor is inserted. Simulation results confirm that the amplifier is unconditionally stable which is indicated by the both stability factors ( $k$  and  $\mu$ )  $> 1$ . Figure 4.7 shows both the stability factors (left) and the output reflection coefficient,  $S_{22}$ , (right) which is below -15 dB up to 40 GHz.



**Figure 4.7:** Stability factors  $k$  and  $\mu$  (left) and output reflection coefficient  $S_{22}$  (right)

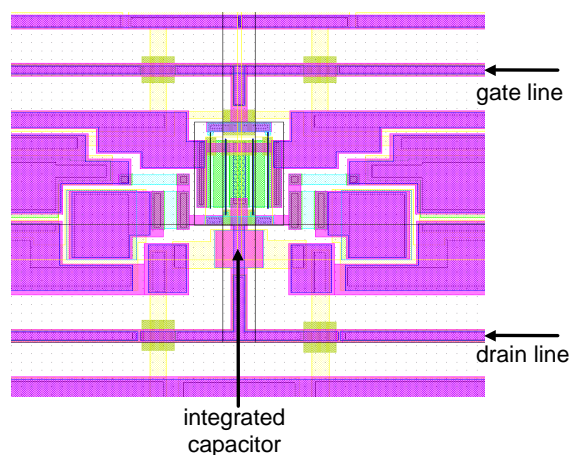
The characteristic impedance of the coplanar waveguides used in the schematic of traveling wave amplifiers is  $65 \Omega$ . The central conductor width and gap between the central conductor and the ground planes is  $8 \mu\text{m}$  and  $21 \mu\text{m}$ , respectively. Top metal is used as a conductor metal.

Simulated drain and gate line lengths for optimum gain with respect to the desired bandwidth are  $200 \mu\text{m}$  and  $150 \mu\text{m}$ , respectively. Such longer lengths are permissible using the meander lines in the layout option, however they complicate the layout and simply consume more area. As an alternative to longer drain line, a small capacitor of the order of  $0.03 \text{ pF}$  was used to slow down the signal. Thus, the gate and drain phase are matched as evident from the simulation shown in Figure 4.8. Figure 4.9 shows how the capacitor is integrated in the T-junction of the drain line.

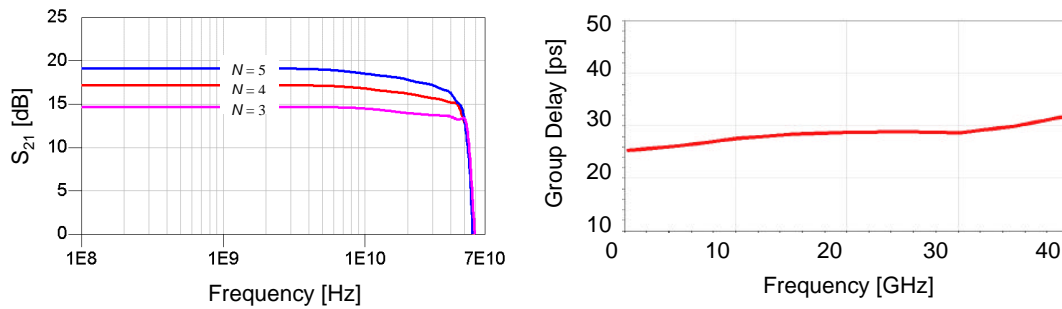


**Figure 4.8:** Phases on the gate and drain line

All resistors in the schematic which are used in simulation use a thin film N+ active layer with a typical sheet resistance of  $100 \Omega/\text{square}$ . DC voltages are decoupled on the chip using the decoupling capacitors having a  $150 \text{ nm}$  SiN dielectric layer.

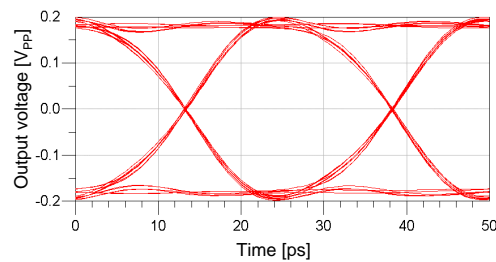


**Figure 4.9:** Layout details of the cascode cell



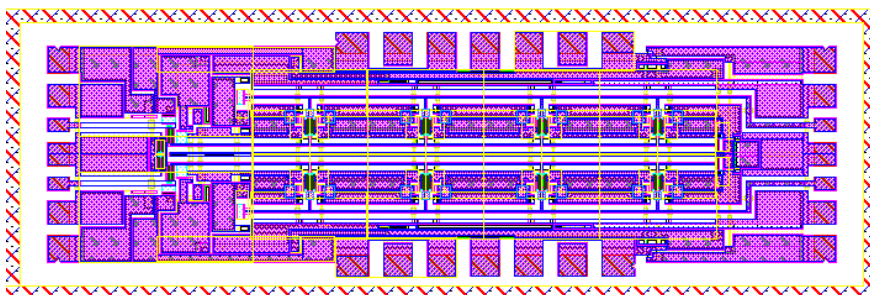
**Figure 4.10:** Optimization of forward transmission as a function of number of stages  $N$  (left) and group delay (right)

Figure 4.10 (left) shows the optimization of forward transmission ( $S_{21}$ ) versus the stage numbers (for  $N = 3 \dots 5$ ). For  $N = 4$ , a forward transmission gain of 17.2 dB with a 46.8 GHz bandwidth is simulated. The gain at 40 GHz is  $\sim 15$  dB. Characteristic response (gain versus frequency) is very flat. The simulated group delay has a very slight rising trend with respect to the increase in frequency. The simulated group delay difference in the frequency range up to 40 GHz is less than 10 ps as depicted in Figure 4.10 (right).



**Figure 4.11:** Simulated eye diagram for 50 mV<sub>pp</sub> input voltage

Figure 4.11 shows the simulated eye diagram having the output voltage of around 0.37 V<sub>pp</sub> for the input voltage of 50 mV<sub>pp</sub>. The simulated gain of the differential amplifier for 40 Gbit/s PRBS signals is higher than 17 dB.



**Figure 4.12:** Layout of the differential distributed amplifier at 40 Gbit/s

Figure 4.12 shows the layout of the differential distributed amplifier which has the dimensions of  $3\text{ mm} \times 1\text{ mm}$ . It is realized to fulfill important high-frequency circuit design goal- a total layout symmetry. The input and output data lines are in GSGSG configuration with a  $100\text{ }\mu\text{m}$  pitch.

### 4.2.3 Result Discussion

This section presents the state of the art technique to implement the high-gain differential amplifiers at 40 Gbit/s. Simulation results indicate that the differential distributed amplifier has a maximal simulated gain of 17.2 dB in a 3 dB frequency bandwidth of 46.8 GHz and a CMRR of  $\sim 16.5\text{ dB}$  at 40 GHz.

Results are comparable with the optical front-end circuit used by Sinsky et al [86]. Their linear differential amplifier was built using a high-performance SiGe process and uses a traveling wave design. They have achieved 21 dB of small signal gain in a 3 dB frequency bandwidth of 36 GHz with the CMRR of 20 dB at 40 GHz. Using this circuit they reported the record sensitivity of  $-35.9\text{ dBm}$  (39 photons/bit) for a BER of  $10^{-9}$  and an OSNR of 17 dB in 0.1 nm bandwidth for the reception of RZ-DPSK signals [86].

## 4.3 10 Gbit/s CMOS Differential Amplifier

Traditionally, high-speed circuits are realized either in GaAs or in InP technology. Recently, the SiGe technology became an alternative to both. However, the above mentioned technologies have relatively high cost of integration. An approach that will drastically reduce the cost is the standard CMOS technology. Another advantage of using the CMOS technology is that it has a high packaging density and relatively low power dissipation. On the other hand, it is relatively slow. It is indeed difficult to implement passive structures because of high propagation loss due to the low bulk-resistivity of CMOS substrates [100].

In this work, a single-stage differential pre-amplifier, followed by three pairs of distributed common source stages using striplines, is implemented in standard  $0.18\text{ }\mu\text{m}$  CMOS technology. Although, striplines (SL's) are lossy as compared to microstrips (MS's) or coplanar waveguides (CPW's), SL has a certain advantage over both of them when used in complex analogue circuits for system integration due to the perfect shielding. Additionally, the striplines are completely surrounded by the dielectric material. As a result, they are free from dispersive effects.

Two most popular technologies used for designing analogue integrated circuits are bipolar and MOS. Continuous improvement of analogue MOS capabilities forced the designers to explore the world of CMOS technology. CMOS stands for the complementary MOS and this technology makes use of both p-channel and n-channel MOSFETs.

In standard  $0.18\text{ }\mu\text{m}$  CMOS technology, the epitaxial substrate has low bulk resistivity of the order of  $10^{-2}\Omega\cdot\text{cm}$ .  $0.18\text{ }\mu\text{m}$  process provides a single polysilicon layer and six metal layers. Metal layers are fabricated using aluminium and numbered from M1 to M6. Top layers M5 and M6 have a thickness of  $0.92\text{ }\mu\text{m}$  while lower layers have typical thickness

of  $0.5 \mu\text{m}$ , respectively. The metal layers in CMOS are separated by the internal dielectric material having dielectric constant  $\epsilon_r \approx 4.3$ . For substrate and p-well isolation, the deep n-well isolation (NISO) technology is available.

Both n- and p-channel MOSFETs are fabricated as surface devices. The gates are fabricated with n- or p-type polysilicon layer and topped with a metal silicide for lower gate series resistance. Figure 4.13 shows the cross-section of  $0.18 \mu\text{m}$  CMOS transistors and transconductance characteristics of n-channel MOSFET as a function of the gate-source voltage.

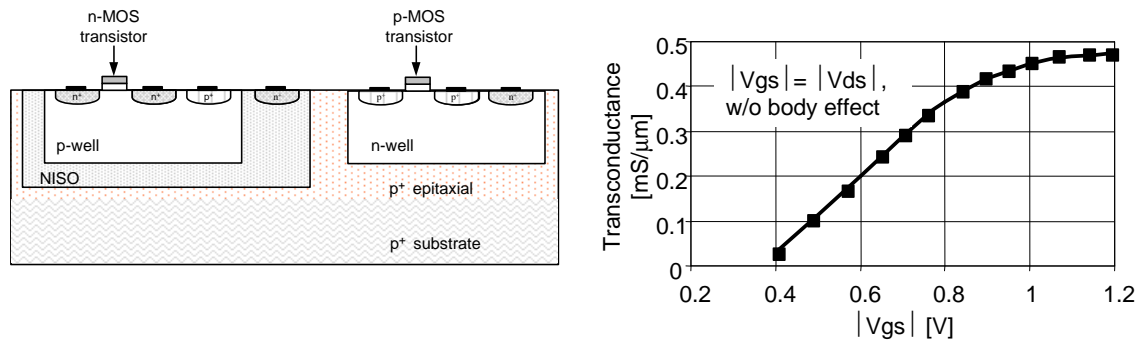


**Figure 4.13:** Cross-section of the  $0.18 \mu\text{m}$  CMOS process (left) and n-MOS transconductance as a function of the gate-source voltage (right)

### 4.3.1 Design of Transmission Line Structures

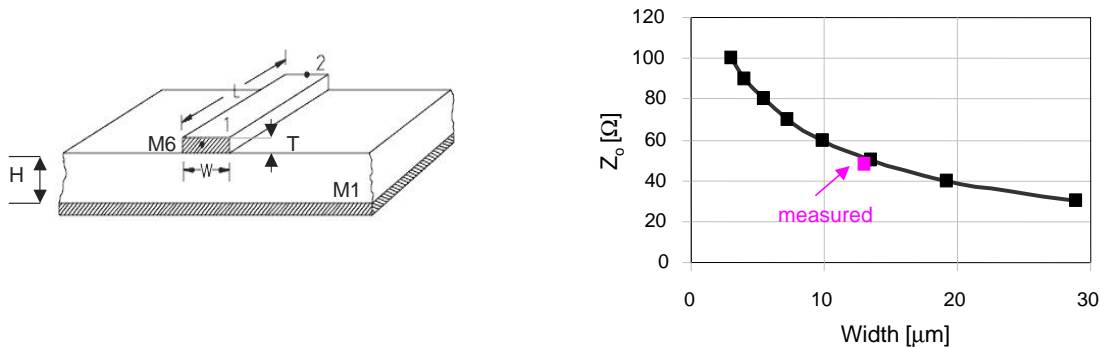
Recent advances in high-speed circuits have highlighted the interest in monolithic transmission lines – as both parasitic components and useful devices. With operating frequencies increasing to several tens of GigaHertz and/or the chip dimensions approaching several millimeters, the transmission lines can degrade the performance of analogue and digital circuits. Therefore, accurate modelling of transmission lines is thus necessary in the design and analysis of high-speed circuits. In circuit design, several characteristic properties of transmission lines become critical: characteristic impedance, loss, wave velocity, and field confinement [101].

Three main types of transmission line structures that can be used in CMOS design are the Microstrip lines (MS), Coplanar Waveguides (CPW), and Striplines (SL). The next subsection presents the simulation results on microstriplines, coplanar waveguides and striplines using the Momentum Electromagnetic Field Simulator and LineCalc in ADS.  $50 \Omega$  lines are fabricated in  $0.18 \mu\text{m}$  CMOS process. The transmission line models are extracted from measured S parameter data. Later on, these models are used to design the differential amplifier using striplines in  $0.18 \mu\text{m}$  CMOS technology.

### Microstrip Line

Figure 4.14 (left) shows a geometry of the microstripline in CMOS process. As the thickness of the dielectric layer depends on the CMOS process, the characteristic impedance of microstriplines is controlled by the width ( $W$ ) of the conductor ribbon fabricated in top metal M6 which is deposited on the internal CMOS dielectric with ground metallization in bottom metal M1 to prevent any interaction with lossy substrate. The layers are chosen such that capacitance per unit length is minimized, while the width of signal conductor is maximized. Thus, the smallest possible attenuation is obtained.

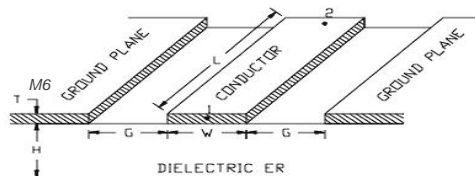
Varying the conductor width from  $29 \mu\text{m}$  to  $3 \mu\text{m}$ , changes the characteristic impedance of the microstripline in a range of  $30\text{-}100 \Omega$  as shown in Figure 4.14 (right). A  $50 \Omega$  microstripline line is fabricated using  $13 \mu\text{m}$  width.



**Figure 4.14:** Geometry of the microstripline in CMOS (left) and its characteristic impedance as function of the conductor width (right)

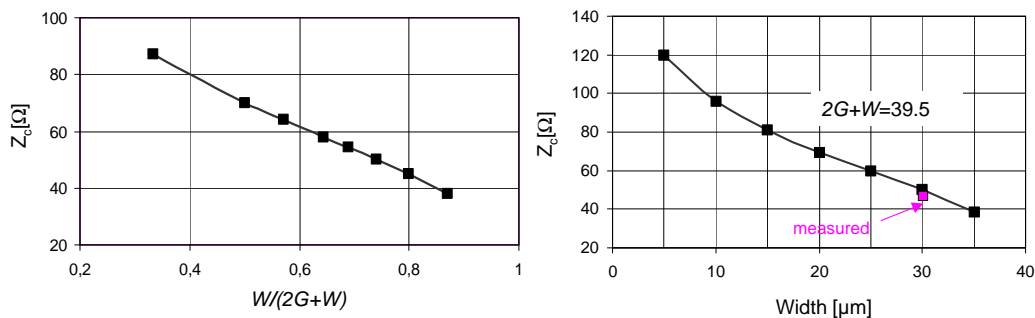
### Coplanar Waveguide

Figure 4.16 shows the geometry of the coplanar waveguides using the top metallization layer M6 in CMOS. The characteristic impedance of coplanar waveguide is controlled by the width ( $W$ ) of the central conductor and the gap ( $G$ ) between the central conductor and ground planes.



**Figure 4.15:** Geometry of coplanar waveguide

Simulated variation of the characteristic impedance for coplanar waveguide as a function of aspect ratio  $W/(2G + W)$  is given in Figure 4.16 (left). The characteristic impedance of the CPW is in the range of 40 – 120  $\Omega$  while keeping the  $W + 2G = 39.5 \mu\text{m}$  constant, as shown in Figure 4.16 (right). Two slots with the same width  $G=4.75 \mu\text{m}$ , separated by a  $30 \mu\text{m}$  metallic ribbon give  $50 \Omega$  waveguide, obtained for minimum total loss in a frequency range up to 10 GHz. Due to the stronger electromagnetic coupling to the lossy substrate coplanar waveguide exhibits higher loss at higher frequency than microstrip line. Figure 4.17 shows the measured attenuation results in dB/mm from the test structures. Wider signal line is more lossy at higher frequency due to the higher substrate loss, indicated by the large width ( $W$ ) of the signal line and the large gap  $G$ .



**Figure 4.16:** Characteristic impedance of the coplanar waveguide in function of the ratio  $W/(W + 2G)$  (left) and conductor width (right)

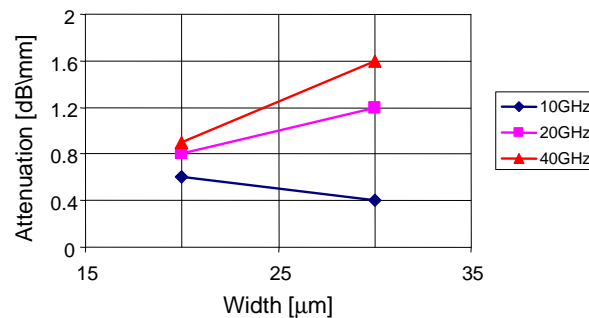


**Figure 4.17:** Measured attenuation for  $50 \Omega$  CPW versus width of signal line

### Stripline

Figure 4.18 (left) shows the geometry of the stripline (SL) which is placed in the metal M4 of the CMOS process. Normally, the metal M4 is sandwiched between the two parallel metal planes, bottom metal (M1) and top metal (M6). Striplines are typically realized using narrow width due to the fact that the two ground planes which are in the close vicinity of the stripline introduces the large parasitic capacitance.  $3.5 \mu\text{m}$  wide stripline brings the characteristic impedance close to  $50 \Omega$ . Changing the conductor width from  $12 - 2 \mu\text{m}$ , changes the characteristic impedance of the stripline in a range of  $20 - 60 \Omega$  as shown in Figure 4.18 (right).

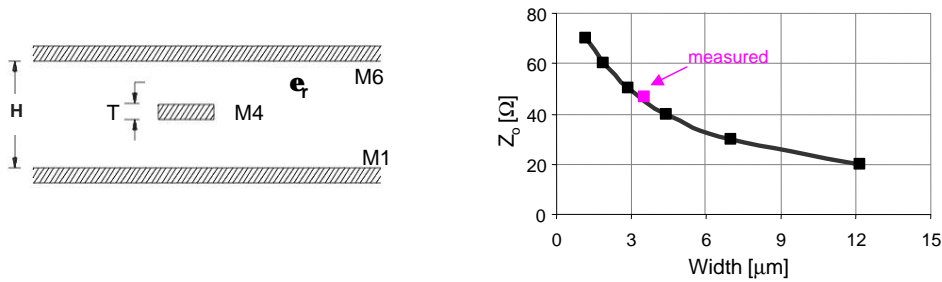


**Figure 4.18:** SL configuration (left) and characteristic impedance of the SL in function of the conductor width (right)

### Characterization of Transmission Line Structures

Figure 4.19 shows the microphotograph of the interconnect test structures (MS, CPW, and SL) used to extract the transmission line parameters. The striplines are invisible as they are fabricated in an intermediate metal layer  $M4$ . Interconnect test structures also includes the open structures for pad calibration which has same layout as the interconnect test structures but without the central conductor (not shown). The transmission line structures are characterized by S-parameter measurement in the frequency domain in range from 100 MHz to 40 GHz.

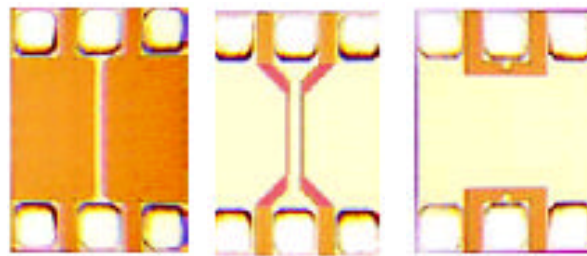


**Figure 4.19:** Microphotograph of the fabricated MS, CPW and SL (from left to right)

Figure 4.20 shows the measured losses for microstripline, coplanar waveguides, and striplines. Attenuation at 10 GHz is 0.45 dB/mm and 0.4 dB/mm for microstripline and coplanar waveguide, respectively. Due to the narrower width of the stripline, the attenuation is comparatively larger with respect to microstripline and coplanar waveguide. It is typically around 1.75 dB/mm at 10 GHz.

Frequency variation of the interconnect test structures are extracted directly from S-parameter measurement data. This information is essential for developing accurate and verified transmission line models for interconnect test structures. The simulation models up to 20 GHz are developed using the classical Telegraph model [102]. The detailed procedure is described in Appendix C. Table 4.1 lists the distributed circuit parameters ( $R$ ,  $L$ , and  $C$ ) extracted for per millimeter length of microstriplines, coplanar waveguides, and striplines.

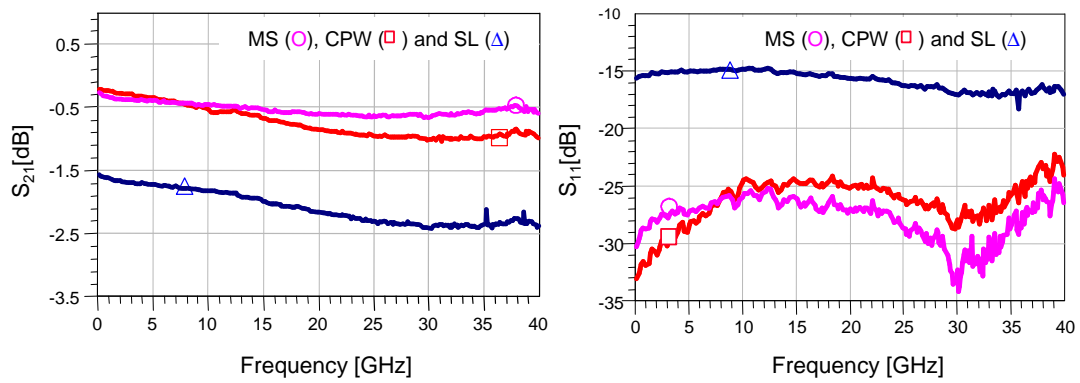


**Figure 4.20:** Comparison of measured MS, CPW and SL data for the magnitude  $S_{21}$  and  $S_{11}$

**Table 4.1:** Distributed circuit parameters for interconnect test structures

Type of TL	R( $\Omega$ /mm)	L(nH/mm)	C(pF/mm)
MS	5.2	0.32	0.13
CPW	5.0	0.28	0.17
SL	22.5	0.30	0.19

Extracted distributed resistance  $R$  of SL is almost four times larger than the resistance of MS and CPW. As a result, the attenuation of SL is also larger as compared to the attenuation of MS and CPW. Figures 4.21, 4.22 and 4.23 show the comparison of measured, simulated and modelled  $S_{21}$  magnitude and  $S_{21}$  phase data for MS, CPW and SL, respectively.

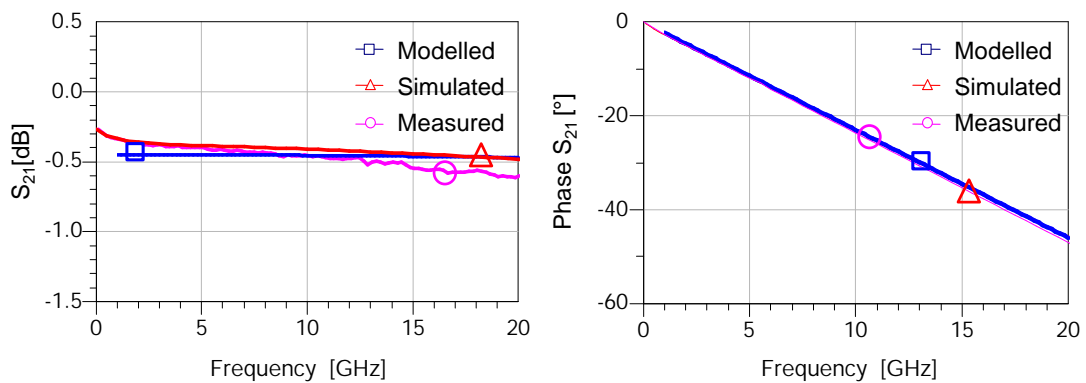


**Figure 4.21:** Comparison of measured, simulated and modelled MS data for the magnitude  $S_{21}$  (top-left), phase  $S_{21}$  (top-right) and magnitude  $S_{11}$  (bottom)

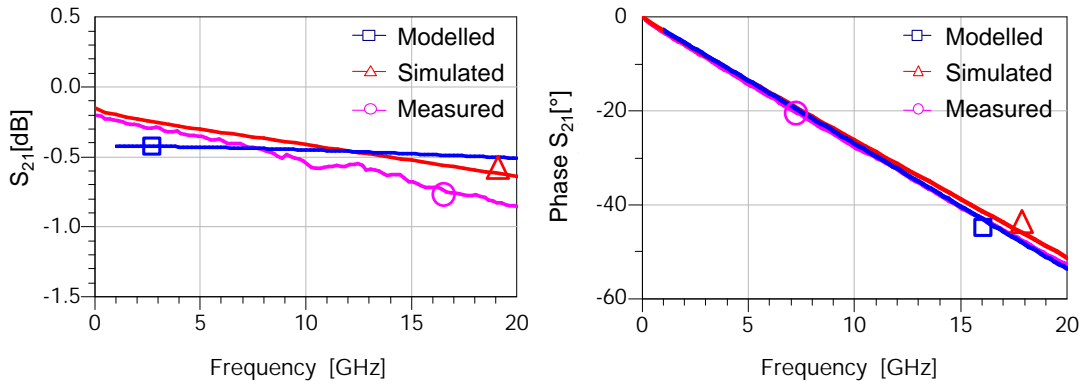


**Figure 4.22:** Comparison of measured, simulated and modelled CPW data for the magnitude  $S_{21}$  (top-left), phase  $S_{21}$  (top-right) and magnitude  $S_{11}$  (bottom)

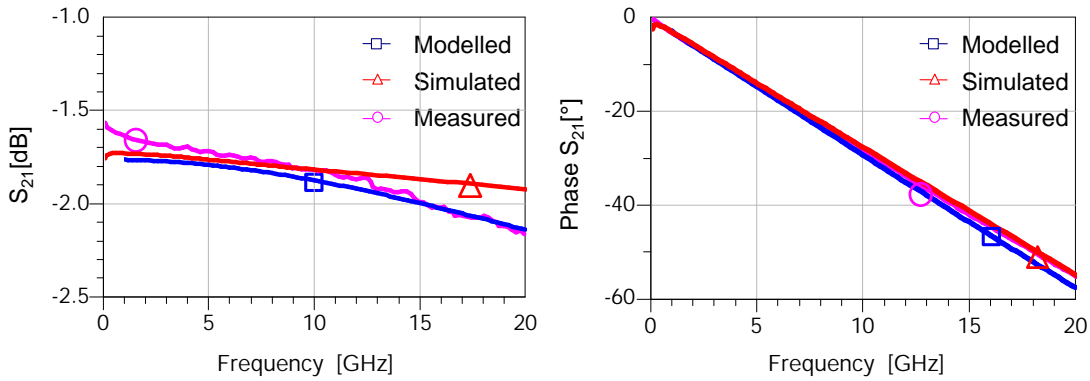
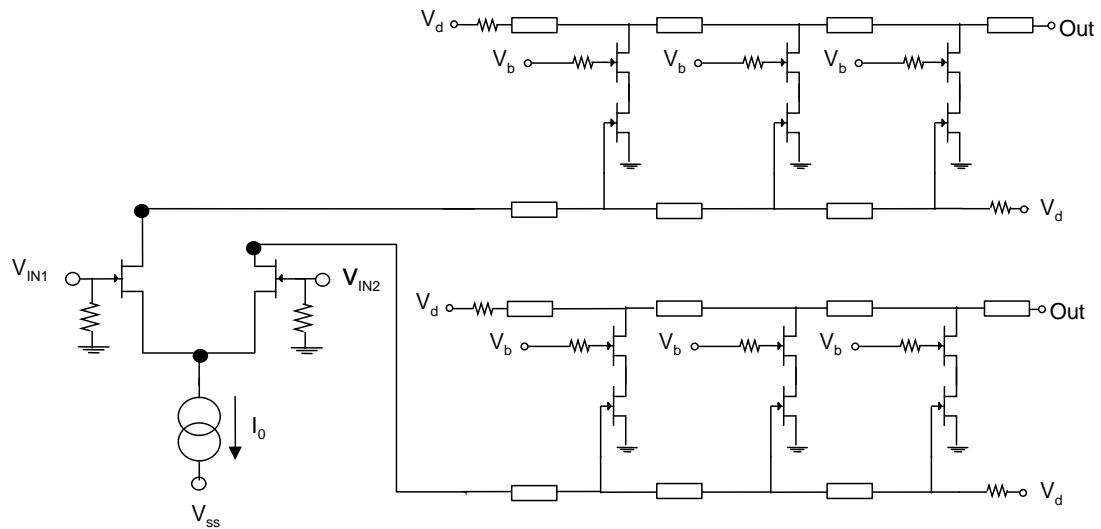


**Figure 4.23:** Comparison of measured, simulated and modelled SL data for the magnitude  $S_{21}$  (top-left), phase  $S_{21}$  (top-right) and magnitude  $S_{11}$  (bottom)

### 4.3.2 Circuit Design

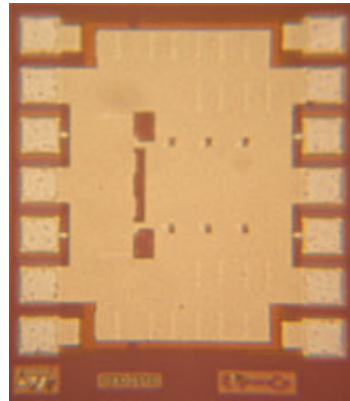
Recently, CMOS has emerged as an alternative to compound semiconductor or SiGe bipolar technology for integration of microwave and optical front-end circuits due to improvement of the RF performance, integration capability with baseband circuits, and most importantly the low cost. The motivation behind this work is to explore the limitation of CMOS distributed amplifier circuit design and analysis together with CMOS device and passive element modelling.

Equation (4.5), described in section 4.1, reduces to  $N = 1$  where  $N$  is the optimum number of stages required to maximize the gain of the CMOS distributed amplifier using striplines at 10 GHz and/or beyond. This indicates that the distributed gain using striplines is not possible in CMOS technology. However, as the striplines have a certain advantage in complex analogue circuitry for system integration, to study their behavior and limitations at 10 Gbit/s data rate, a differential amplifier using striplines was realized in  $0.18 \mu\text{m}$  CMOS technology. The amplifier consists of one differential stage followed by three pairs of distributed common-source common-gate (cascode) stages.



**Figure 4.24:** Schematic of the differential amplifier using striplines in CMOS

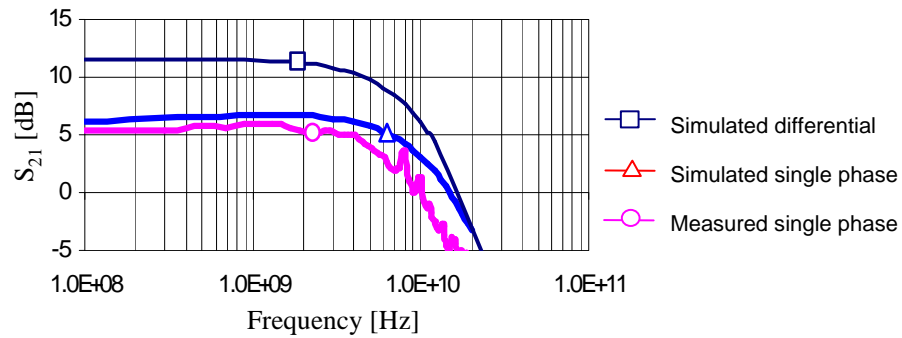
Figure 4.24 shows the schematic circuit diagram of the differential amplifier. Differential input signals are dc coupled to the differential preamplifier. The external gate bias of 1.3 V is applied through the bias Ts. The preamplifier input stage has on-chip  $50\ \Omega$  resistors to provide good impedance matching. The two output signals from the differential preamplifying stage are used to drive common-source common-gate stages which operate from single positive DC power supply of 1.8 V. A total length of the stripline's in each branch of the differential amplifier is  $665\ \mu\text{m}$ .



**Figure 4.25:** Microphotograph of the realized chip

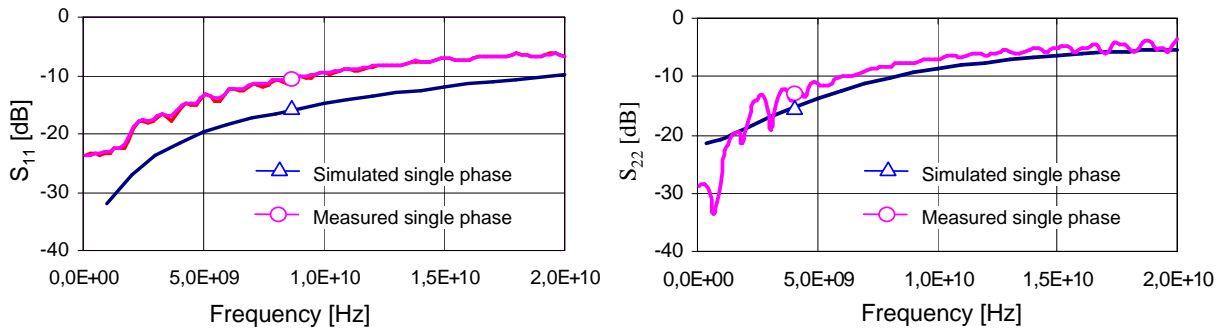
Figure 4.25 shows a microphotograph of the fabricated amplifier. The circuit elements are arranged symmetrically in layout to minimize the offset. Decoupling capacitors are connected between the power supply voltages and the ground. The power dissipation is 185 mW on a chip having an active area of  $0.5\ \text{mm}^2$ .

Figure 4.26 shows the simulated (differential input and single-phase input) and measured (single-phase input)  $S_{21}$ -parameter as a function of frequency. The simulated gain is 11.5 dB over the 7 GHz frequency range. The characteristic frequency response of the amplifier is measured using the wafer probe workstation and a HP network analyzer. To perform this measurement, the another differential input and the corresponding differential output is terminated with a  $50 \Omega$  resistor. The measured gain and 3 dB bandwidth is 6 dB and 6.2 GHz respectively. The simulated frequency response includes the effect of striplines but not the effect of parasitic layout capacitances. Thus, there is a slight mismatch of simulated and measured  $S_{21}$ -parameter.



**Figure 4.26:** Comparison of measured, simulated single phase and simulated differential magnitude of  $S_{21}$

Measured input and output reflection coefficients show acceptable performance.  $S_{11}$  is typically below -9.5 dB and  $S_{22}$  is below -7 dB up to 10 GHz range, as shown in Figure 4.27.



**Figure 4.27:** Comparison of measured, simulated single phase and simulated differential magnitude of  $S_{11}$

Figure 4.28 shows the exemplary measured eye diagram in single-phase configuration using a 10 Gbit/s  $2^7 - 1$  pseudorandom bit sequence signal (PRBS) having  $50 \text{ mV}_{pp}$  input amplitude. The differential structure also rejects the common mode interferences by 8 to 16 dB over 10 GHz frequency range.

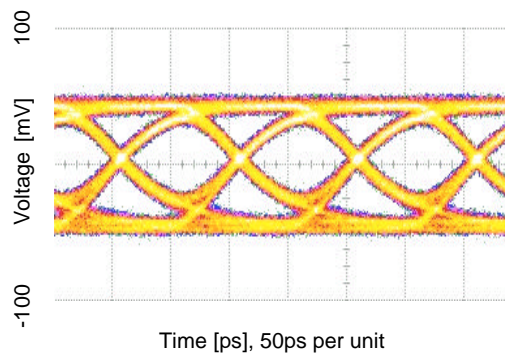


**Figure 4.28:** Measured eye diagram at 10 Gbit/s for  $2^7 - 1$  PRBS input signal

### 4.3.3 Result Discussion

Simulation models for the MS, CPW and SL are extracted to give fundamental insight in to transmission line structures realized in  $0.18 \mu\text{m}$  CMOS technology. A differential amplifier was designed and simulated using the above developed transmission line models. The differential amplifier was later fabricated in  $0.18 \mu\text{m}$  CMOS technology. The experiment demonstrates 10 Gbit/s signal propagation over narrow CMOS striplines. This opens the possibility of using striplines whenever over all good shielding is needed in complex analogue circuits.

The differential amplifier has a 3 dB bandwidth of 6.2 GHz. For single-phase input, the amplifier has the voltage gain of 6 dB at 10 Gbit/s and a CMRR of 8 dB. This is due to the fact that MOS transistor used in the constant current source of the differential amplifier has a very large size and is being operated with minimum gate-to-source voltage in order to provide larger bandwidth. To increase the CMRR of the amplifier, it is necessary to reduce the size of the current source MOS transistor as well as to provide the large voltage headroom. For n-channel MOS transistor, this is only possible by using triple-well technology [103]. The idea is to place the n-channel devices in p-wells, which are isolated from each other by n-wells and a third buried n-isolation implant. Simulation results show that two times better CMRR can be obtained by using this technology.

This CMOS circuit using striplines exhibits comparable performance with that of the state-of-the-art amplifiers designed in conventional technologies [44–46]. However, the results published in [45] and other similar publications have higher gain due to the fact that they have a significant transimpedance gain with very similar performance bandwidth. None of the referenced publication reports on the CMRR performance of the amplifier.

## 4.4 Conclusion

This chapter presents the simulation results on the design of differential travelling wave amplifier in pseudomorphic AlGaAs/InGaAs HEMT technology which combines the advantages of a differential and traveling wave designs. The circuit has 17 dB of differential

gain, 3 dB bandwidth of 46 GHz and a CMRR of 16.5 dB. The circuit could be employed as a differential linear amplifier for the reception of RZ-DPSK signals using the balanced optical front end to obtain high receiver sensitivity and a better OSNR.

Simulation models for the microstrip lines, coplanar waveguides and striplines are extracted from the measured S-parameter data. Simulated and measured results on the interconnect transmission line structure are compared. Moreover, the accurate models are later developed for advance simulation.

Finally, a 10 Gbit/s differential in differential out linear amplifier using striplines is designed and fabricated in 0.18  $\mu\text{m}$  CMOS technology. The experiment demonstrates a voltage gain of 6 dB with CMRR of 8 dB with a good eye opening at 10 Gbit/s.

# Chapter 5

## Result Discussion and Future Scope

The state of the art 40 Gbit/s differential phase shift keying and differential quadrature phase shift keying system was in-house developed using commercially available components. It was shown that signed online chromatic dispersion detection technique also works satisfactorily for the above mentioned modulation formats. The same technique was also used to adaptively compensate the chromatic dispersion of the various transmission spans using a thermally tunable dispersion compensator for RZ-DPSK modulation format. Furthermore, the DQPSK spectral efficiency was once more doubled using polarization division multiplexing and a 160 Gbit/s transmission per WDM channel was demonstrated using a thermally tunable dispersion compensator.

In order to implement optical transmission systems using either DPSK or DQPSK modulation formats, some special high-speed integrated circuits (ICs) are required. Therefore, a differential amplifier employing distributed amplifying stages that could be used to amplify the signals coming out of the balanced 40 Gbit/s DPSK/DQPSK optical receivers was simulated and designed in a pseudomorphic AlGaAs/InGaAs HEMT technology. Also a differential amplifier using striplines at 10 Gbit/s was designed, simulated, and later on fabricated in 0.18  $\mu\text{m}$  CMOS technology.

### 5.1 DPSK Transmission

Return-to-zero differential phase shift keying transmitter at 40 Gbit/s is developed in-house under the supervision of R. Noè. The optical transmitter uses a DFB laser at 192.5 THz as a source while a dual-drive Mach-Zehnder modulator was used to generate nonreturn-to-zero differential phase shift keying signal (NRZ-DPSK). Another dual-drive modulator was used as a pulse carver to generate Return-to-zero differential phase shift keying signal (RZ-DPSK).

Similarly, in-house developed balanced optical receiver uses a Mach-Zehnder interferometer having 4-bit delay as a delay demodulator and two high-speed photodiodes for balanced detection. This delay interferometer was thermally stabilized using the home made temperature controller. It was tuned using the differential micro-heaters with total

constant power. Main problem associated with this photonic lightwave circuit (PLC) is that it had nonnegligible polarization-dependent loss. As a result, the balanced optical receiver suffers nonnegligible transmission penalty due to polarization dependent phase shift that exist in the interferometer. One possibility to resolve this issue is to automatically adjust its phase using the available differential micro-heaters. This kind of automation can be implemented using the lock-in detection scheme. Therefore, one of the photodiode output was tapped using a pick-off T. The signal at the pick-off T was amplified using a chain of five 10 dB amplifiers at 10 GHz followed by a RF power detector. The output of the RF power detector drives the 400 Hz analogue lock-in amplifier and its output was used to stabilize the receiver interferometer. This scheme eliminates the polarization dependent phase shift and makes the system more robust with respect to temperature and occurring polarization changes in the fiber spans, and also to the laser frequency offsets [59].

The signed online chromatic dispersion (CD) detection scheme, previously demonstrated by D. Sandel for NRZ signals, was implemented, for the first time, for DPSK modulation format. This scheme introduces hardly any transmission penalty for DPSK modulation format using a balanced optical receiver even with an interferometer having 4-bit delay. The CD detection scheme offers the several advantages such as low cost of integration and high sensitivity of around 1 ps/nm in 1 ms measurement interval. It has wide dynamic range and detects the sign of the CD without any ambiguity.

Moreover, the residual chromatic dispersion of a 263 km fiber link at 40 Gbit/s for NRZ-DPSK and CS(RZ)-DPSK was compensated, for the first time, using the automatic control of a thermally tunable fiber Bragg grating based dispersion compensator. The total measured penalty of transmission and CD compensation was -1.2 dB ... +1.2 dB, for various link lengths and compensator CDs. As evident from our experiments, the CS(RZ)-DPSK modulation format outperforms the conventional modulation formats and hence we recommend it for long and ultra-long haul optical fiber transmission.

## 5.2 DQPSK Transmission

Spectral efficiency of the (CS)RZ-DPSK modulation format was doubled using differential quadrature phase shift keying (DQPSK) signal. The NRZ-DQPSK signal was generated interferometrically, using NRZ-DPSK signals. The transmitter interferometer was stabilized using a 10 KHz lock-in detection scheme. This 10 KHz phase modulation has a depth of 0.01 rad (rms) and does not introduce any transmission penalty. Carrier suppressed return-to-zero (CSRZ)-DQPSK signal was generated using a subsequent dual-drive Mach-Zehnder modulator driven at half of the clock rate.

$2 \times 40$  Gbit/s RZ-DQPSK transmission over 263 km fiber link with back-to-back receiver sensitivity of  $-27.5$  dBm and Q factor  $> 20$  dB is demonstrated [30]. The experiment shows sufficient resilience against non-linear phase noise and band limitation in a 40 Gbit/s WDM DEMUX with  $Q=17.5$  dB. Residual chromatic dispersion was manually tuned using a thermally tunable dispersion compensator. Especially, for this modulation format the automatic control of the tunable dispersion compensator using signed online

CD detection technique was not possible due to the nonnegligible polarization dependent loss of the receiver interferometer. It is very difficult to stabilize the receiver interferometer for DQSPK modulation format using the lock-in stabilization technique unless the receiver interferometer is free from the polarization dependent loss. Future scope of this work would be to either realize the delay interferometer with negligible polarization dependent loss or to implement automatic polarization control using the lithium niobate-based polarization transformers for the interferometer. Other possibility is to investigate or develop a new kind of lock-in stabilization technique that may work even in the presence of polarization dependent loss.

Further more, the spectral efficiency of the DQPSK signal was once more doubled using polarization division multiplex transmission [75]. This 160 Gbit/s transmission per WDM channel was demonstrated over 230 km of fiber with Q factor  $> 15$  dB using the automatic polarization control and a manually tunable dispersion compensation. A future scope of this work would be to transmit 160 Gbit/s signals with 40 DWDM channels having 100 GHz channel spacing in one single band in order to demonstrate the Tbit/s transmission capacity and spectral efficiencies beyond 1 bit/s/Hz. Fortunately, to date, such multi-terabit transmission experiments are recently demonstrated by [73, 74]. Future scope of this would be to transmit 40 DWDM channels with fully automatic tunable chromatic dispersion compensation using low-cost signed online chromatic dispersion detection scheme.

### **5.3 High-Speed Integrated Circuit for oDPSK Transmission**

A differential amplifier using distributed stages is designed and simulated in a pseudomorphic AlGaAs/InGaAs HEMT technology [35]. The circuit combines the two different concepts: differential and travelling wave concept, achieving the simulated flat gain of around 17 dB over the 46 GHz frequency range with a CMRR of 16.5 dB. Layout of this circuit was done using Cadence software. However, the circuit could not be fabricated due to several reasons. Future scope of this work would be to fabricate and characterize the circuit and to study and compare its measured characteristic properties with the simulated ones. Nevertheless, the latest publication [86] shows that the record sensitivity (39 photons/bit) can be achieved for the RZ-DPSK modulation format using differential travelling wave amplifier having a CMRR of  $> 20$  dB. Therefore, the further step would be to resimulate and redesign the differential distributed amplifier for higher CMRR using the experience gained using these trials.

A single-stage differential pre-amplifier followed by three pairs of spatially distributed common source stages using striplines, was designed and fabricated in standard  $0.18\mu\text{m}$  CMOS technology. For a single-phase input, amplifier has a gain of 6 dB at 10 Gbit/s. The measured 3 dB bandwidth is 6.2 GHz. The CMRR at 10 Gbit/s is 8 dB. The experiment demonstrates the possibility of using the striplines in low-cost standard CMOS technology at 10 Gbit/s. Amplifier performance is comparable with state-of-the-art ampli-

fiers designed in conventional technologies. This experience further open the possibilities of using striplines in CMOS technology where over all good shielding is needed. Further scope of this work would be to improve the CMRR of the amplifier as has been already discussed in chapter 4.

## **5.4 Conclusion**

This chapter summarizes transmission experiments done at 40 and 160 Gbit/s using the latest modulation formats such as return-to-zero–differential phase shift keying and differential quadrature phase shift keying which are currently under investigation for their future use in digital optical transmission systems. It also discusses the simulation and measurement results obtained on the differential amplifiers at 10 Gbit/s and 40 Gbit/s.

# Appendix A

## Definitions

### A.1 Bit Error Rate

The performance of a digital optical communication system is characterized by the bit-error-rate (BER). BER is defined as the average probability of incorrect bit identification. Therefore, a BER of  $10^{-6}$  corresponds to, on average, one error per million bits. Most of the digital optical communication systems specify a BER of  $\leq 10^{-9}$ . The BER with optimum setting of the decision threshold is given by

$$\text{BER} = \frac{1}{2} \text{erfc}\left(\frac{Q}{\sqrt{2}}\right) \quad (\text{A.1})$$

where erfc stands for the complementary error function and  $Q$ -factor is given by

$$Q = \frac{\mu_1 - \mu_0}{\sigma_1 + \sigma_0}. \quad (\text{A.2})$$

In the above expression for  $Q$ -factor, the  $\mu_1$  and  $\mu_0$  are the average intensity levels of the transmitted “1” and “0”, while  $\sigma_1$  and  $\sigma_0$  are standard deviation of the noise sources associated with the transmitted “1” and “0”, respectively. The expression (A.1) is not accurate enough since the derivation is based on the Gaussian approximation for the receiver noise statistics. The approximate form of (A.1) obtained by using the asymptotic expansion of  $\text{erfc}(Q/\sqrt{2})$  is reasonably accurate for  $Q > 3$  and is given by

$$\text{BER} \approx \frac{\exp(-Q^2/2)}{Q\sqrt{2\pi}}. \quad (\text{A.3})$$

The BER improves as  $Q$ -factor increases and becomes lower than  $10^{-12}$  for  $Q > 7$ . The receiver sensitivity corresponds to the average optical power for which  $Q = 6$ , since  $\text{BER} \approx 10^{-9}$  when  $Q = 6$ .

For the asynchronous ASK case,

$$\text{BER} \approx \frac{1}{2} \exp(-\eta N_p/4) \quad (\text{A.4})$$

where  $\eta$  is the quantum efficiency of the photodetector and  $N_p$  is a number of photons receiving during the bit “1”. If we assume  $\eta = 1$  the above equation shows that  $\text{BER} = 10^{-9}$  for  $N_p = 80$ . For ASK, this method gives a fairly good prediction of the BER, although the noise distribution in the intensity domain is not exactly Gaussian [56]. However, direct use of (A.4) in DPSK may lead to wrong prediction of the BER even in the linear regime due to the fundamentally non-Gaussian nature of the noise distribution in the output signal of the DPSK balanced receiver. The BER calculation is slightly more complicated for the DPSK case since is formed by the difference of two photo-currents. The final result is, however, quite simple and is given by

$$\text{BER} \approx \frac{1}{2} \exp(-\eta N_p). \quad (\text{A.5})$$

For  $\eta = 1$ , a BER of  $10^{-9}$  is obtained for  $N_p = 20$ . Thus DPSK provides 3 dB more system margin, than ASK.

## A.2 Receiver sensitivity

An important parameter that indicates the receiver performance is called receiver sensitivity. It is defined as minimum average received optical power for which the BER of the optical receiver is  $10^{-9}$ . The receiver sensitivity depends on the optical signal-to-noise ratio, as defined later, which in turn depends on various noise sources that corrupt the received optical signal.

## A.3 Optical signal-to-noise ratio

The optical signal-to-noise ratio (OSNR) is the measure of the ratio of signal power to noise power in an optical channel. It is usually measured with an Optical Spectrum Analyzer (OSA) and defined as

$$\text{OSNR} = 10 \log \left( \frac{S}{N} \right) \quad (\text{A.6})$$

where the symbol S represents the (linear) optical signal power and the symbol N is the (linear) optical phase power.

OSNR is important because it suggest a degree of impairment when the optical signal is carried by an optical transmission system that includes optical amplifiers. The detection of the signal is typically affected by attenuation and dispersion. With the use of the amplifiers, there is the additional impairment because the of noise seen in the receiver due to the presence of Amplified Spontaneous Emission noise (ASE). In practice, the use of an amplifier will help improve the signal because the increase in the signal amplitude will help overcome noise generated in the receiver’s front end. However, the optical background (noise) that accompanies the desired optical signal will be amplified along with the signal; consequently the OSNR will tend to degrade as it passes trough the transmission system.

The optical noise near signal wavelength can impair the receiver ability to properly decode the signal because of optical interference between the optical signal and optical noise. This impairment can be a bigger contributor to the BER than the power fluctuation in the optical noise.



## Appendix B

# Theory of the Traveling Wave Amplifier

The basic idea behind the design of traveling wave amplifier is to absorb the parasitic capacitances of the transistors into the transmission line and making them as a part of the passive network. For this explanation, there is a need to develop the expression for the complex propagation constant,  $\gamma$ , of a lossy transmission line shown in Figure B.1.

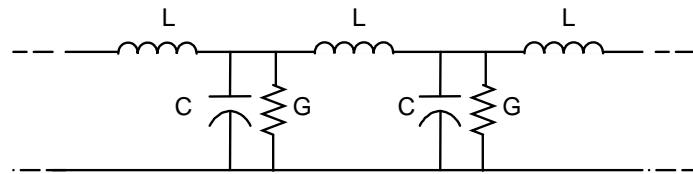


**Figure B.1:** Lumped transmission line with shunt loss

Generally,

$$\gamma = \alpha + j\beta = \sqrt{(R + j\omega L)(G + j\omega C)}. \quad (\text{B.1})$$

In this expression and in Figure B.1 the elements  $R$ ,  $L$ ,  $G$  and  $C$  may be expressed in per section terms for a lumped component artificial transmission line, or in per unit distance terms for a uniform transmission line.  $\alpha$  and  $\beta$  are the attenuation and phase constants, respectively. The characteristic impedance,  $Z$ , of the transmission line is

$$Z = \sqrt{\frac{R + j\omega L}{G + j\omega C}}. \quad (\text{B.2})$$

Combining above two equations gives

$$\gamma = (G + j\omega C)Z. \quad (\text{B.3})$$

For  $G \ll \omega C$  and  $R \ll \omega L$ ,  $\gamma$  may be approximated as follows:

$$\gamma = (G + j\omega C) \left( \frac{j\omega L}{G + j\omega C} \right)^{1/2} \quad (\text{B.4})$$

The further simplification of (B.4) leads to:

$$\gamma = (G + j\omega C) \left(\frac{L}{C}\right)^{1/2} \left(1 + \frac{G}{j\omega C}\right)^{-1/2} \quad (\text{B.5})$$

where for  $G \ll \omega C$ , the expression  $(1 + G/j\omega C)^{-1/2}$  can be approximated by the first order of McLaurin series as  $1 - G/2j\omega C$ , and this leads to

$$\gamma = \left(G + j\omega C - \frac{G}{2} - \frac{G^2}{2j\omega C}\right) \sqrt{\frac{L}{C}}. \quad (\text{B.6})$$

For  $G \ll \omega C$  and  $(G^2/2\omega C)\sqrt{L/C} \approx 0$  the expression (B.5) can be written as:

$$\gamma = \left(\frac{G}{2} + j\omega C\right) \sqrt{\frac{L}{C}} \quad (\text{B.7})$$

Thus, the attenuation constant,  $\alpha$ , and the phase constant,  $\beta$ , are given by

$$\begin{aligned} \alpha &\approx \frac{G}{2} \sqrt{\frac{L}{C}}. \\ \beta &\approx \omega \sqrt{LC} \end{aligned} \quad (\text{B.8})$$

For lossless case,  $Z_0$  even can be approximated by

$$Z_0 \approx \sqrt{\frac{L}{C}}. \quad (\text{B.9})$$

In a practical amplifier the inductors are realized with the lengths of transmission line. Regardless, the inductors not only have inductance per unit length but they also have capacitance associated with them. This capacitance must be included together with the device capacitance in full analysis.

For the drain line, the transmission line section between the FETs are taken to be of electrical length  $l_d$ . The total effective inductance per unit length of the transmission line will be termed  $L'_d$ . If the capacitance per unit length of the transmission line is  $C'_d$ , the total capacitance,  $C'_D$ , per unit length of the drain line is given by

$$C'_D = C'_d + \frac{C_o}{l_d} \quad (\text{B.10})$$

where  $C_o$  is the total output capacitance of the transistor. The Figure B.2 shows a section of the drain line, from which the shunt conductance per unit length,  $G_D$

$$G_D = (1/r_0) \times 1/l_d \quad (\text{B.11})$$

Using the results of equations (B.8) and (B.9), the attenuation per unit length along the

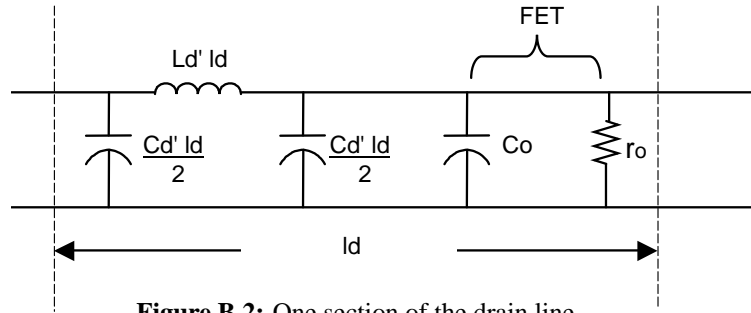


**Figure B.2:** One section of the drain line

drain line is

$$\alpha_D = \frac{1}{2r_0 l_d} \sqrt{\frac{L'_d}{C'_d + C_o/l_d}} \quad (\text{B.12})$$

The phase constant in radians per unit distance along the drain line is

$$\beta_D \approx \omega \sqrt{L'_d (C'_d + C_o/l_d)} \quad (\text{B.13})$$

The characteristic impedance is

$$Z_{0D} \approx \sqrt{\frac{L'_d}{C'_d + C_o/l_d}} \quad (\text{B.14})$$

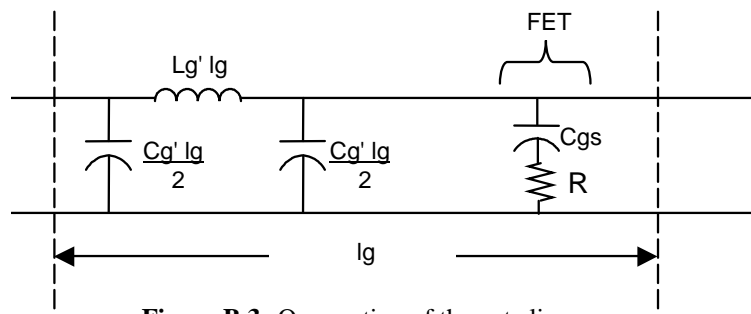


**Figure B.3:** One section of the gate line

For the gate line the procedure is almost same as for the drain line except for the fact that the equivalent circuit of the transistor is now a series RC network. The impedance of the series RC network is given by

$$Z = R + \frac{1}{j\omega C_{gs}} \quad (\text{B.15})$$

The admittance is

$$Y = Z^{-1} = \frac{j\omega C_{gs} + \omega^2 C_{gs}^2 R}{1 + \omega^2 C_{gs}^2 R^2} \quad (\text{B.16})$$

In the above expression,  $\omega^2 C_{gs}^2 R^2 \ll 1$  so that one may take the denominator roughly equal to unity and hence

$$Y \approx j\omega C_{gs} + \omega^2 C_{gs}^2 R. \quad (\text{B.17})$$

Following a procedure identical to that employed for the drain line, we can now write, for the gate line, the inductance per unit length is given by  $L'_g$ . Similar to drain line the  $C'_g$  is the capacitance per unit length of the gate transmission line,  $C'_G$  is the total capacitance per unit length of the gate line,  $C_{gs}$  is the capacitance of the transistor.

$$C'_G = C'_g + \frac{C_{gs}}{l_g} \quad (\text{B.18})$$

The conductance per length is given with

$$G'_G = \frac{\omega^2 C_{gs}^2 R}{l_g} \quad (\text{B.19})$$

Making a use of equations (B.8) and (B.9), the attenuation and phase constant,  $\alpha_G$  and  $\beta_G$ , of a gate line are expressed as

$$\alpha_G \approx \frac{\omega^2 C_{gs}^2 R}{2l_g} \sqrt{\frac{L'_g}{C'_g + C_{gs}/l_g}} \quad (\text{B.20})$$

$$\beta_G \approx \omega \sqrt{L'_g (C'_g + C_{gs}/l_g)} \quad (\text{B.21})$$

and gate impedance is given by

$$Z_{0G} \approx \sqrt{\frac{L'_g}{C'_g + C_{gs}/l_g}}. \quad (\text{B.22})$$

Equations (B.12) and (B.20) respectively give the attenuation coefficient of signals propagating along the drain and gate lines. Similarly, equations (B.13) and (B.21) give the phase delay per unit length along the two lines and equations (B.14) and (B.22) give their characteristic impedances. All this quantities appear in the expression for the power gain of the amplifier which will now be derived.

Consider the path from the input, via FET  $k$ , to the output, as shown in Figure B.4. The signal wave propagating along the gate line of FET  $k$  has an amplitude

$$V_{gk} = V_{go} \exp(-\alpha_G k l_g). \quad (\text{B.23})$$

FET  $k$  generates a current  $I_{dk}$  in response. Assuming half of  $I_{dk}$  goes into the wave propagating towards the external load, the current actually entering the load has an amplitude of

$$I_{ok} = \frac{I_{dk}}{2} \exp[-\alpha_D (N - k) l_d] \quad (\text{B.24})$$

But

$$I_{dk} = g_{ko}V_{gk} = g_{ko}V_{go} \exp(-\alpha_G k l_g) \quad (\text{B.25})$$

Therefore

$$I_{ok} = \frac{g_{ko}}{2} V_{go} \exp(-\alpha_D N l_d) \exp[k(\alpha_D l_d - \alpha_G l_g)]. \quad (\text{B.26})$$

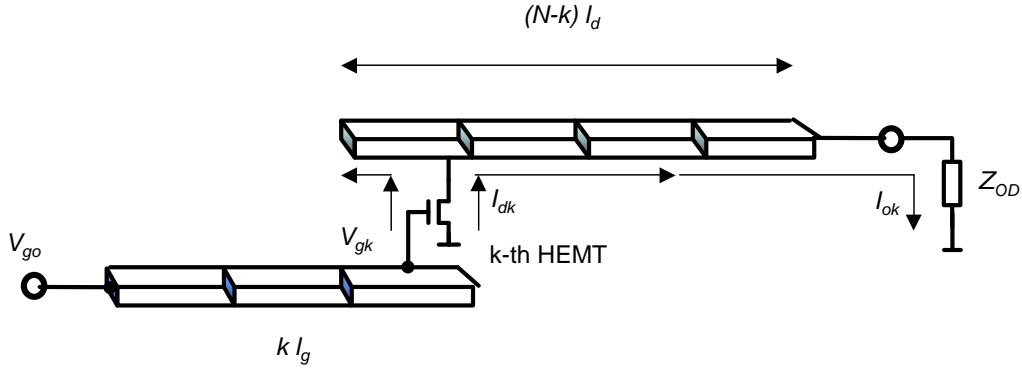


**Figure B.4:** Signal path from the input to the output via the 'k'-th transistor

If the phase delay per section of the gate line is equal to the phase delay per section of the drain line, all components  $I_{ok}$  arising from the individual FETs will add in-phase so that the total current in the external load,  $I_{out}$ , can be found by summing the magnitudes  $I_{ok}$  given by equation (B.26). The sum is taken over  $1 \leq k \leq N$ . This summation can be replaced by an integration. Taking the integration limits from 1 to  $N$  would be appropriate if amplifier uses  $N$  number of FETs. But taking the limits from 0 to  $N$  is even more appropriate given that the total length of the lines involved and hence for determining the total attenuation. Since the integration affects the last term in equation (B.26), a term which expresses attenuation assume limits from 0 to  $N$ . Thus, the total output current is

$$\begin{aligned} I_{out} &= \frac{g_{ko}}{2} V_{go} \exp(-\alpha_D N l_d) \int_0^N \exp[k(\alpha_D l_d - \alpha_G l_g)] dk \\ &= \frac{g_{ko}}{2} V_{go} \frac{\exp(-\alpha_G N l_g) - \exp(-\alpha_D N l_d)}{\alpha_D l_d - \alpha_G l_g} \end{aligned} \quad (\text{B.27})$$

The amplifier power gain is defined as

$$G_p = \frac{P_{out}}{P_{in}}. \quad (\text{B.28})$$

The input power to the amplifier is given by

$$P_{in} = \frac{V_{go}^2}{Z_{OG}} \quad (\text{B.29})$$

while the amplifier output power is given by

$$P_{out} = I_{out}^2 Z_{OD}. \quad (\text{B.30})$$

As a result, the power gain is given by the following equation which is used in chapter 4.

$$G_p = \frac{g_{ko}^2 Z_{OG} Z_{OD} [\exp(-\alpha_G N l_g) - \exp(-\alpha_D N l_d)]^2}{4(\alpha_D l_d - \alpha_G l_g)^2} \quad (\text{B.31})$$

## Appendix C

# Extraction of Transmission Line Parameters

Interconnect signal transmission is based on the solution of the classical Telegraph transmission line equation [102]. A model has been developed that presents, in the frequency domain the interconnect voltage and current in terms of propagation constant,  $\gamma$  and characteristic impedance,  $Z$ . Then the impedance and the propagation constant are described by four distributed transmission line parameters,  $R$ ,  $L$ ,  $C$ , and  $G$ . An infinitely small section of this model incorporating distributed circuit elements are shown in Figure C.1.

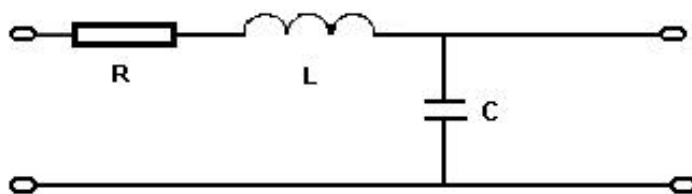


**Figure C.1:** Single transmission line represented by a two-port network and described with distributed transmission line parameters  $R$ ,  $L$ ,  $C$  and  $G \rightarrow 0$

These distributed circuit parameters describe per unit length values and not the lumped element values that are assumed in simulation. IC interconnect circuit elements  $Z$ ,  $\gamma$ ,  $R$ ,  $L$ ,  $C$ , and  $G$  are shown to be function of frequency. To solve the Telegraph equation for IC interconnect- signal propagation requires an understanding of S-parameter based interconnect test structure characterization. Single line IC interconnect transmission is represented by a two port network and is tested in a controlled ( $Z_o = 50\Omega$ ) impedance microwave measurement system. The S-parameter response measured from a lossy unmatched transmission line with parameters  $\gamma$  and  $Z$  in a  $Z_o$  impedance system are:

$$[S] = \frac{1}{D_s} \begin{bmatrix} (Z^2 - Z_0^2) \sinh \gamma l & 2ZZ_0 \\ 2ZZ_0 & (Z^2 - Z_0^2) \sinh \gamma l \end{bmatrix} \quad (\text{C.1})$$

where

$$D_s = 2ZZ_0 \cosh \gamma l + (Z^2 + Z_0^2) \sinh \gamma l. \quad (\text{C.2})$$

Since the above matrix is symmetrical it contains two independent linear equations. This S-parameter matrix is converted to ABCD parameters, which incorporated the interconnect propagation constant  $\gamma(\omega)$  and impedance  $Z(\omega)$  more explicitly. The equivalent ABCD matrix is

$$[ABCD] = \begin{bmatrix} \cosh \gamma l & Z \sinh \gamma l \\ (1/Z) \sinh \gamma l & \cosh \gamma l \end{bmatrix} \quad (\text{C.3})$$

The relationship between S parameters and ABCD matrix is:

$$A = \frac{(1 + S_{11} - S_{22} - \Delta S)}{2S_{21}} \quad (\text{C.4})$$

$$B = \frac{(1 + S_{11} + S_{22} + \Delta S)Z_0}{2S_{21}} \quad (\text{C.5})$$

$$C = \frac{(1 - S_{11} - S_{22} + \Delta S)Z_0}{2S_{21}Z_0} \quad (\text{C.6})$$

$$D = \frac{(1 - S_{11} + S_{22} - \Delta S)}{2S_{21}} \quad (\text{C.7})$$

where

$$\Delta S = S_{11}S_{22} - S_{21}S_{12} \quad (\text{C.8})$$

The equations (C.1)–(C.7) are combined to yield

$$e^{-\gamma l} = \left\{ \frac{1 - S_{11}^2 + S_{21}^2}{2S_{21}} \pm K \right\}^{-1} \quad (\text{C.9})$$

where

$$K = \left\{ \frac{(S_{11}^2 - S_{21}^2 + 1)^2 - (2S_{11})^2}{2S_{21}^2} \right\}^{1/2} \quad (\text{C.10})$$

and

$$Z^2 = Z_0^2 \frac{(1 + S_{11})^2 - S_{21}^2}{(1 - S_{11})^2 - S_{21}^2} \quad (\text{C.11})$$

During the extraction of complex parameter  $\gamma$  and  $Z$  from  $e^{-\gamma}$  and  $Z^2$ , the cylindrically mapped phase output of the S-parameter network analyzer ( $-180^\circ$  to  $180^\circ$ ) is converted to the true radian measurement phase which can be any real value. Also, extracted parameter with values that are not physical satisfy the Telegraph equation for propagation in the

negative direction. Once  $\gamma$  and  $Z$  are determined, then from standard transmission line relationships, characteristic impedance,  $Z$ , (B.1) and complex propagation constant,  $\gamma$ , (B.2), given in Appendix B, follows

$$\begin{aligned}R &= \text{Re}\{\gamma Z\} \\L &= \text{Im}\{\gamma Z\}/\omega \\G &= \text{Re}\{\gamma/Z\} \\C &= \text{Im}\{\gamma/Z\}/\omega\end{aligned}\tag{C.12}$$

Thus, the Telegraph equation transmission line model parameters are determined by combining (C.12).



# References

- [1] R. Cowper, M. OSullivan, G. Ribakovs, K. Roberts, “Perspectives on the Evolution of Next Generation High-Capacity Systems”, *Nortel Networks Inc.*, (1999).
- [2] Freedonia Custom Research, “Fiber Optics to 2006: Products and Systems”, *The Freedonia Group Inc.*, (June, 2002), Industry Study No.1550.
- [3] S. C. Rashleigh, R. Ulrich, “Polarization Mode Dispersion in Single-Mode Fibers”, *Optic. Letters*, **vol. 3**, (1978), 60–62.
- [4] J. G. Proakis, “*Digital Commmunications*,”, Electrical Engineering, McGraw-Hill Inc., 2. edition, (1989).
- [5] J. Leibrich, C. Wree, W. Rosenkranz, “CF-RZ-DPSK for Suppression of XPM on Dispersion-managed Long-Haul Optical WDM Transmission on Standard Single-Mode Fiber”, *IEEE Photonics Technology Letters*, **vol. 14**, (2002), 155-157.
- [6] L. Becouarn, G. Varelle, P. Pecci, J. F. Marcerou, “3 Tbit/s Transmission (301 DPSK Channels at 10.709 Gb/s) Over 10 270 km with a Record Efficiency of 0.65 bit/s/Hz”, *Proc. ECOC2003, Rimini, Italy*, (2003), PDP Th4.3.2.
- [7] I. Morita, N. Edagawa, “50-GHz-Spaced  $64 \times 42.7$  Gbit/s Transmission over 8200 km Using Pre-Filtered CS-RZ DPSK Signal and EDFA Repeaters ”, *Proc. ECOC2003, Rimini, Italy* (2003), PDP, Th4.3.1.
- [8] A. H. Gnauck, P. J. Winzer, “Optical Phase-Shift-Keyed Transmission”, *Journal of Lightwave Technology*, **vol. 23**, (January, 2005), 115-130.
- [9] T. Chikama, S. Watanabe, T. Naito, H. Onaka, T. Kiyonaga, Y. Onoda, H. Miyata, M. Suyama, M. Seino, H. Kuwahara, “Modulation and Demodulation Techniques in Optical Heterodyne PSK Transmission Systems”, *Journal of Lightwave Technology*, **vol. 8**, (March, 1990), 309-325.
- [10] R. A. Linke, A. H. Gnauck, “High-Capacity Coherent Lightwave Systems”, *Journal of Lightwave Technology*, **vol. 6**, (1988), 1750-1769.
- [11] A. H. Gnauck, S. Chandrasekhar, J. Leuthold, L. Stulz, “Demonstration of 42.7 Gb/s DPSK Receiver with 45 Photons/Bit Sensitivity”, *IEEE Photonics Technology Letters*, **vol. 15**, (January, 2003), 99-101.

- [12] W. Idler, A. Klekamp, R. Dischler, J. Lazaro, A. Konczykowska, "System Performance and Tolerances of 43 Gb/s ASK and DPSK Modulation Formats", *Proc. ECOC2003, Rimini, Italy*, (2003), Th2.6.3.
- [13] S. R. Chinn, D. M. Boroson, J. C. Livas, "Sensitivity of Optically Preamplified DPSK Receivers with Fabry-Perot Filters", *Journal of Lightwave Technology*, **vol. 14**, (March, 1996), 370-376.
- [14] A.H. Gnauck, G. Raybon, S. Chandrasekhar, J. Leuthold, C. Doerr, L. Stulz, A. Agarwal, S. Banerjee, D. Grosz, S. Hunsche, A. Kung, A. Marhelyuk, D. Maywar, M. Movassaghi, X. Liu, C. Xu, X. Wei, D.M. Gill, "2.5 Tb/s ( $64 \times 42.7$  Gb/s) Transmission over 40x100 km NZDSF Using RZ-DPSK Format and All-Raman-Amplified Spans", *Proc. OFC2002, Anaheim, CA* (2002), PD FC2.
- [15] C. Rasmussen, T. Fjelde, J. Bennike, F. Liu, S. Dey, B. Mikkelsen, P. Mamyshev, P. Serbe, P. van der Wagt, Y. Akasaka, D. Harris, D. Gapontsev, V. Ivshin, P. Reeves-Hall, "DWDM 40 Gb/s Transmission over Trans-Pacific Distance (10,000 km) Using CSRZ-DPSK, Enhanced FEC and All-Raman Amplified 100 km Ultra-Wave Fiber Spans", *Proc. OFC2003, Atlanta, GA, USA*, (2003), PD 18.
- [16] B. Zhu, L.E. Nelson, S. Stulz, A.H. Gnauck, C. Doerr, J. Leuthold, L. Grner-Nielsen, M.O. Pedersen, J. Kim, R. Lingle, Jr., Y. Emori, Y. Ohki, N. Tsukiji, A. Oguri, S. Namiki, "6.4 Tb/s ( $160 \times 42.7$  Gb/s) Transmission with 0.8 bit/s/Hz Spectral Efficiency over  $32 \times 100$  km of Fiber Using CSRZ-DPSK Format", *Proc. OFC2003, Atlanta, GA, USA*, (2003), PD 19.
- [17] G. Vareille, L. Becouarn, P. Pecci, P. Tran, J.F. Marcero, "8370 km with 22 dB Spans ULH Transmission of  $185 \times 10.709$  Gbit/s RZ-DPSK Channels", *Proc. OFC2003, Atlanta, GA, USA* (2003), PD 20.
- [18] J.X. Cai, D.G. Foursa, C.R. Davidson, Y. Cai, G. Domagala, H. Li, L. Liu, W.W. Patterson, A.N. Pilipetskii, M. Nissov, N.S. Bergano, "A DWDM Demonstration of 3.73 Tb/s over 11,000 km Using 373 RZ-DPSK Channels at 10 Gb/s", *Proc. OFC2003, Atlanta, GA, USA* (2003), PD 22.
- [19] T. Tsuritani, K. Ishida, A. Agata, K. Shimomura, I. Morita, T. Tokura, H. Taga, T. Mizuochi, N. Edagawa, "70 GHz-Spaced  $40 \times 42.7$  Gbit/s Transmission over 8700 km Using CS-RZ DPSK Signal, All-Raman Repeaters and Summetrically Dispersion-Managed Fiber Span", *Proc. OFC2003, Atlanta, GA, USA* (2003), PD 23.
- [20] G. Charlet, J. Lazaro, E. Corbel, P. Tran, A. Klekamp, T. Lopez, H. Mardoyan, W. Idler, A. Konczykowska, J.-P. Thiery, R. Dischler, S. Bigo, "One-Hundred WDM-Channel Transatlantic Transmission Experiment at 43 Gbit/s Using Raman Repeaters with Large 65-km Spacing", *Proc. ECOC2003, Rimini, Italy* (2003), Postdeadline paper Th4.3.3.
- [21] B. Milivojevic, D. Sandel, S. Bhandare, R. Noé, F. Wüst, "Practical 40 Gbit/s CSRZ-DPSK Transmission System with Signed Online Chromatic Dispersion Detection", *Proc. ECOC2003, Rimini, Italy*, (2003), Tu3.6.4.

- [22] B. Milivojevic, D. Sandel, S. Bhandare, R. Noé, F. Wüst, "Chromatic Dispersion Detection in a 40 Gbit/s CSRZ-DPSK Transmission", *Proc. YUINFO04, Kopaonik, Serbia and Montenegro*, **vol. 58**, (2004), 91.
- [23] D. Sandel, S. Bhandare, B. Milivojevic, R. Noé, M. Guy, M. Lapointe, "Automated Tunable Chromatic Dispersion Compensation at 40 Gbit/s", *Proc. 5. ITG-Fachtagung Photonische Netze, Leipzig, Germany* (May, 2004), 199–201.
- [24] R. A. Griffin, A. C. Carter, "Optical Differential Quadrature Phase Shift Key (oDQPSK) for High capacity Optical Transmission", *Proc. OFC02, Atlanta, GA, USA*, **WX6** (2002), 367-368.
- [25] Pak S. Chao, Vladimir S. Grigoryan, Yuri A. Godin, Aviv Salamon, Yaakov Achiam, "Transmission of 25 Gb/s RZ-DQPSK Signals with 25 GHz Channel Spacing over 1000 km of SMF-28 Fiber", *IEEE Photonics Technology Letters*, **vol. 15**, (2003), 473–475.
- [26] Hoon Kim, Ren-Jean Essiambre, "Transmission of  $8 \times 20$  Gb/s DQPSK Signals with 25 GHz Channel Spacing over 310 km SMF with 0.8 b/s/Hz Spectral Efficiency", *IEEE Photonics Technology Letters*, **vol. 15**, (2003), 769–771.
- [27] Christoph Wree, Nancy Hecker-Denschlag, Erich Gottwald, Peter Krummrich, Jochen Leibrich, Ernst-Dieter Schmidt, Berthold Lankl, Werner Rosenkranz, "High Spectral Efficiency 1.6 b/s/Hz Transmission ( $8 \times 40$  Gb/s With 25 GHz Grid) over 200 km SSMF Using RZ-DQPSK and Polarization Multiplexing", *IEEE Photonics Technology Letters*, **vol. 15**, (2003), 1303–1305.
- [28] N. Yoshikane, I. Morita, "1.14 b/s/Hz Spectral Efficiency  $50 \times 85.4$  Gb/s Transmission over 300 km Using Copolarized CS-RZ DQPSK Signals", *Proc. OFC2004* (2004), PDP38.
- [29] C. Wree, M. Serbay, W. Rosenkranz, "Toward 1.6 b/s/Hz Spectral Efficiency by Strong Optical Filtering of RZ-DQPSK", *Proc. ECOC2003, Rimini, Italy*, **We4.P.126** (September, 2003), 808-809.
- [30] S. Bhandare, D. Sandel, B. Milivojevic, A. Fauzi Abas Ismail, A. Hidayat, R. Noé, "2×40 Gbit/s RZ-DQPSK Transmission", *Proc. 5. ITG-Fachtagung Photonische Netze, Leipzig, Germany* (May, 2004), 195–197.
- [31] Y. Zhu, K. Cordina, N. Jolley, R. Feced, H. Kee, R. Rickard, A. Hadjifotiou, "1.6 bit/s/Hz Orthogonally Polarized CSRZ-DQPSK Transmission of  $8 \times 40$  Gbit/s over 320 km NDSF", *Proc. OFC2004* (2004), TuF1.
- [32] S. Bhandare, D. Sandel, A. F. Abas, B. Milivojevic, A. Hidayat, R. Noé, M. Guy, M. Lapointe, "2×40 Gbit/s RZ-DQPSK Transmission over 263 km of Fiber with Tunable Chromatic Dispersion Compensator", *IEE Electronics Letters*, **vol. 13**, (June, 2004), 821–822.
- [33] D. Sandel, V. Mirvoda, F. Wüst, R. Noé, "PMD Compensation in a 2×40 Gbit/s, 212 km, CS-RZ Polarization Multiplexed Transmission Experiment", *Proc. ECOC2001*, **PD.B.1.4** (2001).

- [34] B. Milivojevic, A. Fauzi Abas, A. Hidayat, S. Bhandare, D. Sandel, R. Noé, M. Guy, M. Lapointe, "160 Gbit/s, 1.6 bit/s/Hz RZ-DQPSK Polarization-Multiplexed Transmission over 230km Fiber with TDC", *Proc. ECOC04, Stockholm, Sweden*, (September, 2004), We1.5.5.
- [35] B. Milivojevic, S. Hoffmann, A. Thiede, R. Noé, R. Leblanc, B. Wroblewski, "Distributed Amplifiers for Transmitter and Receiver of a 40 Gbit/s DPSK Optical Transmission System", *Proc. European Microwave Week, The European Gallium Arsenide and other Compound Semiconductors Application Symposium, GAAS2004, Amsterdam, The Netherlands*, (October, 2004), 9–12.
- [36] W. Mouzannar, F. Jorge, S. Vuye, E. Dutisseuil, R. Lefevre, "40 Gbit/s High Performance GaAs P-HEMT High Voltage Modulator Driver for Long Hual Optical Fiber Communication", *IEEE GaAs Digest* (2002), 163–166.
- [37] A. Hillsmann, V. Hurm, F. Steinhagen, A. Thiede, M. Schlechtweg, "40 Gbit/s High Voltage Modulator Driver in P-HEMT Technology", *IEE Electronics Letters*, **vol. 35**, (1999), 1–2.
- [38] H. Shigematsu, M.Sato, T. Hirose, Y. Watanabe, "A 54-GHz Distributed Amplifier with 6-Vpp Output for a 40 Gbit/s  $LiNbO_3$  modulator driver", *IEEE Journal of Solid-State Circuits*, **vol. 37**, (September, 2002), 1100–1105.
- [39] S. Hoffmann, J. R. Ojha, A. Thiede, R. Leblanc, B. Wroblewski, "7 Vpp Modulator-Driver for 40 Gbit/s Optical Communications", *Proc. of European Microwave Week, The European Gallium Arsenide and Other Compound Semiconductors Application Symposium, GaAs2002* (2002), 181–184.
- [40] C.Meliani, G.Rondeau, G.Post, J.Decobert, W.Mouzannar, E.Dutisseuil, R.Lefvre, "A High Gain-Bandwidth Product InP HEMT Distributed Amplifier with 92 GHz Cut-off Frequency for 40 Gbit/s Applications and Beyond", *IEEE GaAs Digest* (2002), 103–106.
- [41] C.Meliani, G.Post, G.Rondeau, J.Decobert, W.Mouzannar, E.Dutisseuil, R.Lefvre, "DC-92 GHz Ultra-Broadband High Gain InP HEMT Amplifier with 410 GHz Gain-Bandwidth Product", *IEE Electronics Letters*, **vol. 38**, (September, 2002), 1175–1177.
- [42] S. Masuda, T. Hirose, T. Takahashi, M. Nishi, S. Yokokawa, S. Lijima, K. Ono, N. Hara, K. Joshin, "An Over 110 GHz InP HEMT Flip-Chip Distributed Baseband Amplifier with Inverted Microstrip Line Structure for Optical Transmission System", *IEEE GaAs Digest* (2002), 99–102.
- [43] B. Milivojevic, Z. Gu, A. Thiede, "10 Gbit/s Differential Amplifier Demonstrating Striplines in 0.18 $\mu$ m CMOS Technology", *Proc. of European Microwave Week, The European Gallium Arsenide and other Compound Semiconductors Application Symposium, GAAS2005*, accepted.
- [44] E. Sckinger, and W. C. Fischer, "A 3 GHz 32 dB CMOS Limiting Amplifier for SONET OC-48 Receivers", *IEEE Journal of Solid-State Circuits*, **vol. 35**, (December, 2000), no.12, 1884-1888.

- [45] Rui Tao, M. Berroth, Zheng Gu and Zhi Gong Wang, "Wideband Fully Differential CMOS Transimpedance Preamplifier", *Electronic Letters*, **vol. 39**, (October, 2003), no.21, 1488-1490.
- [46] Holdenried, C., M.W. Lynch and J.W. Haslett,, "Modified CMOS Cherry-Hooper Amplifiers with Source-Follower Feedback in a 0.35  $\mu\text{m}$  Technology", *Proc. European Solid State Circuits Conference, Portugal* (September, 2003), 553-556.
- [47] C. Xu, X. Liu, L. Mollenauer, "Comparison of Return-To-Zero Phase Shift Keying and On-Off Keying In Long Haul Dispersion Managed Transmissions", *Proc. OFC 2003, Atlanta, GA*, (2003), ThE3.
- [48] K. Ishida, T. Kobayashi, J. Abe, K. Kinjo, S. Kuroda, T. Mizuochi, "A Comparative Study of 10 Gb/s RZ-DPSK and RZ-ASK WDM Transmission over Transoceanic Distances", *Proc. OFC 2003, Atlanta, GA*, (2003), ThE2.
- [49] G. Charlet, E. Corbel, J. Lazaro, A. Klekamp, R. Dischler, P. Tran, W. Idler, H. Mardoyan, A. Konczykowska, F. Jorge, S. Bigo, "WDM Transmission at 6 Tbit/s Capacity over Trans-Atlantic Distance, Using 42.7 Gb/s Differential Phase-Shift Keying without Pulse Carver", *Proc. OFC2004, Los Angeles, CA* (2004), PDP36.
- [50] C. M. Kim, R. V. Ramaswamy, "Overlap Integral Factors in Integrated Optic Modulators and Switches", *IEEE Journal of Lightwave Technology*, **vol. 7**, (1989), 1063-1070.
- [51] G. L. Li, P. K. L. Yu, "Optical Intensity Modulators for Digital and Analog Applications", *Journal of Lightwave Technology*, **vol. 21**, (September, 2003), 2010-2030.
- [52] E.L. Wooten, K.M. Kissa, A. Yi-Yan, E. J. Murphy, D. A. Lafaw, P.F. Hallemeier, D. Maack, D. V. Attanasio, D.J. Fritz, G.J. McBrien, D.E. Bossi, "A Review of Lithium Niobate Modulators for Fiber-Optic Communications Systems", *IEEE Journal Of Selected Topics In Quantum Electronics*, **vol. 6**, (January/February 2000), 69-82.
- [53] Keang-Po Ho, "Generation of Optical Signals", *Advanced Topics in Lightwave Communications*, (February, 2005), 1-19.
- [54] R. Noé, "Optical Amplifiers in System with Direct Detection", *Internal Study, University Paderborn, Germany* (2002).
- [55] Agere Systems Inc., "Agere 40 Gbit/s Lithium Niobate Electro-Optic Modulator", *Data Sheet Information* (2002).
- [56] P. A. Humblet, M. Azizoglu, "On The Bit Error Rate of Lightwave Systems with Optical Amplifiers", *Journal of Lightwave Technology*, **vol. 9**, (November, 1991), 1576-1582.
- [57] E. A. Swanson, J. C. Livas, R. S. Bondurant, "High Sensitivity Optically Preamplified Direct Detection DPSK Receiver with Active Delay-Line Stabilization", *IEEE Photonics Technology Letters*, **vol. 6**, (1994), 263-265.
- [58] D. Sandel, V. Mirvoda, F. Wüst, R. Noé, S. Hinz, "Signed Online Chromatic Dispersion Detection at 40 Gb/s with a Sub-ps/nm Dynamic Accuracy", *Proc. ECOC2002, Kopenhagen, Denmark*, **vol. 3**, (2002), 6.1.4.

- [59] B. Milivojevic, D. Sandel, S. Bhandare, R. Noé, F. Wüst, “40 Gbit/s CSRZ-DPSK Transmission System with Signed Online Chromatic Dispersion Detection”, *IEE Electronics Letters*, **vol. 39**, (2003), 1455–1456.
- [60] Editor: Govind P. Agrawal, “*Fiber-Optic Communication systems*”, volume vol. 26, of *Wiley Series In Microwave and Optical Engineering*, A Wiley Interscience Publication,, 1990.
- [61] Y. Takushima, H. Yoshimi, K. Kikuchi, H. Yamauchi, H. Taga, “Experimental Demonstration of In-service Dispersion Monitoring in 960-km WDM Transmission System Using Optical Frequency-Modulation Method”, *IEEE Photonics Technology Letters*, **vol. 15**, (2003), 870–872.
- [62] P. S. Cho, G. Harston, C. J. Kerr, A. S. Greenblatt, A. Kaplan, Y. Achiam, G. Levy-Yurista, M. Margalit, Y. Gross, and J. B. Khurgin,, “Investigation of 2-b/s/Hz 40-Gb/s DWDM Transmission over  $4 \times 100$  km SMF-28 Fiber Using RZ-DQPSK and Polarization Multiplexing”, *IEEE Photonics Technology Letters*, **vol. 16**, (February, 2004), 656-658.
- [63] M. Sharma et al, “Optical Circuits for Equalizing Group Delay Dispersion of Optical Fibers”, *IEEE Journal of Lightwave Technology*, **vol. 12**, (1994), 1759-1765.
- [64] K. Takiguchi et al., “Planar Lightwave Circuit Dispersion Equalizer”, *IEEE Journal of Lightwave Technology*, **vol. 14**, (1996), 2003-2011.
- [65] K. Takiguchi et al, “Dispersion Slope Equalizer For Dispersion Shifted Fiber Using a Lattice-Form Programmable Optical Filter on a Planar Lightwave Circuit”, *IEEE Journal of Lightwave Technology*, **vol. 16**, (1998), 1647-1656.
- [66] M. Bohn et al., “Tunable Dispersion Compensation in a 40 Gb/s System Using a Compact FIR Lattice Filter in SiON Technology”, *Proc. ECOC02 Copenhagen, Denmark* (2002), II, 4.2.3.
- [67] G.L. Bona et al., “Tunable Dispersion Compensators Realized in High-Refractive-Index-Contrast SiOn Technology”, *Proc. ECOC’02 Copenhagen, Denmark* (2002), II, 4.2.1.
- [68] Andreas Othonos, Kyriacos Kalli, “*Fiber Bragg Gratings*,” Fundamentals and Applications in Telecommunications and Sensing, III, Artech House, Boston-London, 1999.
- [69] M. Guy, F. Trpanier, A. Doyle, Y. Painchaud, R. Lachance, “Novel Applications of Fiber Bragg Grating Components for Next-Generation WDM Systems”, *Annales des tcommunications*, **vol. 58**, (2003), 1275–1306.
- [70] Z. Pan, Y.W. Song, C. Yu, Y. Wang, Q. Yu, J. Popelek, H. Li, Y. Li, A. E. Willner, “Tunable Chromatic Dispersion Compensation in 40 Gbit/s Systems Using Nonlinearly Chirped Fiber Bragg Grating”, *IEEE Journal Lightwave Technology*, **vol. 20**, (December, 2002), 2239–2246.
- [71] P. Pecci et al, “Tolerance to Dispersion Compensation Parameters of Six Modulation Formats in Systems Operating at 43 Gbit/s”, *Proc. ECOC03, Rimini, Italy* (2003), We3.5.5.

- [72] Y. Yokoyama et al, "Precise Dispersion Monitoring and Dynamic Compensation in 42.7 Gbit/s Long-Haul Transmission Using an Optical Time Domain Level Monitoring Technique", *Proc. ECOC2003, Rimini, Italy* (2003), PDP, Th4.2.1.
- [73] S. Bhandare, D. Sandel, B. Milivojevic, A. Hidayat, A. Fauzi, H. Zhang, S. K. Ibrahim, F. Wüst, R. Noé, "5.94 Tbit/s, 1.49 bit/s/Hz ( $40 \times 2 \times 2 \times 40$  Gbit/s) RZ-DQPSK Polarization Division Multiplex C-Band Transmission over 324 km", *IEEE Photonics Technology Letters*, **vol. 17**, (April, 2005), 914–916.
- [74] A. F. Abas, B. Milivojevic, A. Hidayat, S. Bhandare, D. Sandel, H. Zhang, R. Noé, "2.38 Tbit/s, 1.49 bit/s/Hz, 40 Gbit/s RZ-DQPSK Polarization Division Multiplex Transmission over 273 km of Fiber", *Electrical Engineering* (2005), accepted.
- [75] B. Milivojevic, A. Fauzi Abas, A. Hidayat, S. Bhandare, D. Sandel, R. Noé, M. Guy, M. Lapointe, "1.6-bit/s/Hz, 160-Gbit/s, 230-km RZ-DQPSK Polarization Multiplex Transmission with Tunable Dispersion Compensation", *IEEE Photonics Technology Letters*, **vol. 17**, (February, 2005), 495–497.
- [76] N. Yoshikane, I. Morita, "160% Spectrally-Efficient 5.12 Tb/s ( $64 \times 85.4$  Gb/s RZ DQPSK) Transmission without Polarisation Demultiplexing", *ECOC Proceedings Post Deadline*, **Th4.4.3** (2004), 44–45.
- [77] R. Noé, "Coherent Optical Transmission", *Internal Study, University Paderborn, Germany* (2002).
- [78] Keang-Po Ho, "Generation of Arbitrary Quadrature Signals Using One Dual-Drive Modulator", *Journal of Lightwave Technology*, **vol. 23**, (2005), 764–770.
- [79] Sheldon Walklin, Jan Conradi, "A 10 Gb/s 4-ary ASK Lightwave System", *Proc. IOOC-ECOC97, Edinburg, Scotland* (September, 1997).
- [80] B. Wedding et al, "Multi-Level Dispersion Supported Transmission at 20 Gbit/s over 46 km Installed Standard Singlemode Fiber", *Proc. ECOC96*, **MoB.4.4** (September, 1996), 91–94.
- [81] Sheldon Walklin, Jan Conradi, "Multilevel Signaling for Increasing the Reach of 10 Gb/s Lightwave Systems", *Journal of Lightwave Technology*, **vol. 17**, (November, 1999), 2235–2248.
- [82] J.P. Gordon, and L.F. Mollenauer, "Phase Noise in Photonic Communication Systems Using Linear Amplifiers", *Opt. Letters*, **vol. 15**, (1990), 1351–1353.
- [83] S. Ryu, "Signal Linewidth Broadening due to Nonlinear Kerr Effect in Long-Haul Coherent Systems Using Cascaded Optical Amplifiers", *IEEE Journal of Lightwave Technology*, **vol. 10**, (1992), 1450–1457.
- [84] R. Schmidt, T.F. Meister, M. Rest, H.M. Rein, "23 Gbit/s SiGe Modulator Driver with 3.5 V Single-Ended Output Swing", *Design Aspects and Measuring Results, Int., IEEE MTT/AP, Workshop on MMIC Design, Packaging and System Applications, Freiburg, Germany* (1998), 87–88.

- [85] Douglas S. McPherson, Florin Pera, Mihai Tazlauanu, Sorin P. Voinigescu, "A 3-V Fully Differential Distributed Limiting Driver for 40-Gb/s Optical Transmission Systems", *IEEE Journal of Solid-State Circuits*, **vol. 38**, (September, 2003).
- [86] J.H. Sinsky, A. Adamiecki, A. Gnauck, C. Burrus, J. Leuthold, "A 42.7 Gb/s Balanced Optical Front End with Record Sensitivity", *Proc. OFC2003* (2003), PD39.
- [87] J. Kim et al., "A 12 dBm 320-GHz GBW distributed amplifier in a SOI 0.12 $\mu$ m CMOS technology", *Proc. IEEE ISSCC Dig. Tech. Papers*, (2004), 478–479.
- [88] J. Olivier Plouchart, J. Kim, N. Zamdmer, L.H. Lu, M. Sherony, Y. Tan, R. A. Groves, R. Trzcinski, M. Talbi, A. Ray, L. F. Wagner, "A 4-91 GHz Traveling-Wave Amplifier in a Standard 0.12 $\mu$ m SOI CMOS Microprocessor Technology", *IEEE Journal Of Solid-State Circuits*, **39** (September, 2004), no.9, 1455-1461.
- [89] A. Hee-Tae, D. J. Allstot, "A 0.5-8.5 GHz fully differential CMOS distributed amplifier", *IEEE Journal of Solid-State Circuits*, **37** (August, 2002), 985-993.
- [90] Philips, "*GaAs IC Design Manuals*", D01PH Design Manual, July, 2002, OMMIC.
- [91] I. D. Robertson, S. Lucyszyn, "*RFIC and MMIC Design and Technology*", IEE Circuits, Devices and Systems Series, vol. 13, The Institution of Electrical Engineers, London, United Kingdom, (2001).
- [92] P. J. Sullivan, B. A. Xavier, D. Costa, and W. H. Ku, "Silicon MOSFET Distributed Amplifier", *Electronics Letters*, **vol. 32** (June, 1996), no. 12, 1106.
- [93] Patrick J. Sullivan, Bernard A. Xavier and Walter H. Ku, "An Integrated CMOS Distributed Amplifier Utilizing Packaging Inductance", *IEEE Transactions on Microwave Theory and Techniques*, **vol. 45**, (October, 1997), no.10, 1969–1976.
- [94] B. Kleveland, C.H. Diaz, D. Vook, L. Madden, T.H. Lee, S.S. Wong, "Monolithic CMOS Distributed Amplifier and Oscillator", *IEEE Int. Solid-State Circuits Conf. Dig.*, **MP 4.3** (1999), 70–71.
- [95] B. Ballweber, R. Gupta, D. Allstot, "A Fully Integrated 0.55.5 GHz CMOS Distributed Amplifier", *IEEE Solid-State Circuits*, **vol. 35**, (February, 2000), 231–239.
- [96] B. M. Frank, A. P. Freundorfer, Y. M. M. Antar, "Performance of 110-GHz Travelling Wave Amplifiers in 0.18- $\mu$ m CMOS", *IEEE Microwave And Wireless Components Letters*, **vol. 12**, (September, 2002).
- [97] S. P. Voinigescu, S. W. Tarasewicz, T. MacElwee, J. Ilowski, "An Assessment of State-Of-The-Art 0.5  $\mu$ m Bulk CMOS Technology for RF Applications", *Proc. IEDM* (1995), 721-724.
- [98] A. Thiede, "*High Frequency Electronics*", Lecture Notes, University Paderborn.
- [99] David M. Pozar, "*Microwave Engineering*", John Wiley and Sons, Inc., 2. edition, 1998.

- [100] H. S. P. Wong, D. J. Frank, P. M. Solomon, C. H. J. Wann, and J. J. Welser, "Nanoscale CMOS", *Proc. IEEE*, **vol. 87**, (April, 1999), no.10, 537–570.
- [101] Behzad Razavi, "The Role of Monolithic Transmission Lines in High-Speed Integrated Circuit", *Proc. IEEE Custom Integrated Circuit Conference* (2002), 367–374.
- [102] William R. Eisenstadt, Yungseon Eo, "S-Parameter-Based IC Interconnect Transmission Line Characterization", *IEEE Transaction on Components, Hybrids and Manufacturing Technology*, **vol. 15**, (1992), 483–489.
- [103] A. Thiede, "*Analog CMOS Integrated Circuits*", Lecture Notes, University Paderborn.



## **Acknowledgements**

I would like to sincerely thank my Professors Dr.-Ing. Reinhold Noè and Dr.-Ing. Andreas Thiede for offering me an opportunity to work in their internationally recognized groups in the area of optical communication and high-frequency electronics. I am grateful for their generous support and motivating discussions during my dissertation. I sincerely thank both of them for their kindness, patience and encouragement.

Further, I would like to thank Professor Dr. math Friedhelm Meyer auf der Heide for acting as supervisor during my work.

I would like to thank Dr.-Ing. David Sandel and Dr.-Ing. Suhas Bhandare from whom I received enormous help during the entire course and especially in the last phase of my work.

Here, I would like to thank Mr. Bernd Bartsch and Mr. Gerhard Wieseler for their constant encouragement and technical support.

I gratefully acknowledge the help that I received from all my colleges and friends from the Optoelectronic and High Frequency Electronic Group at Electrical Engineering department of the University of Paderborn - Selvan K. Ibrahim, Ariya Hidayat, Sebastian Hoffmann, Abas Ahmad Fauzi, Dr. Olaf Adamczyk, Vitali Mirvoda, Zheng Gu and Dr.-Ing. Frank Wüst.

I would also like to thank my husband and my son Nikola for continuous support, in spite of the long periods of my physical and mental absence they had to put with. I also would like to thank my parents for giving constant moral support throughout the entire stay in Germany.

Paderbron, Germany  
April 7, 2005

Biljana Milivojevic